

WL-TR-93-1172

WIDEBAND ELECTROMAGNETIC SCATTERING/
ANALYSIS PROGRAM

ELECTROMAGNETIC SCATTERING FROM THE TRUNKS
AND BRANCHES OF TREES

AD-A283 112



A. A. NOWOTARSKI
R. J. MARHEFKA

THE OHIO STATE UNIVERSITY
ELECTROSCIENCE LABORATORY
1320 KINNEAR ROAD
COLUMBUS OH 43212

SEPTEMBER 1993

INTERIM REPORT FOR 10/01/92-09/30/93

APPROVED FOR PUBLIC RELEASE; DISTRIBUTION IS UNLIMITED.

1278 94-24971

DTIC
ELECTE
AUG 10 1994
S B D

94 8 08 035

AVIONICS DIRECTORATE
WRIGHT LABORATORY
AIR FORCE MATERIEL COMMAND
WRIGHT PATTERSON AFB OH 45433-7409

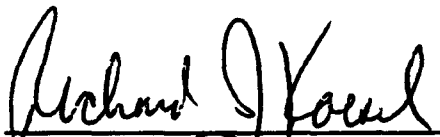
DTIC QUALITY INSPECTED 1



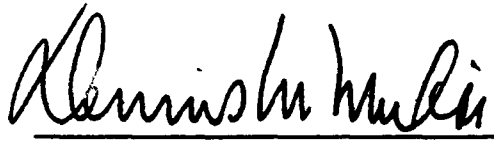
NOTICE

WHEN GOVERNMENT DRAWINGS, SPECIFICATIONS, OR OTHER DATA ARE USED FOR ANY PURPOSE OTHER THAN IN CONNECTION WITH A DEFINITELY GOVERNMENT-RELATED PROCUREMENT, THE UNITED STATES GOVERNMENT INCURS NO RESPONSIBILITY OR ANY OBLIGATION WHATSOEVER. THE FACT THAT THE GOVERNMENT MAY HAVE FORMULATED OR IN ANY WAY SUPPLIED THE SAID DRAWINGS, SPECIFICATIONS, OR OTHER DATA, IS NOT TO BE REGARDED BY IMPLICATION, OR OTHERWISE IN ANY MANNER CONSTRUED, AS LICENSING THE HOLDER, OR ANY OTHER PERSON OR CORPORATION; OR AS CONVEYING ANY RIGHTS OR PERMISSION TO MANUFACTURE, USE, OR SELL ANY PATENTED INVENTION THAT MAY IN ANY WAY BE RELATED THERETO.

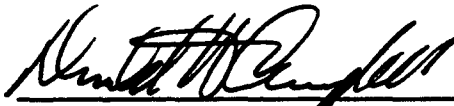
This report is releasable to the National Technical Information Service (NTIS). At NTIS, it will be available to the general public, including foreign nations.



RICHARD J. KOESSEL
PROJECT ENGINEER



DENNIS M. MUKAI, SEC CHIEF
TECHNOLOGY DEVELOPMENT SECTION



DONALD H. CAMPBELL
ACTG DIRECTOR
MISSION AVIONICS DIVISION
AVIONICS DIRECTORATE

IF YOUR ADDRESS HAS CHANGED, IF YOU WISH TO BE REMOVED FROM OUR MAILING LIST, OR IF THE ADDRESSEE IS NO LONGER EMPLOYED BY YOUR ORGANIZATION, PLEASE NOTIFY WL/AARM-1, WRIGHT-PATTERSON AFB OH 45433-7408 TO HELP MAINTAIN A CURRENT MAILING LIST.

COPIES OF THIS REPORT SHOULD NOT BE RETURNED UNLESS RETURN IS REQUIRED BY SECURITY CONSIDERATIONS, CONTRACTUAL OBLIGATIONS, OR NOTICE ON A SPECIFIC DOCUMENT.

REPORT DOCUMENTATION PAGE			Form Approved OMB No. 0704-0188	
Public reporting burden for this collection of information is estimated to average 1 hour per response, including the time for reviewing instructions, searching existing data sources, gathering and maintaining the data needed, and completing and reviewing the collection of information. Send comments regarding this burden estimate or any other aspect of this collection of information, including suggestions for reducing this burden, to: Washington Headquarters Services, Directorate for Information Operations and Reports, 1215 Jefferson Davis Highway, Suite 1204, Arlington, VA 22202-4302, and to the Office of Management and Budget, Paperwork Reduction Project (0704-0188), Washington, DC 20503.				
1. AGENCY USE ONLY (Leave blank)	2. REPORT DATE SEP 1993	3. REPORT TYPE AND DATES COVERED INTERIM 10/01/92--09/30/93		
4. TITLE AND SUBTITLE WIDEBAND ELECTROMAGNETIC SCATTERING/ ANALYSIS PROGRAM ELECTROMAGNETIC SCATTERING FROM THE TRUNKS AND BRANCHES OF TREES		5. FUNDING NUMBERS C F33615-91-C-1729 PE 62204 PR 7622 TA 07 WU 71		
6. AUTHOR(S) A. A. NOWOTARSKI R. J. MARHEFKA				
7. PERFORMING ORGANIZATION NAME(S) AND ADDRESS(ES) THE OHIO STATE UNIVERSITY ELECTROSCIENCE LABORATORY 1320 KINNEAR ROAD COLUMBUS OH 43212		8. PERFORMING ORGANIZATION REPORT NUMBER 724733-3		
9. SPONSORING / MONITORING AGENCY NAME(S) AND ADDRESS(ES) AVIONICS DIRECTORATE WRIGHT LABORATORY AIR FORCE MATERIEL COMMAND WRIGHT PATTERSON AFB OH 45433-7409		10. SPONSORING / MONITORING AGENCY REPORT NUMBER WL-TR-93-1172		
11. SUPPLEMENTARY NOTES				
12a. DISTRIBUTION / AVAILABILITY STATEMENT APPROVED FOR PUBLIC RELEASE; DISTRIBUTION IS UNLIMITED.			12b. DISTRIBUTION CODE	
13. ABSTRACT (Maximum 200 words) The electromagnetic scattering from various parts of a tree is analyzed to find their characteristics for frequencies between 0.3-1.3 GHz. The scattered fields in the vicinity of a tree are found to be relatively insensitive to the dielectric materials used in tree modeling. The RCS of a trunk and its ground interactions are examined and it is found to be 5-7 dB higher for the horizontal than for the vertical polarization for the angles of interest. The difference is due to the reflection coefficients near the Brewster angle. The scattering from branches is shown to have similar polarization difference and is about 20 dB lower than the trunk-ground scattering. The analysis is based on deterministic techniques using the Uniform Geometrical Theory of Diffraction and are compared to eigenfunction solutions and measurements.				
14. SUBJECT TERMS DIELECTRIC POLARIZATION UTD MODELING SCATTERING			15. NUMBER OF PAGES 125	
			16. PRICE CODE	
17. SECURITY CLASSIFICATION OF REPORT UNCLASSIFIED	18. SECURITY CLASSIFICATION OF THIS PAGE UNCLASSIFIED	19. SECURITY CLASSIFICATION OF ABSTRACT UNCLASSIFIED	20. LIMITATION OF ABSTRACT UL	

Contents

Accession For	
NTIS GRA&I	<input checked="" type="checkbox"/>
DTIC TAB	<input type="checkbox"/>
Unannounced	<input type="checkbox"/>
Justification	
By	
Distribution/	
Availability Codes	
Dist	Avail and/or Spec
A-1	

List of Figures	v
List of Tables	x
Glossary	xi
1 Introduction	1
2 Geometrical Theory of Diffraction	3
1 Introduction	3
2 Theory	3
3 Chiang and Marhefka Rim Caustic Correction	6
3 Background	8
1 Introduction	8
2 Modeling of a Tree	8
3 Dielectric Properties of Trees	10
4 Dielectric Properties of Soil	12
4 Scattering From Logs	13
1 Introduction	13
2 Theory of Modeling a Log	14
2.1 Dielectric Properties of Wood	14
2.2 Effect of Wood Roughness	15
2.3 Solution of Dielectric Cylinder Scattering	16
3 Measurement of the Radar Cross Section of Logs	16
4 Comparison of Log RCS with Theory	21
5 Summary	32
5 Scattered Fields in the Vicinity of a Tree Trunk	34
1 Introduction	34
2 Target Geometries	35
3 Analysis and Results	38

3.1	Results for Cylinders of Infinite Length	38
4	Results For Cylinders Of Finite Length	46
5	Summary	55
6	Trunk-Ground Interactions	62
1	Introduction	62
2	Modeling of Geometry	63
3	Verification of TGI Solution	68
4	Analysis of Trunk-Ground Interactions	69
5	Summary	77
7	Branch Scattering	81
1	Introduction	81
2	Modeling of Branch Scattering	82
3	Analysis of Branch Scattering	85
4	Summary	90
8	Summary and Conclusions	95
APPENDICES		
A	Reflection and Transmission of plane waves in Planar, Stratified (multilayered) Medium	98
B	Scattering of Plane Waves by Stratified (multilayered) Cylinders	103
C	Scattering from Multijointed Cylinders	108
	Bibliography	113

Figures

1	Canonical geometry for the diffraction by a wedge.	5
2	Measured RCS of log #1 for TM and TE polarizations.	18
3	Measured RCS of log #2 for TM and TE polarizations.	19
4	Measured RCS of log #3 for TM and TE polarizations.	20
5	Comparison of the RCS of the dielectric cylinder used to model a log for relative dielectric constants of $\epsilon_r=24-j8$ and $\text{Real}[\epsilon_r]=24$, $\sigma_e=0.5563$	23
6	Comparison of the RCS of the dielectric cylinder used to model a log for relative dielectric constants of $\epsilon_r=24-j8$ and $\text{Real}[\epsilon_r]=24$, $\sigma_e=0.5563$ processed to remove the creeping wave component.	24
7	Echo width for TE polarization of logs #1, #2, and #3 from process- ing RCS measurements to show variation in echo width for logs from the same tree.	25
8	Echo width for TM polarization of logs #1, #2, and #3 from pro- cessing RCS measurements to show variation in echo width for logs from the same tree.	26
9	Echo width for TE polarization of logs #1, #2, and #3 from process- ing RCS measurements compared to different dielectric models for the logs.	28
10	Echo width for TM polarisation of logs #1, #2, and #3 from pro- cessing RCS measurements compared to different dielectric models for the logs.	29
11	Variation of roughness factor δ_r for different values of Δh as a function of frequency.	30
12	Comparison between the measured and calculated RCS of log #2. For the modeling, the parameters are $\epsilon_r=24-j8$ and $\Delta h=0.0025\text{m}$	31
13	Geometry for infinite length cylinder analysis with normal plane wave incidence.	36
14	Geometry used for analysis of finite length cylinders with oblique plane wave incidence.	37

15	Geometry used for analysis of finite length cylinders with oblique plane wave incidence above an infinite ground plane to simulate the ground.	37
16	Total E-field magnitude in dB relative to the incident field for a three-layer cylinder at a distance of 4 meters at 0.75GHz.	40
17	Total E-field magnitude in dB relative to the incident field for a three-layer cylinder at a distance of 10 meters at 0.75GHz.	41
18	Total E-field magnitude in dB relative to the incident field for a three-layer cylinder at a distance of 30 meters at 0.75GHz.	42
19	Total E-field magnitude in dB relative to the incident field for a two-layer cylinder at a distance of 4 meters at 0.75GHz.	43
20	Total E-field magnitude in dB relative to the incident field for a single layer cylinder with $\epsilon_r=12.4-j4.9$ at a distance of 4 meters at 0.75GHz.	44
21	Total E-field magnitude in dB relative to the incident field for a single layer cylinder with $\epsilon_r=24-j8$ at a distance of 4 meters at 0.75GHz.	45
22	Total E-field magnitude in dB relative to the incident field for a three-layer cylinder at 0.75GHz for TM polarization.	47
23	Total E-field magnitude in dB relative to the incident field for a three-layer cylinder at 0.75GHz for TE polarization.	48
24	Total E-field magnitude in dB relative to the incident field for a three-layer cylinder at 0.75GHz for TM polarization.	49
25	Total E-field magnitude in dB relative to the incident field for a three-layer cylinder at 0.75GHz for TE polarization.	50
26	Total E-field magnitude in dB relative to the incident field for a single layer cylinder with $\epsilon_r=12.4-j4.9$ at 0.75GHz for TM polarization.	51
27	Total E-field magnitude in dB relative to the incident field for a single layer cylinder with $\epsilon_r=12.4-j4.9$ at 0.75GHz for TE polarization.	52
28	Total E-field magnitude in dB relative to the incident field for a single layer cylinder with $\epsilon_r=24-j8$ at 0.75GHz for TM polarization.	53
29	Total E-field magnitude in dB relative to the incident field for a single layer cylinder with $\epsilon_r=24-j8$ at 0.75GHz for TE polarization.	54
30	Comparison of total E-field magnitude in dB relative to the incident field for a P.E.C. cylinder for an exact solution at normal incidence and a UTD solution at 15 degrees incidence at a distance of 5 meters at 0.75GHz	56
31	Comparison of total E-field magnitude in dB relative to the incident field for a P.E.C. cylinder for an exact solution at normal incidence and a UTD solution at 30 degrees incidence at a distance of 5 meters at 0.75GHz.	57

32	Comparison of total E-field magnitude in dB relative to the incident field for a P.E.C. cylinder for an exact solution at normal incidence and a UTD solution at 15 degrees incidence at a distance of 10 meters at 0.75GHz.	58
33	Comparison of total E-field magnitude in dB relative to the incident field for a P.E.C. cylinder for an exact solution at normal incidence and an imaged UTD solution at 15 degrees incidence at a distance of 5 meters at 0.75GHz.	59
34	Comparison of total E-field magnitude in dB relative to the incident field for a P.E.C. cylinder for an exact solution at normal incidence and an imaged UTD solution at 30 degrees incidence at a distance of 5 meters at 0.75GHz.	60
35	Geometry used to model trunk-ground interactions.	63
36	Diffraction interactions used in trunk-ground interaction modeling . .	64
37	Calculation of RD and DR term using small bistatic angles between ray paths.	67
38	Comparison of top-hat and TGI solutions for the PEC case. The cylinder radius $a=0.2\text{m}$ and height $H=15\text{m}$. The top-hat base is 430 meters for this comparison and the frequency is 0.75GHz.	70
39	Radar cross section for a tree with $DBH=14''$ and height $h_t=17\text{m}$ at a frequency of 0.75GHz for both horizontal and vertical polarizations. The relative dielectric constant of the ground is $\epsilon_g=20-j0.15$. The relative dielectric constant of the tree is $\epsilon_t=12.4-j4.9$ for the top plot and $\epsilon_t=24-j8$ for the bottom plot.	72
40	Radar cross section for a tree with $DBH=14''$ and height $h_t=17\text{m}$ at a frequency of 0.75GHz for both horizontal and vertical polarizations. The relative dielectric constant of the ground is $\epsilon_g=7-j1.5$. The relative dielectric constant of the tree is $\epsilon_t=12.4-j4.9$ for the top plot and $\epsilon_t=24-j8$ for the bottom plot.	73
41	Radar cross section for a tree with $DBH=14''$ and height $h_t=17\text{m}$ at a frequency of 0.75GHz for both horizontal and vertical polarizations. The relative dielectric constant of the ground is $\epsilon_g=18-j5$. The relative dielectric constant of the tree is $\epsilon_t=12.4-j4.9$ for the top plot and $\epsilon_t=24-j8$ for the bottom plot.	74
42	Reflection coefficient from dielectric half-spaces to show the differences in the reflection coefficient (Γ) for the horizontal and vertical polarizations of the dielectric materials used in modeling the trunk-ground interaction. Top plot is of the reflection coefficients for soil dielectric constants (Γ_s) and the bottom plot is of the reflection coefficients for tree dielectric constants (Γ_t).	76

43	Radar cross section for a tree with $DBH = 12''$ and height $h_t = 14.8m$ at a frequency of 0.75GHz for both horizontal and vertical polarizations. The relative dielectric constant of the ground is $\epsilon_g = 18-j5$. The relative dielectric constant of the tree is $\epsilon_t = 12.4-j4.9$ for the top plot and $\epsilon_t = 24-j8$ for the bottom plot.	78
44	Radar cross section for a tree with $DBH = 12''$ and height $h_t = 14.8m$ at a frequency of 1.3GHz for both horizontal and vertical polarizations. The relative dielectric constant of the ground is $\epsilon_g = 18-j5$. The relative dielectric constant of the tree is $\epsilon_t = 12.4-j4.9$ for the top plot and $\epsilon_t = 24-j8$ for the bottom plot.	79
45	Radar cross section for a tree with $DBH = 16''$ and height $h_t = 20m$ at a frequency of 1.3GHz for both horizontal and vertical polarizations. The relative dielectric constant of the ground is $\epsilon_g = 7-j1.5$. The relative dielectric constant of the tree is $\epsilon_t = 12.4-j4.9$ for the top plot and $\epsilon_t = 24-j8$ for the bottom plot.	80
46	Geometry used to model branch scattering.	83
47	Radar cross section of 90 degree PEC cylindrical dihedral with diameters of 12'' for comparison to the dielectric case of scattering from a tree-branch dihedral at a frequency of 0.75GHz.	87
48	Radar cross section of 90 degree cylindrical dihedral to simulate the scattering from a tree-branch dihedral at a frequency of 0.75GHz. The tree diameter (DBH) is 12'' with a relative dielectric constant of $\epsilon_b = \epsilon_t = 12.4-j4.9$	88
49	Radar cross section of 90 degree cylindrical dihedral to simulate the scattering from a tree-branch dihedral at a frequency of 0.75GHz. The tree diameter (DBH) is 12'' and a relative dielectric constant of $\epsilon_b = \epsilon_t = 24-j8$	89
50	Radar cross section of 90 degree cylindrical dihedral to simulate the scattering from a tree-branch dihedral at a frequency of 0.75GHz. The tree diameter (DBH) is 14'' with relative dielectric constants of $\epsilon_b = \epsilon_t = 12.4-j4.9$ and $\epsilon_b = \epsilon_t = 24-j8$	91
51	Radar cross section of 90 degree cylindrical dihedral to simulate the scattering from a tree-branch dihedral at a frequency of 0.75GHz. The tree diameter (DBH) is 16'' with relative dielectric constants of $\epsilon_b = \epsilon_t = 12.4-j4.9$ and $\epsilon_b = \epsilon_t = 24-j8$	92
52	Radar cross section of 90 degree cylindrical dihedral to simulate the scattering from a tree-branch dihedral at a frequency of 1.3GHz. The tree diameter (DBH) is 16'' with relative dielectric constants of $\epsilon_b = \epsilon_t = 12.4-j4.9$ and $\epsilon_b = \epsilon_t = 24-j8$	93
53	A plane multilayer, illustrating the outgoing and the reflected waves in each layer.	99

54	A Multilayered Dielectric Cylinder of Infinite Length.	104
55	Geometry of multijointed cylinder.	109
56	Diffraction interactions Used in calculating the scattering from multijointed cylinders.	110

Tables

1	Dielectric constants used to model the dielectric properties of wood at L-Band from the literature.	11
2	Dielectric constants used to model the dielectric properties of wood at L-Band from the literature for multilayered modeling.	11
3	Dielectric constants used to model the dielectric properties of soil at L-Band from the literature.	12
4	Diameters of trees (<i>DBH</i>) and the corresponding tree height <i>h</i> and effective tree height <i>h_t</i> of the cylinder used to model the tree.	69
5	Diameters of trees (<i>DBH</i>) and the corresponding cylinder lengths used in modeling branch scattering for worst case analysis.	86

Glossary

2D	— Two-Dimensional
3D	— Three-Dimensional
DBH	— Diameter of tree at Breast Height
dBm	— deciBels with respect to a meter
dBsm	— deciBels with respect to a square meter
DR	— Diffracted-Reflected field
DRD	— Diffracted-REflected-Diffracted fields
GTD	— Geometrical Theory of Diffraction
NEC-BSC	— Numerical Electromagnetic Code - Basic Scattering Code
PEC	— Perfect Electrical Conducting
RCS	— Radar Cross Section
RD	— Reflected-Diffracted field
RDR	— Reflected-Diffracted-Reflected field
TE	— Transverse Electric (electric field perpendicular to z -axis)
TGI	— Trunk-Ground Interaction
TM	— Transverse Magnetic (magnetic field perpendicular to z -axis)
UTD	— Uniform Geometrical Theory of Diffraction

SECTION 1

Introduction

In recent years, there has been an increased interest in the electromagnetic scattering from forests. Current measurements of the scattering from trees cover almost the entire electromagnetic spectrum from low frequency radio waves to light [1, 2]. One frequency band of interest is in the low microwave range near L-Band specifically between 0.3-1.3GHz. This frequency range is of interest, because the electromagnetic wave is of long enough wavelength to penetrate through the outer leaf canopy of the forest yet is small enough to provide information about what is below the leaves. These characteristics make these wavelengths useful in remote sensing applications. Previously, most of the measurements and modeling of the scattering from forests at L-Band has concentrated on narrow band radar systems. These systems have low resolution and are unable to isolate the scattering from individual trees. Therefore when modeling is needed, the scattering behaviour from an individual tree is not important.

For ultrawide bandwidth radar systems, the scattering from a single tree is important since the individual trees are identifiable. Therefore, the electromagnetic scattering from an individual tree needs to be examined. To study the scattering from a tree, a modified form of the Geometrical Theory of Diffraction (GTD) for dielectric materials is used for the analysis. For background, an introduction to GTD is presented in Chapter 2 to provide the basic information used in analyzing

the scattering from a tree. Chapter 3 provides background into current methods and parameters used in modeling trees, wood, and soil.

Before the geometry of a tree is analyzed, a simpler geometry is examined. To do this, measurements of the radar cross section (RCS) of tree logs are presented in Chapter 4. The measurements of the logs help to confirm the methods and parameters used in modeling wood that are presented in Chapter 3 since the cylindrical geometry of the logs is simpler to analyze than the complete geometry of a tree.

After the wood modeling is confirmed through log measurements, the scattering from various parts of a tree are examined. Chapter 5 examines the scattered fields in the vicinity of a tree trunk. For this analysis, the trunk is modeled based on the results of Chapters 3 and 4. In Chapter 6 a model for the scattering from a tree that includes interactions between the ground and the trunk are examined. In Chapter 7 the scattering from tree branches is examined. By separating the scattering from the trunk and ground from the branch scattering, the contributions and importance of each scattering mechanism is determined.

SECTION 2

Geometrical Theory of Diffraction

1 Introduction

This chapter provides a brief description of the modified Geometrical Theory of Diffraction (GTD). The far-zone diffracted field and diffraction coefficients for perfectly conducting and dielectric wedges are presented. Also, corrections to GTD for curved disks are shown. The term GTD is used for convenience but is meant to incorporate the Uniform Geometrical Theory of Diffraction (UTD) and the modified form of GTD for dielectric media throughout. Details on GTD can be found in References[3, 4, 5]. The time dependence $e^{j\omega t}$ is used and is suppressed throughout.

2 Theory

The Geometrical Theory of Diffraction (GTD) was developed in great detail by Keller and can be found in [6]. The general solution to a problem has the form:

$$\vec{E}^t(P) = \vec{E}^i(P) + \vec{E}^r(P) + \vec{E}^d(P) \quad (1)$$

where $\vec{E}^i(P)$ is the incident field at the observation point P and $\vec{E}^r(P)$ is the reflected field at P . The far zone diffracted field $\vec{E}^d(P)$ at point P is of the form:

$$\vec{E}^d(P) = \vec{E}^i(Q_s) \cdot \overline{D} \sqrt{\rho^d} \frac{e^{-jks}}{s}. \quad (2)$$

where \bar{D} is a dyadic diffraction coefficient given by:

$$\bar{D} = -\hat{\beta}'_0 \hat{\beta}_0 D_s - \hat{\Phi}'_0 \hat{\Phi}_0 D_h \quad (3)$$

and $\vec{E}^i(Q_e)$ is the incident field at the point of diffraction Q_e . The amplitude spreading factor is defined as the square root term in (2). For the perfectly conducting case, the diffraction coefficients D_s and D_h corresponding to the soft and hard polarizations; respectively, are:

$$D_{s,h} = \frac{-e^{-j\pi/4}}{2n\sqrt{2\pi k} \sin \beta_0} \left\{ \left[\cot \left(\frac{\pi + (\Phi - \Phi')}{2n} \right) + \cot \left(\frac{\pi - (\Phi - \Phi')}{2n} \right) \right] \mp \left[\cot \left(\frac{\pi + (\Phi + \Phi')}{2n} \right) + \cot \left(\frac{\pi - (\Phi + \Phi')}{2n} \right) \right] \right\}. \quad (4)$$

The caustic of the diffracted ray is ρ^d and is given by:

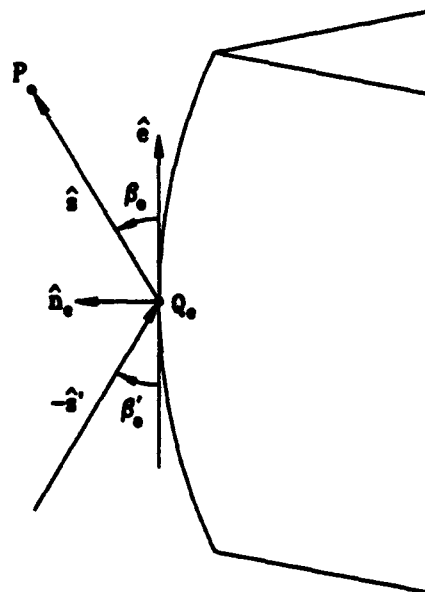
$$\frac{1}{\rho^d} = \frac{1}{\rho_e} + \frac{\hat{n}_e \cdot (\hat{s}' + \hat{s})}{\rho_g \sin^2 \beta_0} \quad (5)$$

where ρ_e is the radius of curvature of the incident wave in the edge fixed plane and ρ_g is the radius of curvature of the edge at the point of diffraction. The geometry for these diffracted rays is shown in Figure 1.

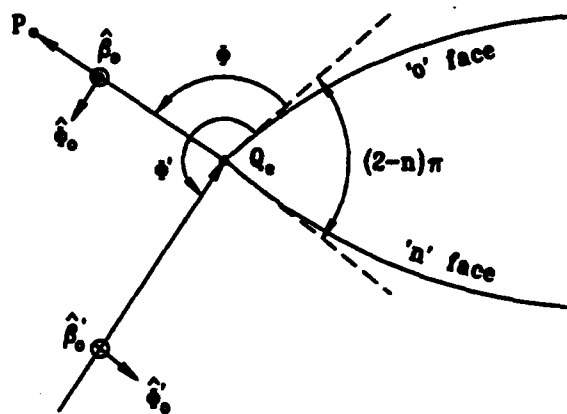
The above diffraction coefficient in Equation (4) must be modified for the dielectric cases that are encountered in analyzing trees. It is shown in References [7, 8, 9] that the modified diffraction coefficient for an electrically thin dielectric is:

$$D_{s,h} = \frac{-e^{-j\pi/4}}{2n\sqrt{2\pi k} \sin \beta_0} \times \left\{ \left[(1 - T_o^{s,h}) \cot \left(\frac{\pi + (\Phi - \Phi')}{2n} \right) + (1 - T_n^{s,h}) \cot \left(\frac{\pi - (\Phi - \Phi')}{2n} \right) \right] + \left[R_o^{s,h} \cot \left(\frac{\pi + (\Phi + \Phi')}{2n} \right) + R_n^{s,h} \cot \left(\frac{\pi - (\Phi + \Phi')}{2n} \right) \right] \right\}. \quad (6)$$

where $R_o^{s,h}$ and $R_n^{s,h}$ are the reflection coefficients for the soft and hard polarizations for the 'o' and the 'n' faces, respectively, and $T_o^{s,h}$ and $T_n^{s,h}$ are the transmission coefficients for the soft and hard polarizations for the 'o' and 'n' faces, respectively. Calculation of the reflection and transmission coefficients are given in Appendix A or



(a)



(b)

Figure 1: Canonical geometry for the diffraction by a wedge.

in Reference [10]. The above equation can be reduced further if the assumption that the dielectric material is lossy so that the transmission coefficient becomes small. With this assumption, the diffraction coefficient reduces to:

$$D_{s,h} = \frac{-e^{-j\pi/4}}{2n\sqrt{2\pi k} \sin \beta_0} \left\{ \left[\cot \left(\frac{\pi + (\Phi - \Phi')}{2n} \right) + \cot \left(\frac{\pi - (\Phi - \Phi')}{2n} \right) \right] + \left[R_o^{s,h} \cot \left(\frac{\pi + (\Phi + \Phi')}{2n} \right) + R_n^{s,h} \cot \left(\frac{\pi - (\Phi + \Phi')}{2n} \right) \right] \right\}. \quad (7)$$

This equation can then be used to calculate the diffraction from lossy dielectric media.

3 Chiang and Marhefka Rim Caustic Correction

The above formulas for the diffracted field don't provide the correct diffracted field for the circular disk on the ends of a cylinder. To produce the proper diffracted fields from the end face of the cylinder, a rim caustic correction factor needs to be included in the diffraction coefficient to produce the proper fields from the cylinder ends. An appropriate caustic correction for the cylinders encountered in analyzing trees is given by Chiang and Marhefka in [11]. The new diffraction coefficients for the perfect electrical conducting (PEC) case are given by:

$$D_{s,h} = \frac{-e^{-j\pi/4}}{2n\sqrt{2\pi k} \sin \beta_0} \left\{ \left[\cot \left(\frac{\pi + (\Phi - \Phi')}{2n} \right) + \cot \left(\frac{\pi - (\Phi - \Phi')}{2n} \right) \right] \mp \left[\cot \left(\frac{\pi + (\Phi + \Phi')}{2n} \right) + \cot \left(\frac{\pi - (\Phi + \Phi')}{2n} \right) \right] T_e(U) \right\} \quad (8)$$

where:

$$T_e(U) = \frac{1}{\pi} f_0(U) \sqrt{\frac{\pi U}{2}} e^{-j(U - \frac{\pi}{4})} \quad (9)$$

and:

$$f_0(U) = \pi \left[\frac{2}{\pi} - H_1(U) + jJ_1(U) \right]. \quad (10)$$

The functions $J_1(U)$ is a Bessel functions of argument U and order 1 and $H_1(U)$ is a Struve function of argument U and order 1 where:

$$U = ka\hat{n}_e \cdot (\hat{s}' + \hat{s}). \quad (11)$$

For dielectric materials, the diffraction coefficient including caustic correction is given by:

$$D_{e,h} = \frac{-e^{-j\pi/4}}{2n\sqrt{2\pi k} \sin \beta_0} \left\{ \left[\cot \left(\frac{\pi + (\Phi - \Phi')}{2n} \right) + \cot \left(\frac{\pi - (\Phi - \Phi')}{2n} \right) \right] + \left[R_o^{e,h} \cot \left(\frac{\pi + (\Phi + \Phi')}{2n} \right) + R_n^{e,h} \cot \left(\frac{\pi - (\Phi + \Phi')}{2n} \right) \right] \right\} T_e(U) \quad (12)$$

where $T_e(U)$ is as described previously. Equation (12) works well in describing the far zone fields from a disk where a flat face is always visible and will later be used extensively in analyzing the scattering from trees.

SECTION 3

Background

1 Introduction

Before the scattering from a tree can be analyzed, some background information on tree modeling is needed. In this Chapter, a summary of current methods of modeling a tree is presented. The summary includes a description of what tree components need to be considered and how these components are usually modeled. Finally, information is provided on modeling the ground.

2 Modeling of a Tree

Many different methods are used to model a tree depending on the species of the tree to be modeled and the frequency range of interest. For the purposes of this study, an attempt will be made to use average values for the tree parameters such that a wide range of tree types are represented. The primary frequency range of interest is between 0.3-1.3GHz although other frequencies are studied.

Due to the low frequencies of interest, simplifications can be made in modeling the trunk and branches of the tree. For the frequencies between 0.3-1.3GHz, the surface of the tree and branches can be treated as smooth since the roughness of the tree bark will be small compared to a wavelength. Also, the leaves and smaller branches on the tree are ignored when modeling the trunk and branches. However, for a complete

model of a tree, the leaves and small branches need to be accounted for. The only remaining features of the tree are the trunk and the larger branches. The trunk and branches are then modeled as dielectric cylinders with a single finite length cylinder representing the trunk and smaller finite length cylinders representing the larger branches. There are many different methods used to pick the height, diameters, and dielectric properties of the cylinders. The different techniques of picking these parameters depend largely on the tree species and what seems to work.

The choice of cylinder sizes used to model the tree trunk has been reported by many authors. Specifically, formulas by M. O. Kolawole [12], and G. Sun and D. S. Simonett [13] are summarized here. Kolawole uses a simple relationship between the diameter of the tree at breast height (DBH) to the tree height h and effective height h_e given by:

$$DBH = 0.00532 + 0.0172h \quad (13)$$

$$h_e = \frac{2}{3}h \quad (14)$$

where all dimensions are in meters. G. Sun and D. S. Simonett use another relationship between the DBH of a tree and the tree height given by:

$$DBH = 0.00532 + 0.0172h \quad (15)$$

$$h_u = 0.594h - .82 \quad (16)$$

$$h_e = h_u + \frac{2}{3}(h - h_u) \quad (17)$$

where again all dimensions are in meters. In Equation (17), h_u is the distance from the ground to the widest part of the crown. The parameter h_e is the length of the dielectric cylinder that is used to model the trunk of the tree, i.e., the effective height of the tree. Usually, the diameter of the tree (DBH) is known and is used to solve for the heights h_u and h_e . These relationships between the tree diameter and effective height are used repeatedly in modeling tree trunks.

While there is information on the dimensions of the tree trunk used for modeling, there is little discussion of the dimensions of branches. The literature is short on

details for the lengths and diameters that are used to model tree branches. Therefore, an intuitive approach for selecting diameters and lengths will be used based upon the exact modeling needs when analyzing their scattering. As a result, the discussion of the lengths and diameters of branches for modeling will be postponed to the discussion of branch scattering.

3 Dielectric Properties of Trees

In addition to knowing the size of a tree, its dielectric properties must also be known for realistic modeling. There have been many papers that present measured dielectric constants of trees [14, 15]. The daily and seasonal variations of the dielectric constants of trees have also been examined by several authors and for different tree species [14, 16]. But, for the purposes of this study, the variation in tree parameters will be ignored and instead a set of values for the dielectric constants will be used that should cover typical values including the variations in the dielectric constant. In theory, however, the variations can be taken into account.

The modeling of the dielectric properties of wood can be divided into two groups, the use of a single homogeneous piece of dielectric and the use of multiple layers of dielectric to simulate the individual parts of the tree structure. While the simplicity of modeling the wood as a single layer of dielectric is apparent, it can be argued that the multilayer approach is more accurate since it is more faithful to the actual structure. This is because the dielectric constant is lower on the inside of a tree. The dielectric constant then increases as a function of radius before decreasing to a lower dielectric constant near the bark. This profile of the dielectric constant forms the basis of the 3-layer modeling. Both methods of modeling a tree as single and multiple layers are presented here. In Table 1, the relative dielectric constants of wood used in single layer modeling are presented. The wood is assumed to have no magnetic properties such that the permeability of the wood μ_c is equal to μ_0 . The wide range of values in Table 1 shows the large differences in modeling trees with

Table 1: Dielectric constants used to model the dielectric properties of wood at L-Band from the literature.

ϵ_r	author(s) and reference
5-j1.5	F. Amir, et. al. [17]
12.4-j4.9	M.A. Karam and A.K. Fung [18]
18-j6 5-j1.7 24-j8	Kyle McDonald [19]
4-j1	Tsan Mo and J.R. Wang [20]
20-j5	Guo-qing Sun, et. al. [21]

Table 2: Dielectric constants used to model the dielectric properties of wood at L-Band from the literature for multilayered modeling.

layer	layer thickness (cm)	ϵ_r
inner layer	10	15-j7
outer layer	0.5	4-j1

dielectric materials. The large variation in dielectric constants is explained by the wide range of tree species that have been measured. The variation in Table 1 is also due to the seasonal and daily variations in the dielectric constants of wood mainly due to the change in moisture content of the wood. In Table 2, the relative dielectric constants and layer information are presented for 2-layer modeling. In addition to using a 2-layer model, a third layer can be added to to simulate more accurately the dielectric profile of the tree as mentioned previously. The use of 3-layer modeling is discussed in later chapters. The differences in modeling the cylinders as single and multiple layers are examined further in following chapters.

4 Dielectric Properties of Soil

The effect of the ground on the scattering from a tree can be of importance. Therefore, a model for the ground needs to be developed. Typically, for the primary frequencies of interest, the wavelength is long enough so that the ground can be treated as smooth. The ground is also assumed planar near the tree. The soil is then usually modeled as a homogeneous dielectric half-space. Table 3 summarizes typical dielectric properties for soil that will be used in modeling the scattering from a tree.

Table 3: Dielectric constants used to model the dielectric properties of soil at L-Band from the literature.

ϵ_r	comments and source
7-j1.5	moist soil from Michael O. Kolawole [12]
18-j5	wet soil from Michael O. Kolawole [12]
20-j0.15	soil at Ohio State University Radio Telescope [22]

SECTION 4

Scattering From Logs

1 Introduction

A model for the scattering characteristics of wood needs to be developed that can be used in the analysis of the scattering from trunks and branches. In Chapter 3, a summary of the parameters used in modeling the various parts of a tree is presented along with dielectric constants. However, due to the wide range of values that are presented, it is desired to find which values and techniques are appropriate for the cases of interest in this analysis. To do this, the parameters and ideas that are presented in Chapter 3 are used to develop a model that is appropriate to the cases of interest in this analysis.

To develop this model, the scattering from a log is measured and theory is used to match the measurements. In doing this, a set of parameters for the wood is found that will allow theory to predict the scattering from the log. These wood parameters will then be used later to model the wood in more complex geometries involving branches and trunks.

To find the parameters for the wood, a method of modeling the scattering from a log is presented. First, methods of accounting for the effects of log roughness and dielectric constant on the calculated scattered field of the log are discussed. Then measured results for the RCS of three logs are presented. The methods of modeling a log using the roughness and dielectric constants are then applied to compare to

the measured RCS of the logs. The resulting values for the dielectric constants and roughness used to match the measured log RCS provides a set of values for the wood that can be used to model the characteristics of wood in branches and trunks.

2 Theory of Modeling a Log

To model the scattering from a log, three things are taken into account. First, a model for the dielectric properties of the wood must be found that accurately represents the dielectric constants of the wood as a function of frequency. Then, a method of accounting for the roughness of the log's bark must be chosen depending on the frequencies of interest. Finally, the dielectric and roughness information must be included into a solution for the scattering for a finite length, rough, dielectric cylinder.

2.1 Dielectric Properties of Wood

To model the dielectric properties of wood, the variation of the dielectric constant with frequency must be taken into account. Various dielectric constants have been published to model wood and are summarized in Table 1. These values represent typical values used in L-band. However, a method of calculating the scattered field over a broad range of frequencies is of interest. There are many papers that present data on the dielectric constant of wood in specific frequency bands but there is little data available that present the dielectric constant as a function of frequency. Therefore, a method will be used to vary the dielectric constant as a function of frequency using the values as presented in Table 1.

For the purposes of this analysis, the real part of the dielectric constant will always be held constant with frequency. This is done to simplify the analysis and is consistent with the small variation in the real part of the dielectric constant with frequency shown in the literature.

Although the real part of the dielectric constant varies little, the imaginary part has been shown to vary considerably with frequency[14]. Therefore, a simple method of varying the imaginary part of the dielectric constant with frequency will be discussed and compared with holding the dielectric constant fixed with frequency. Taking the values from Table 1 and by knowing the approximate frequency at which the dielectric constants were measured, the conductivity of the material at that frequency can be found by:

$$\sigma_e = \text{Imag}[\epsilon_r] \times \omega_t \epsilon_0 \quad (18)$$

where ω_t is the frequency at which the relative dielectric constant ϵ_r is measured. The value of σ_e from Equation (18) is then held constant as the frequency is varied. The relative dielectric constant ϵ_r then varies with frequency as:

$$\epsilon_r = \frac{1}{\epsilon_0} \left(\epsilon + \frac{\sigma_e}{j\omega} \right) \text{ where } \sigma_e \text{ and } \epsilon \text{ are fixed.} \quad (19)$$

This method of varying the dielectric constant will be compared to the method of holding the dielectric constant fixed with frequency later.

2.2 Effect of Wood Roughness

The roughness of the log bark also must be taken into account. While the roughness of the bark will be small, as the frequency increases the effect of the roughness will increase. For the logs and frequencies of interest, an appropriate model for treating the roughness is used where the roughness factor is a function of the surface height variability[23]. This model is only valid for slightly rough surfaces where the main reflection from the surface is the specular component and the diffuse scatter caused by the surface roughness is small. The model modifies the reflection coefficient by:

$$\Gamma_{rough} = \delta_s \Gamma \quad (20)$$

where:

$$(\delta_s)^2 = e^{-(\Delta\Phi)^2} \quad (21)$$

$$\Delta\Phi = \frac{4\pi\Delta h}{\lambda} \sin \gamma. \quad (22)$$

In Equations (20)- (22), Γ is the reflection coefficient from the smooth surface, Γ_{rough} is the modified reflection coefficient for the rough surface, Δh is the maximum height difference between two points on the rough surface, and γ is the angle between the incident wave and the surface. This formula is valid only when the height variation Δh is less than $\frac{\lambda}{8 \sin \gamma}$ which is true for the cases of interest. Values of Δh will depend on the type of wood and number of bumps in the wood bark and will be found later when the wood measurements are modeled.

2.3 Solution of Dielectric Cylinder Scattering

The scattering from a finite length dielectric cylinder must be calculated. To accomplish this, the solution for scattering by a multilayered infinite length dielectric cylinder described in Appendix B is used. Since this solution is for infinite length cylinders it must be modified for finite length cylinders. A simple method of doing this is to convert the 2-dimensional echo width to the 3-dimensional radar cross section (RCS). This is accomplished by the well known formula:

$$\sigma_{3D} = \frac{2L^2}{\lambda} \times \sigma_{2D} \quad (23)$$

where L is the length of the finite length cylinder. This conversion gives accurate answers when the length L is much greater than the cylinder diameter and $L \gg \lambda$.

3 Measurement of the Radar Cross Section of Logs

To measure the radar cross section of a log, a tree approximately 4" (0.10m) in diameter was cut down from the woods near the Ohio State University Big Ear radio telescope where forest propagation measurements have been made in the past. The tree was a sugar maple which comprise a large number of the trees in the

woods. The tree trunk was cut into 3 lengths approximately 24" (0.61m) long. The diameters of the logs varied from approximately 3.5"-4" (0.089-0.10m). The bark of the logs was fairly smooth with main grooves in the bark approximately 2-3mm deep. The branches were cut off leaving a few small bumps on each log. After the tree was cut into logs, the ends and the bark were spray coated with shellac to reduce moisture loss due to evaporation. Although the layer of shellac has a slightly different dielectric constant than the wood, the layer of shellac was very thin and, therefore, is thought to have negligible impact on the wood dielectric properties. Also, after the logs were removed from the woods, they were wrapped in plastic bags to further reduce water loss.

The logs were then measured in a compact range the next day from 2-18GHz. The logs were measured in this frequency range due to necessity of available equipment at the time of the measurements. Although these frequencies are higher than the primary frequencies of interest, the results obtained by the measurements should be applicable to the frequencies between 0.3-1.3GHz. The measurements consisted of specular impulse responses from the smoothest section of the logs (i.e., the side with the fewest bumps). The measurements were then repeated 19 days later to allow for some drying of the logs to see how a small decrease in the water content of the logs would affect the RCS. For the second set of measurements, the orientation of the log was maintained as close as possible to the original measurements. Both days of measurements are combined and are shown for the three logs in Figures 2, 3, and 4. The RCS is represented in decibels with respect to a square meter for the transverse magnetic (TM) case with the electric field aligned with the log axis and the transverse electric (TE) case with the magnetic field aligned with the log axis.

It is seen from the measurements, that the RCS of each log didn't change appreciably for the 2 days of measurements at the frequencies below approximately 10GHz. But above 10GHz, the RCS for the 2 days of measurements for each log tended to change. This variation can be attributed to the difficulty in precisely align-

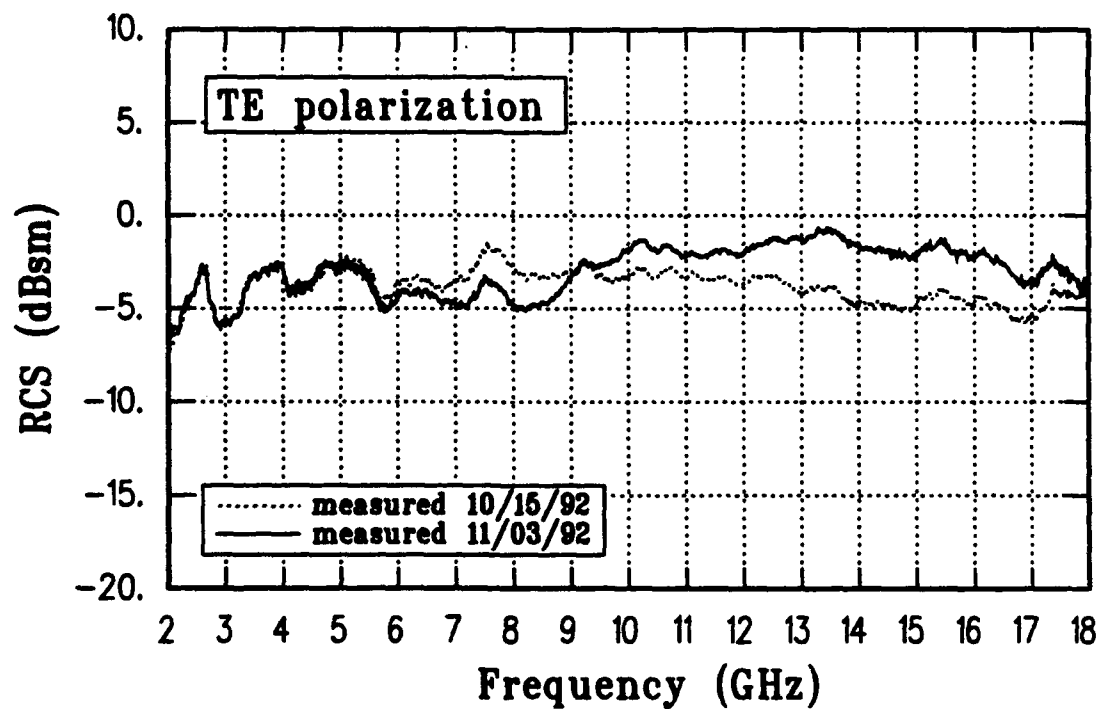
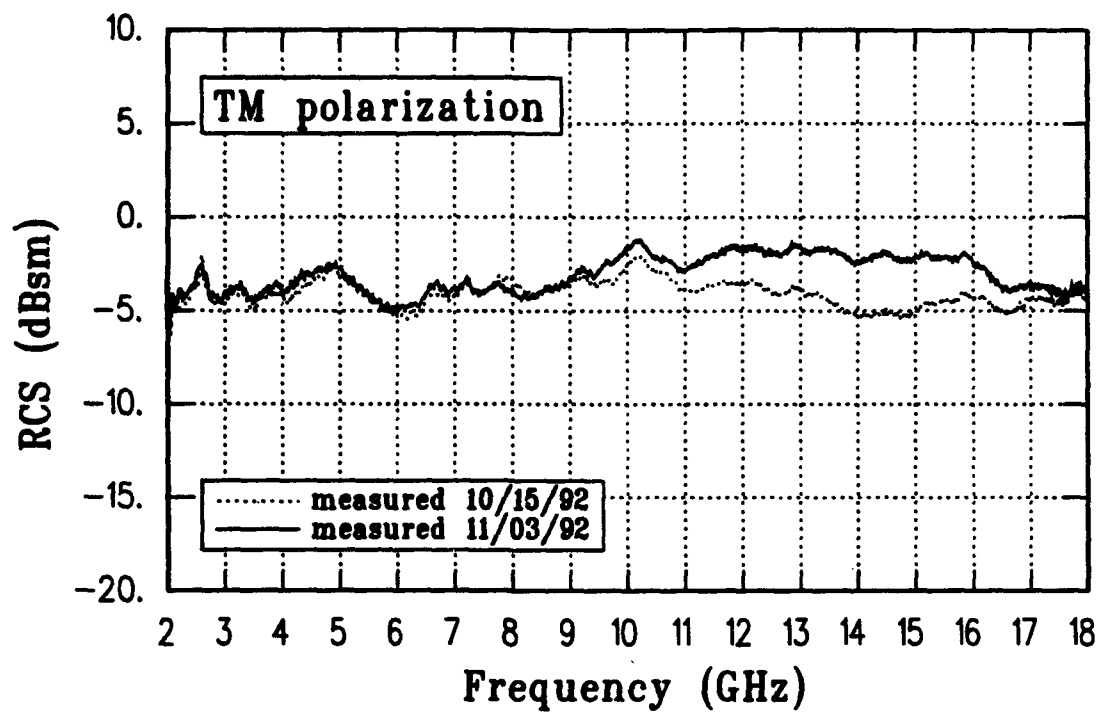


Figure 2: Measured RCS of log #1 for TM and TE polarizations.

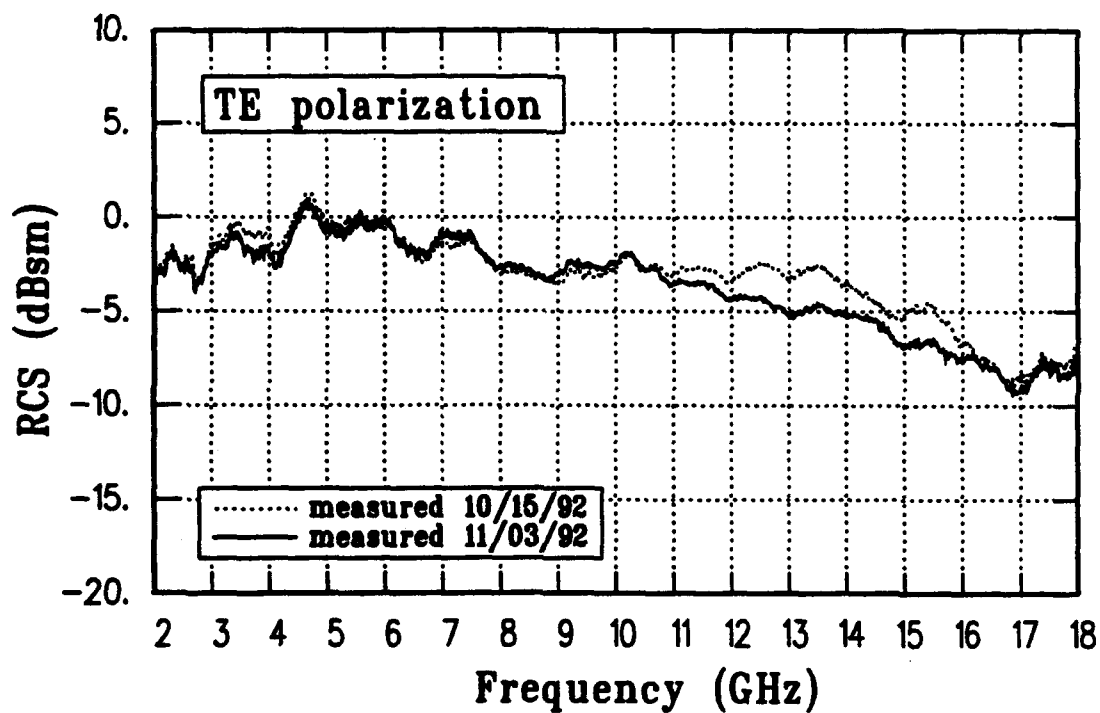
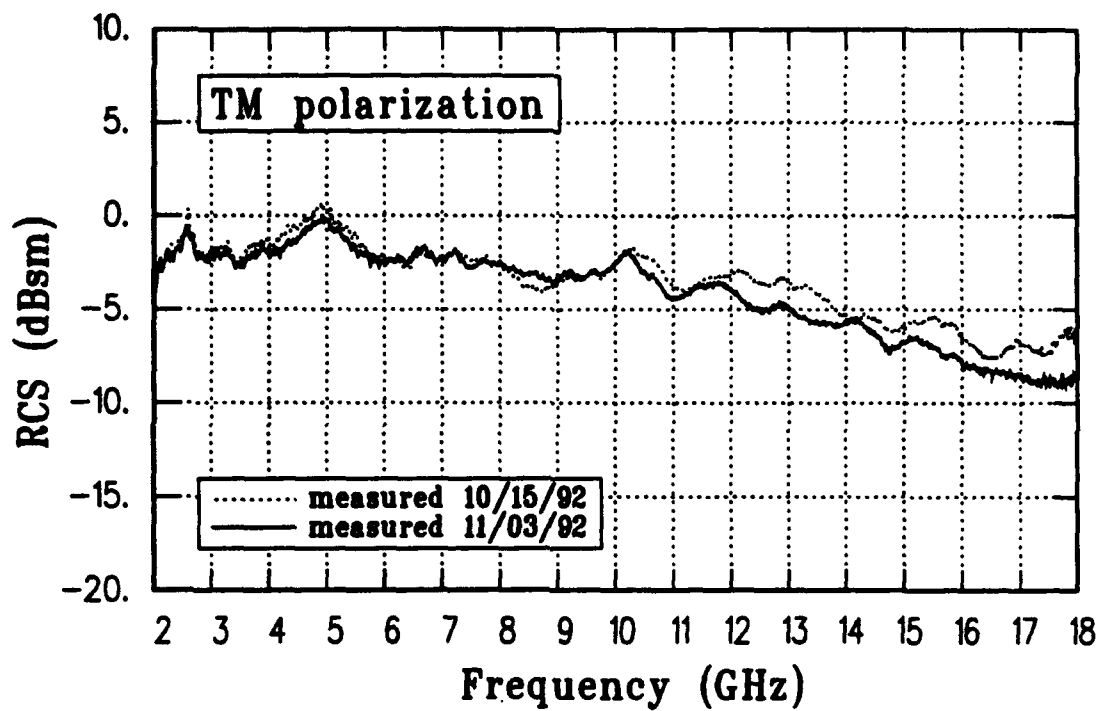


Figure 3: Measured RCS of log #2 for TM and TE polarizations.

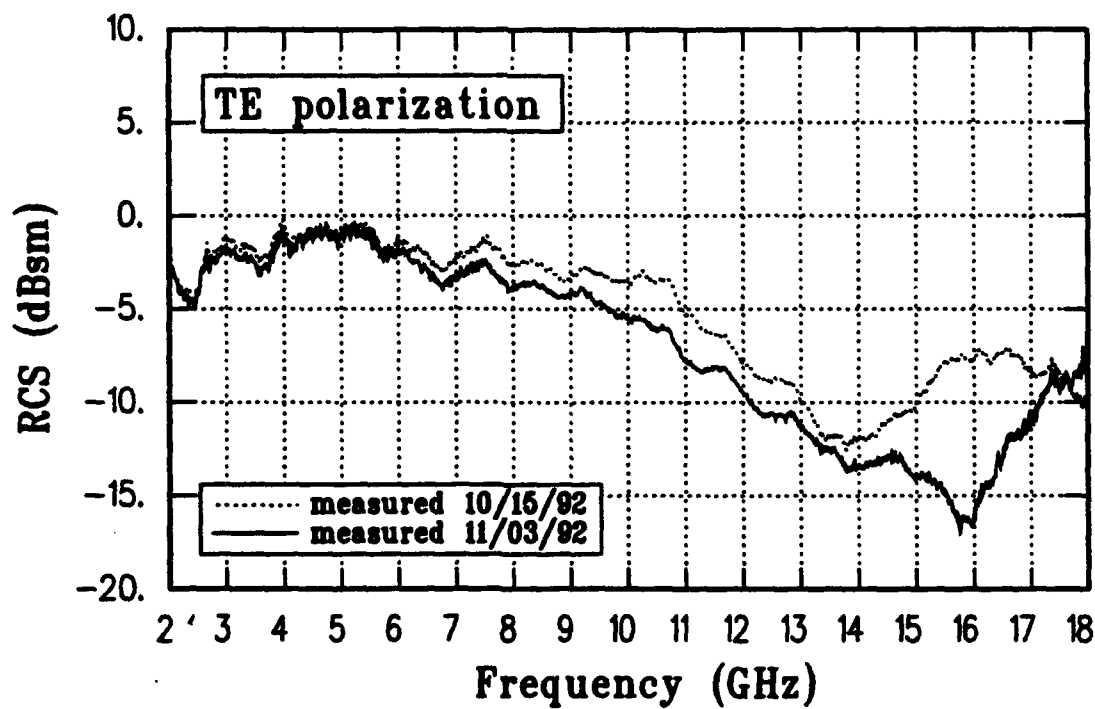
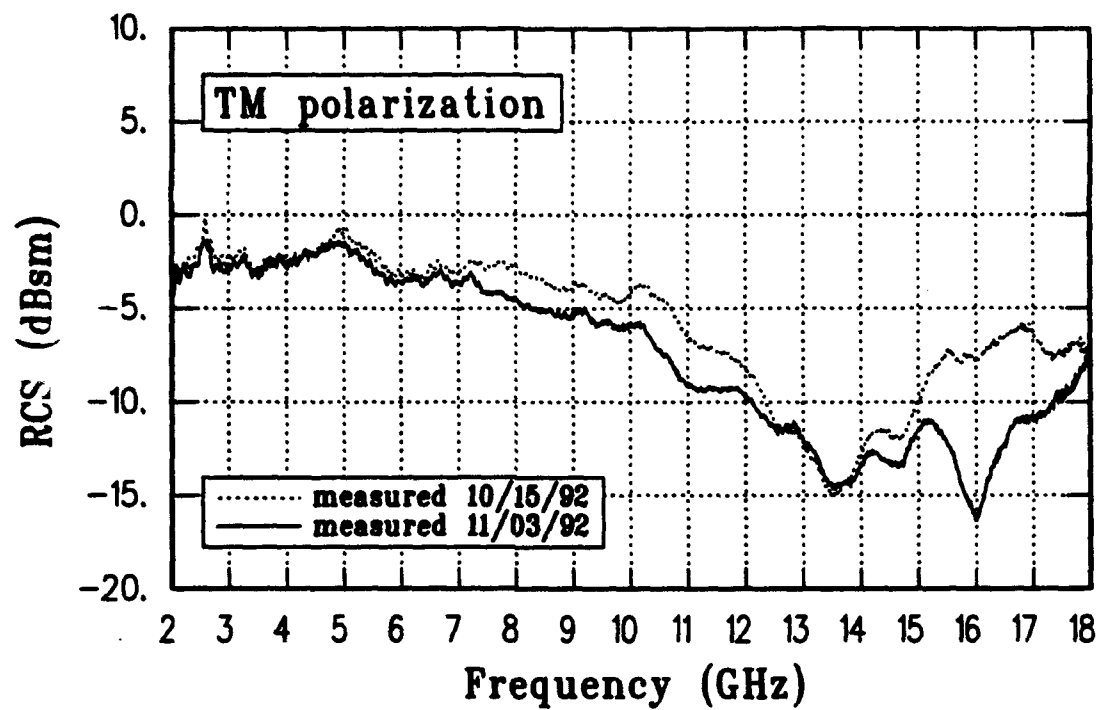


Figure 4: Measured RCS of log #3 for TM and TE polarizations.

ing the log to the same location as the previous days measurement since a rotation about the long axis of the log was difficult to control. Since the logs don't have a perfectly circular cross and are not entirely straight, a small rotation causes a change in the surface characteristics of the log being measured. Also, the resulting small rotation of the log caused a different part of the log surface to be measured, thereby, the effective surface roughness changed slightly. Since the surface roughness of the log has an larger effect on RCS at higher frequencies as shown by Equation (22), the small rotational error caused a large difference on the RCS at higher frequencies. By the same reasoning, the small differences in the data for the 2 days of measurements at the lower frequencies show that the surface roughness has a small effect on the RCS of the logs at the lower frequencies and that any drying of the logs also had a small effect.

4 Comparison of Log RCS with Theory

It is now desirable to try to relate the different techniques of modeling logs from Section 2 to the measurements of Section 3. To accomplish this, the surface roughness model described in Equations (22) and (20) is used to modify the echo width in the exact solution given by Equation (76). The scattered field in Equation (76) was multiplied by the coefficient δ_s . This results in the echo width for a rough cylinder $\sigma_{2D-rough}$ where:

$$\sigma_{2D-rough} = \frac{2\lambda}{\pi} \left| \delta_s \sum_{n=0}^{\infty} e_n D_n \cos n\phi \right|^2. \quad (24)$$

The echo width given by Equation (24) is then modified from the two-dimensional (2D) echo width to the three-dimensional (3D) RCS by Equation (23). Dielectric constants are then chosen from Table 1 and are used to model the log as a single-layer homogeneous dielectric cylinder. The length of log #2 is 27.5" (0.699m) and an average value for the diameter for log #2 of 3 $\frac{5}{8}$ " (0.092m) is chosen and used to model the log. Two cases are run, one where the conductivity σ_c is held fixed and the other where the dielectric constant ϵ_r is held fixed. The two cases are shown in

Figure 5 for $\epsilon_r = 24 - j8$, and for $\text{Real}[\epsilon_r] = 24$ and $\sigma_e = 0.5563$. Figure 5 shows that the two curves follow the same general trend, however, the constant σ_e curve shows a stronger creeping wave component than the constant ϵ_r curve. The creeping wave component can travel easily around the smooth cylinder used in the solution. But, since the roughness of tree bark will quickly attenuate the creeping wave component, the creeping wave component of the solution must be removed by processing the scattered field. The creeping wave is removed by processing the impulse response of the theoretical solution and filtering out the creeping wave. The processed results for the same cylinders as calculated in Figure 5 are shown in Figure 6. By examining Figure 6, once the creeping wave component is removed from the scattered field, it doesn't matter whether σ_e or ϵ_r is held constant with frequency since the results are the same once the creeping wave is removed. Therefore, since both methods produce the same result after the creeping wave component is removed, future calculations will keep the dielectric constant ϵ_r constant with frequency when the creeping wave component is removed.

Since the three logs came from the same tree trunk, the measured RCS can help illustrate the variations in the RCS of a tree. To show this variation, the RCS of the three logs is converted to the 2D echo width by equation (23). This is done to remove the effect of the different log lengths. The resulting echo widths for the three logs and 2 different days of measurements is shown in Figures 7 and 8 for TE and TM polarizations, respectively. The purpose of these plots is not to show the individual echo width for each log measurement but to show the variation in the scattering from the logs. At the low frequencies near 2.0GHz, the echo width varies about 4dB while at higher frequencies the fluctuation is almost 15dB. This shows that for the same tree trunk, the RCS of different sections will vary by several dB. Due to this fluctuation, it is difficult to model the RCS of a log (or tree trunk) with a high degree of accuracy. Therefore, it can be expected that any modeling of a tree trunk will only be accurate to within a few dB.

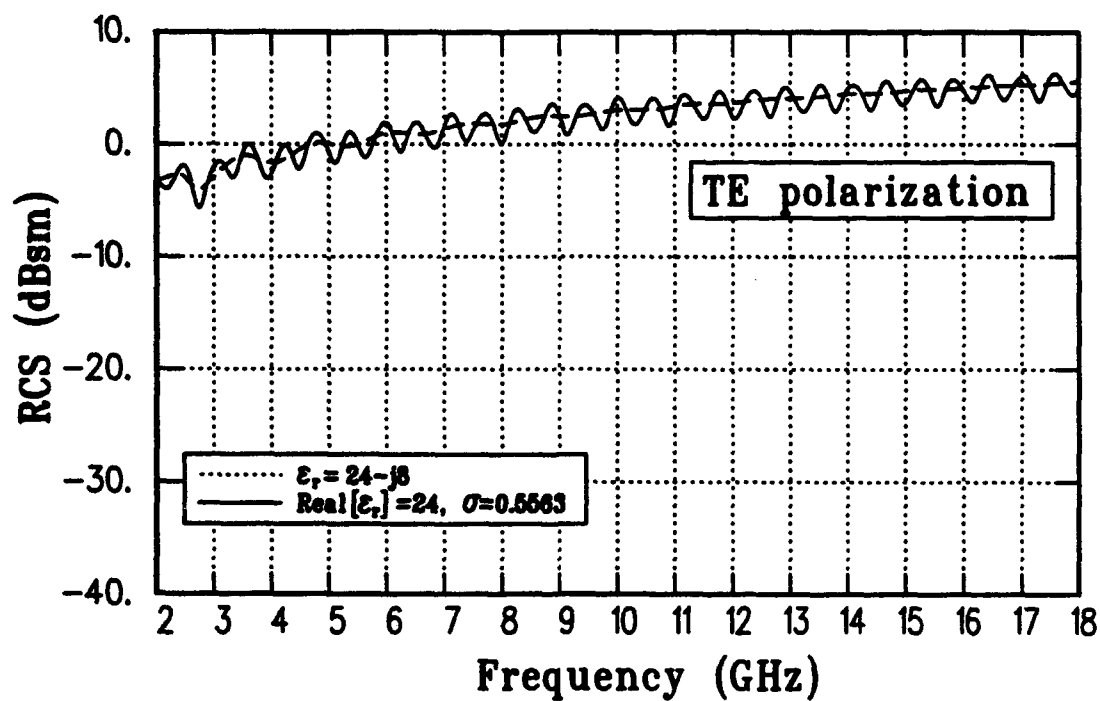
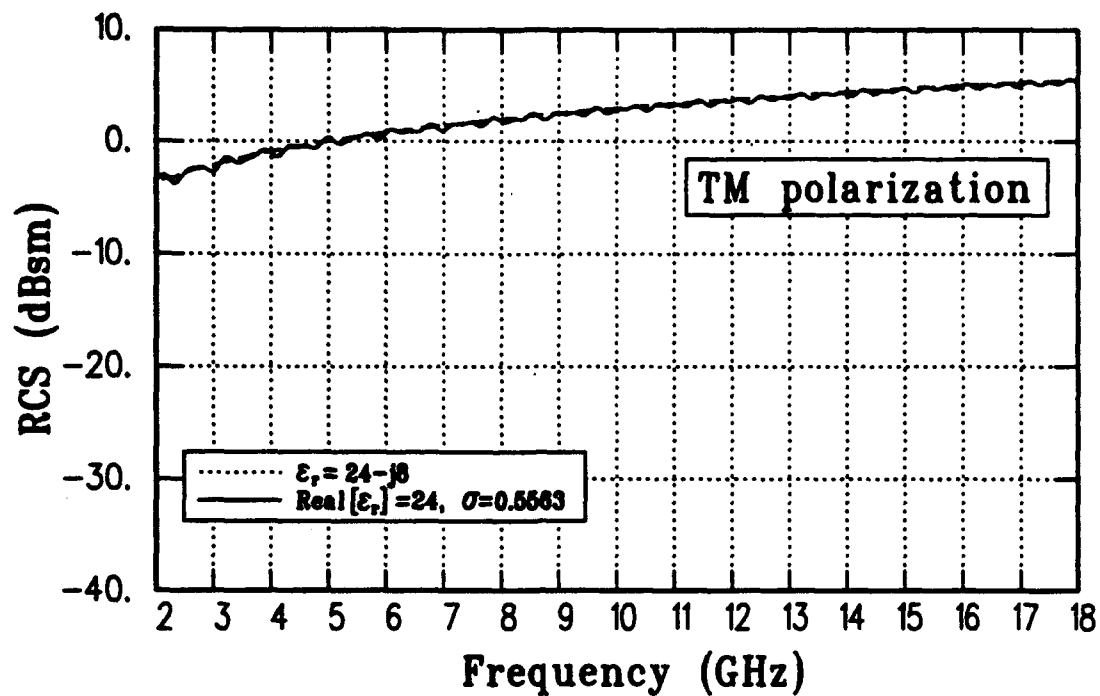


Figure 5: Comparison of the RCS of the dielectric cylinder used to model a log for relative dielectric constants of $\epsilon_r = 24 - j8$ and $\text{Real}[\epsilon_r] = 24, \sigma_e = 0.5563$.

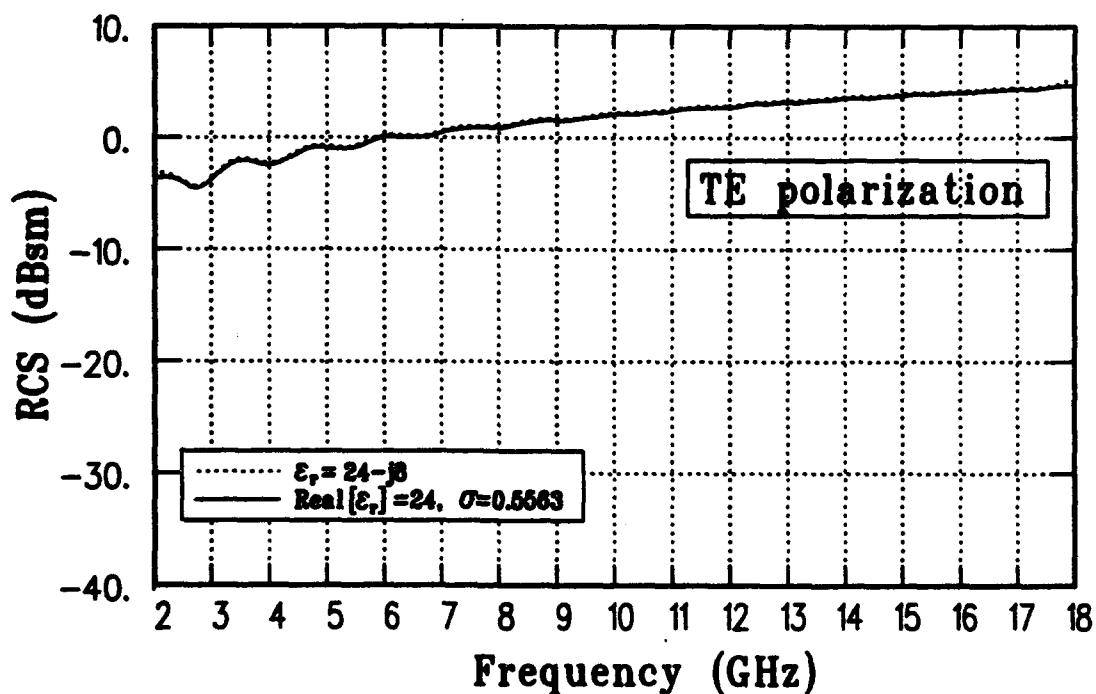
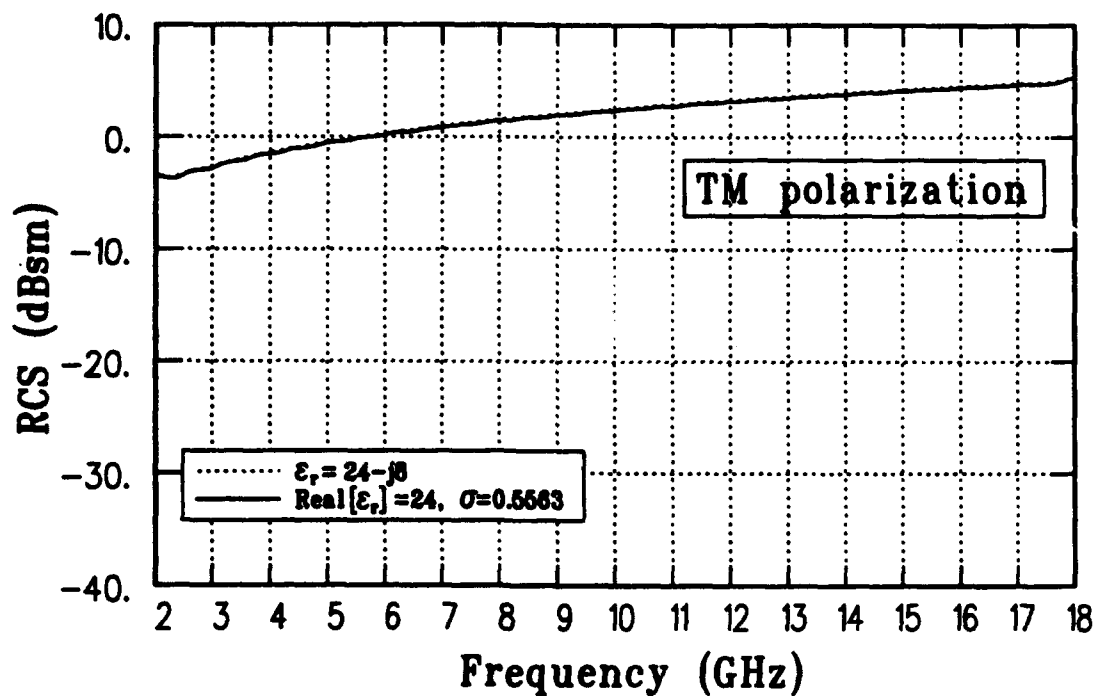


Figure 6: Comparison of the RCS of the dielectric cylinder used to model a log for relative dielectric constants of $\epsilon_r = 24 - j8$ and $\text{Real}[\epsilon_r] = 24, \sigma_r = 0.5563$ processed to remove the creeping wave component.

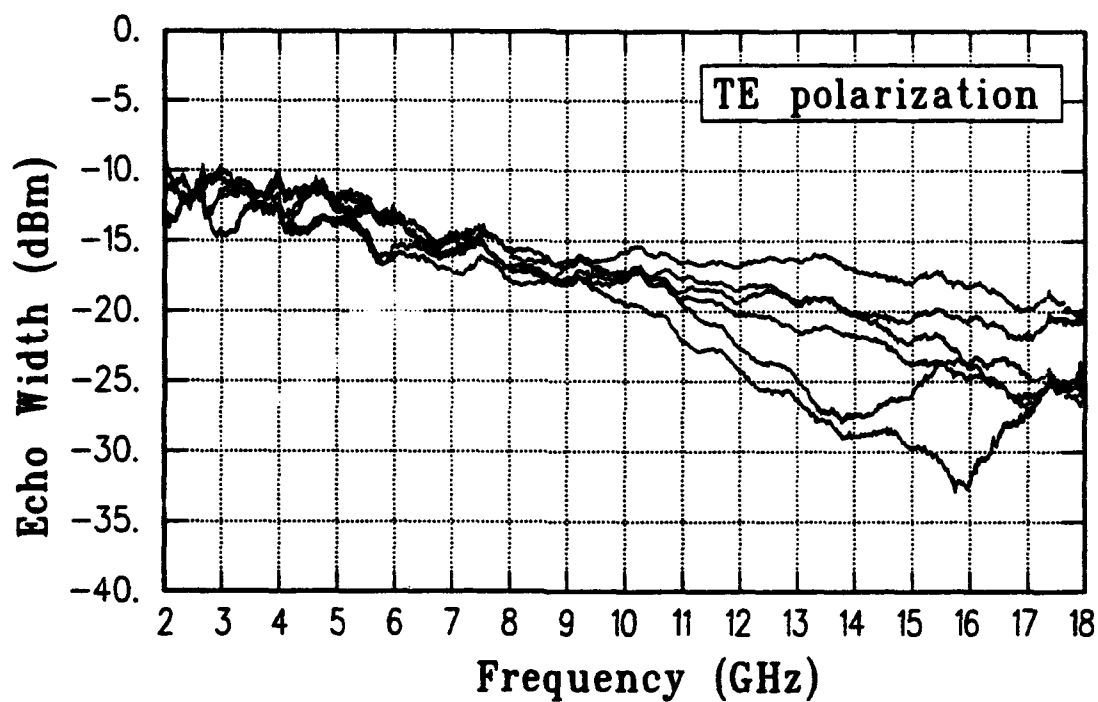


Figure 7: Echo width for TE polarization of logs #1, #2, and #3 from processing RCS measurements to show variation in echo width for logs from the same tree.

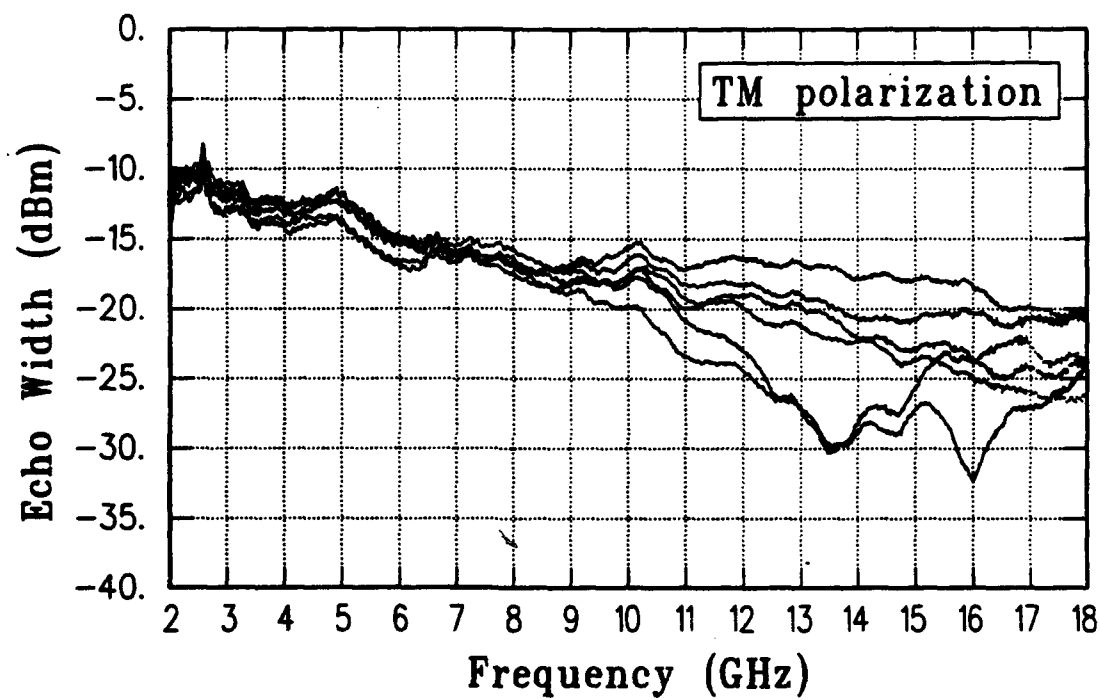


Figure 8: Echo width for TM polarization of logs #1, #2, and #3 from processing RCS measurements to show variation in echo width for logs from the same tree.

The roughness modification for slightly rough surfaces as described in Equations (22) is then added to the modeling of the logs. In Figures 9 and 10, the echo width for the 3 log measurements are compared with two different dielectric models for the logs. The models are for dielectric constants of $\epsilon_r=12.4-j4.9$ and $\epsilon_r=24-j8$ with roughness factor (Δh) of 2mm and 3mm since the log roughness is between 2mm and 3mm. The models for the logs are within approximately 2dB lower than the measured echo width at the lower frequencies and are within the range of measurements at the higher frequencies. Since it is difficult to model the logs more accurately, these dielectric constants are considered adequate to represent the range of dielectric properties for the trees of interest in modeling. Based on these results, for future calculations of the RCS from wood, the dielectric constants used to model the wood will either be $\epsilon_r=12.4-j4.9$ or $\epsilon_r=24-j8$. Since using roughness factors (Δh) of 2-3mm falls within the measured results at higher frequencies, when the roughness is important the value of Δh will be between 2mm and 3mm. These values should provide accurate models for actual wood.

The surface roughness has a significant effect on the RCS of the logs at higher frequencies while at lower frequencies, the surface roughness has a smaller effect. In Figures 9 and 10, a change in Δh from 2-3mm causes a large change in the echo width of about 10dB at 18GHz. This sensitivity is further illustrated in Figure 11 which shows the roughness effect for various values of Δh . It is seen that the roughness only has an effect of about 3dB at 6GHz for a $\Delta h=3$ mm. Therefore, when the roughness factor is removed from the echo width calculations, the difference between the theory and the measurements will be within the variation of the measured echo width for the logs of 4dB at 6GHz. Therefore, the roughness factor can be ignored at frequencies below 6GHz and the log surface can be treated as smooth without causing significant error. For the primary frequencies of interest between 0.3-1.3GHz, the effect of the surface roughness is even smaller and therefore, it can be ignored as was discussed in Chapter 3. Above 6GHz, the sensitivity to the roughness factor is too great to be

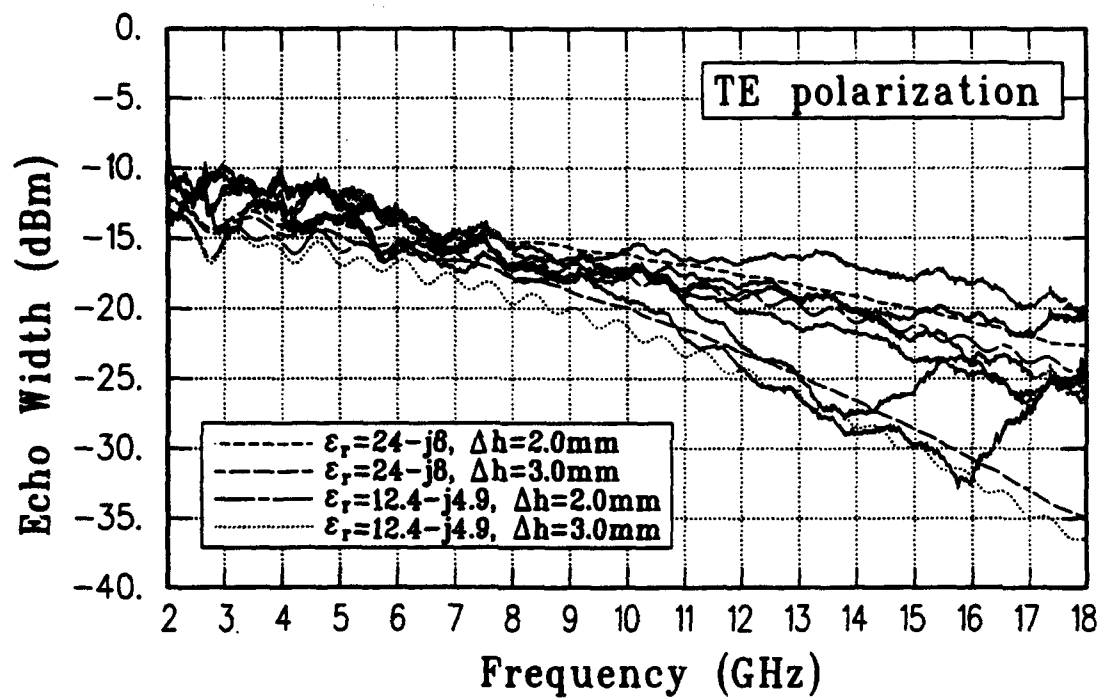


Figure 9: Echo width for TE polarization of logs #1, #2, and #3 from processing RCS measurements compared to different dielectric models for the logs.

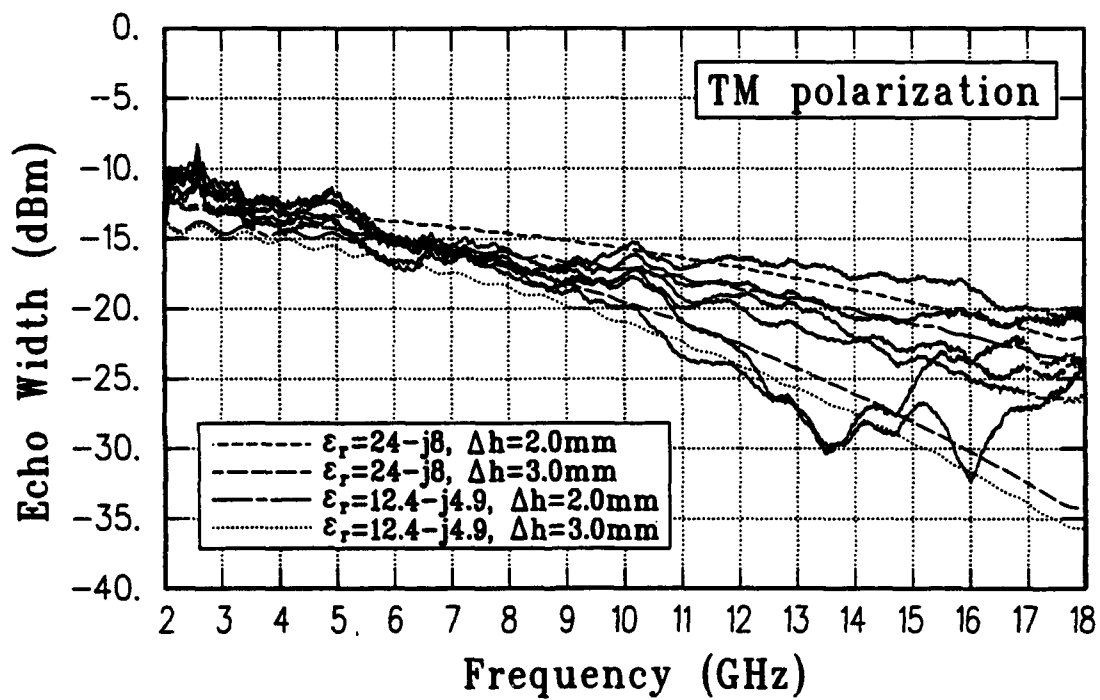


Figure 10: Echo width for TM polarization of logs #1, #2, and #3 from processing RCS measurements compared to different dielectric models for the logs.

used in modeling and, therefore, is not recommended since it is difficult to measure the Δh value and then calculate the RCS. Instead the value of Δh must be chosen to match the measurements. Therefore, this technique of modeling the roughness of the log is not recommended at high frequencies.

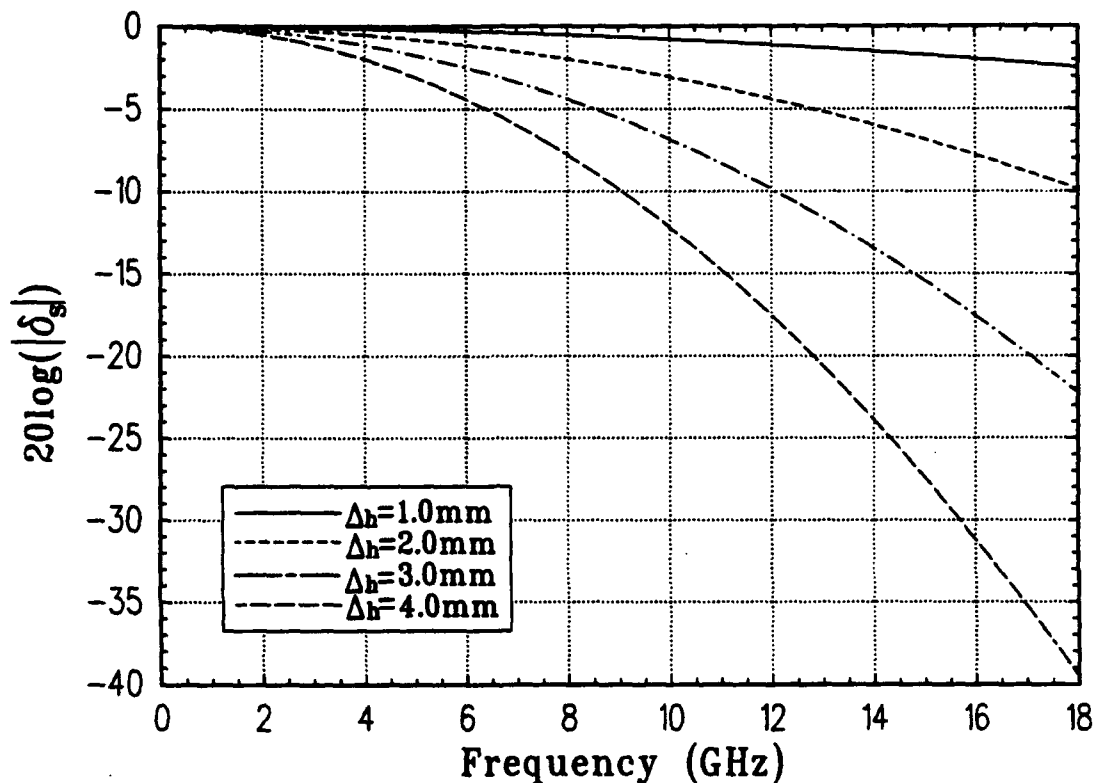


Figure 11: Variation of roughness factor δ_s for different values of Δh as a function of frequency.

However, if the roughness factor is varied until the calculated RCS match the measured RCS, the modeling of the log closely approximates the measured RCS. In Figure 12, comparison between the measured and calculated RCS for log #2 is shown. For these plots, the dielectric constant is chosen as $\epsilon_r = 24 - j8$. The surface roughness is found by adjusting Δh until the calculated RCS matched the measured data. While this method seems rather unscientific, for the log geometry, there is no way to actually calculate the roughness factor Δh directly due to the complexity of

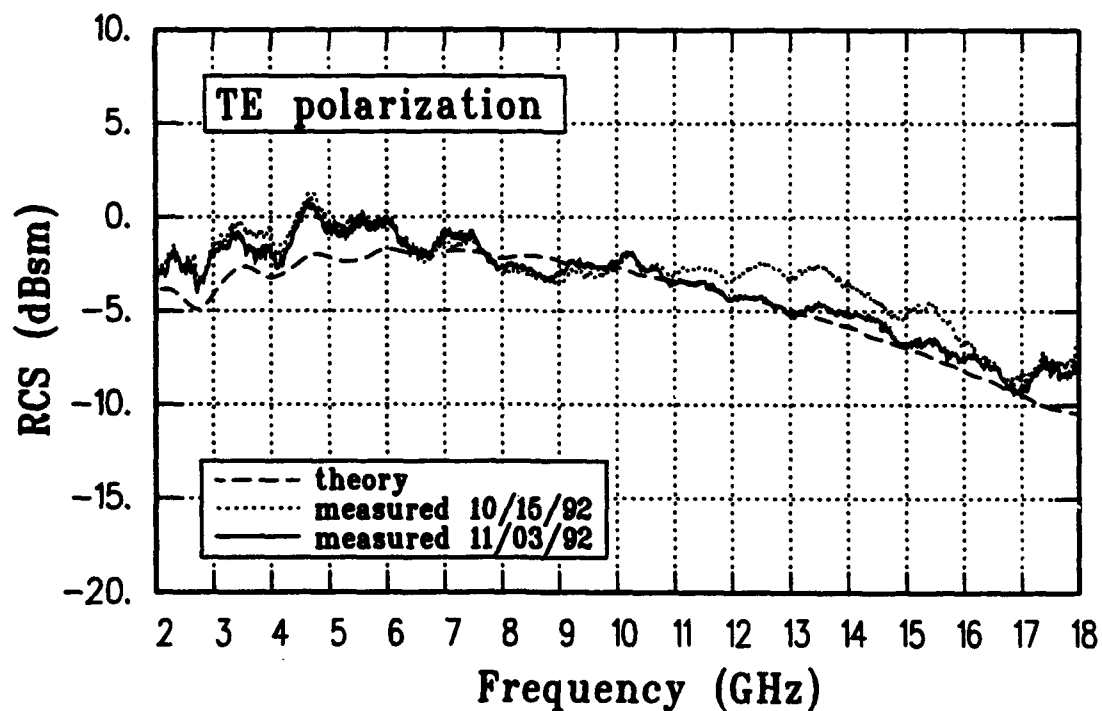
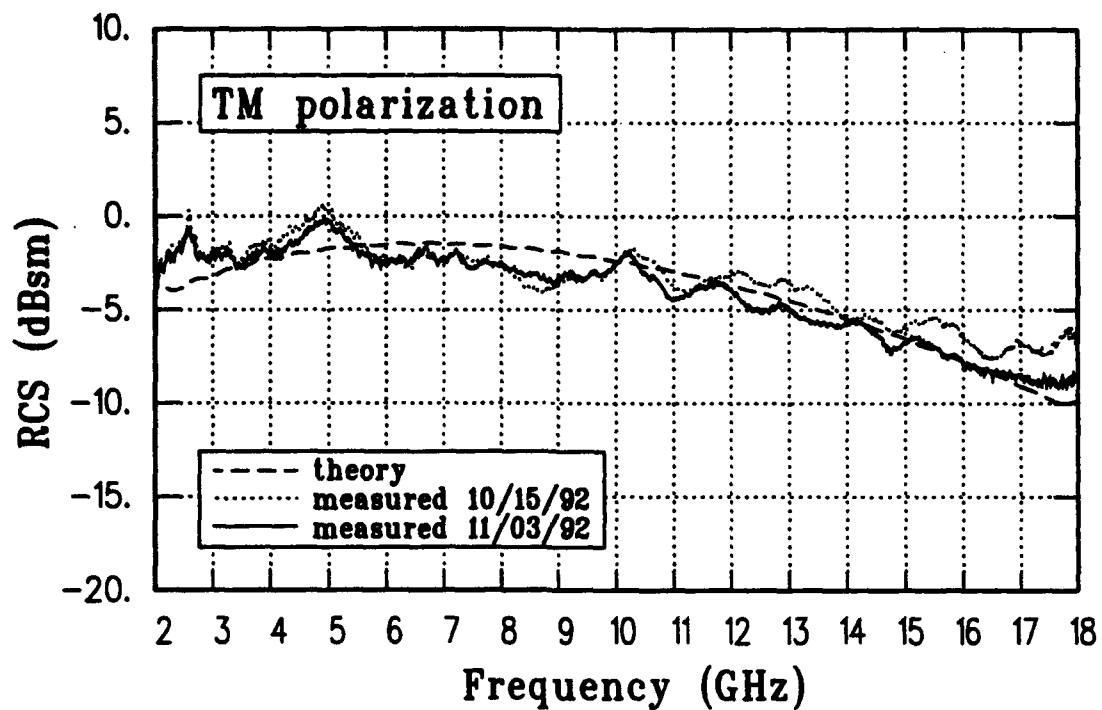


Figure 12: Comparison between the measured and calculated RCS of log #2. For the modeling, the parameters are $\epsilon_r=24-j8$ and $\Delta h=0.0025m$

the log surface. Therefore, once a value is found by trial and error, it is verified that this value is reasonable for the log. A roughness $\Delta h = 0.0025\text{m}$ is needed to match the measured data. This roughness is on the same level of roughness that can be measured for the bark of between 2-3mm which doesn't include large features such as bumps from branches. Therefore, it is felt that this is a reasonable value for the roughness factor Δh . Also, for Figure 12 the creeping wave component is processed out as discussed previously. So, this method of accounting for the surface roughness can provide good agreement with measurements. However, as stated earlier, since the RCS from modeling the log is very dependent on the surface roughness Δh , and there is no way to measure Δh directly, this method of modeling the logs at higher frequencies should be used with caution.

5 Summary

Methods of calculating the effect of the dielectric constants and roughness of a log on the calculated scattered field is presented. The measured RCS of three logs is then shown. By comparing the theory of calculating the RCS of a log to the measurements, the effect of roughness and dielectric constant is observed. It is found that the roughness of the bark had a significant contribution to the RCS of the logs above approximately 6GHz but had a much smaller impact at lower frequencies. Therefore, for future modeling, the surface roughness can be ignored for frequencies below 6GHz. The effect on varying the dielectric constant with frequency versus holding it fixed is also examined. It is found that when holding the dielectric constant fixed, the creeping wave component decreased with frequency as compared to the case where the dielectric constant varies with frequency in which case the creeping wave remained significant at higher frequencies. However, the method used to calculate the scattered field was for a smooth cylinder and, therefore, a creeping wave could be supported. But for an accurate modeling of the log to fully account for the surface roughness, the creeping wave needs to be removed since the rough log

surface reduces the creeping waves. When the creeping wave is removed, the results for a constant and a varying dielectric constant are identical. Therefore, for future modeling, the dielectric constant can be chosen to vary or remain fixed and will produce the same results as long as there is no creeping wave components. Finally, the effect of choice of the dielectric constants is examined. It is found that using dielectric constants of $\epsilon_r = 24 - j8$ or $\epsilon_r = 12.4 - j4.9$ for the wood produced the correct scattered field magnitude within approximately 2dB of the measured values. The difference of 2dB is shown to be small and a good enough match since the echo widths of the three logs vary by more than 4dB for logs from the same tree trunk. Therefore, these values for the wood dielectric constants will be used extensively to model wood in later chapters.

SECTION 5

Scattered Fields in the Vicinity of a Tree Trunk

1 Introduction

The scattered fields in the vicinity of a cylinder used to model a tree trunk are of interest. In Chapter 4, the modeling of a log as a dielectric cylinder is discussed and agreement between the modeling and measurements is shown. This chapter discusses the scattered field in the vicinity of the dielectric cylinder used to represent the tree trunk. The dielectric parameters used for the dielectric cylinder are based in part on the results of the previous chapter and also on the modeling discussed in Section 2. The purpose of the analysis is to look for trends in the near-field scattering of a cylinder for various geometries.

The analysis is comprised of two parts. The first part involves studying the near field scattering of a cylinder representing a tree trunk using an exact numerical solution of a multilayered dielectric cylinder of infinite length under plane wave incidence. Various combinations of cylinder parameters are used to discover trends in the scattered patterns for various cylinder geometries. The second part of the analysis involves comparing the applicability of the above exact solution for infinite length cylinders with normal incidence to finite length cylinders with oblique incidence. This is done to find a range of angles over which the solution for an infinite

length cylinder with normal incidence can be used for a finite length cylinder with oblique incidence. For this comparison, a UTD solution for a finite length perfect electrical conducting (PEC) cylinder alone and above an infinite ground plane with oblique plane wave incidence is compared to the above exact solution for an infinite length PEC cylinder. A UTD solution for PEC cylinders is used since a more general solution for the near field of a multilayered dielectric cylinders of finite length and oblique incidence is not presently available. From this comparison, a range of applicability is found which should be valid for the multilayered dielectric case.

2 Target Geometries

The geometry used for the analysis of infinite length cylinders is shown in Figure 13. It consists of a multilayered dielectric cylinder of infinite length with circular cross section in the x-y plane. A plane wave is incident from the negative x-axis. The solution to this geometry is discussed in Appendix B.

The geometry used in the comparison cases for oblique incidence is shown in Figure 14. The UTD solution for a finite length PEC cylinder with oblique plane wave incidence is calculated using the Numerical Electromagnetic Code - Basic Scattering Code (NEC-BSC) code [24]. This code does not accurately provide the scattered fields in the deep shadow region of a dielectric cylinder. Therefore, only the PEC case is analyzed for the finite length cylinder. The NEC-BSC code outputs the total field for a radial 180 degree cut in the forward scatter region at a constant radial distance R about the center of the finite length cylinder with the angle ϕ defined as in Figure 13.

The geometry for the case of the finite length cylinder above an infinite ground plane used to simulate the ground is shown in Figure 15. This geometry is analyzed since it's closer to the actual geometry that would occur in nature. This case produces the same type of output as the case without the ground plane but allows the height of the receiver above the ground plane to be varied.

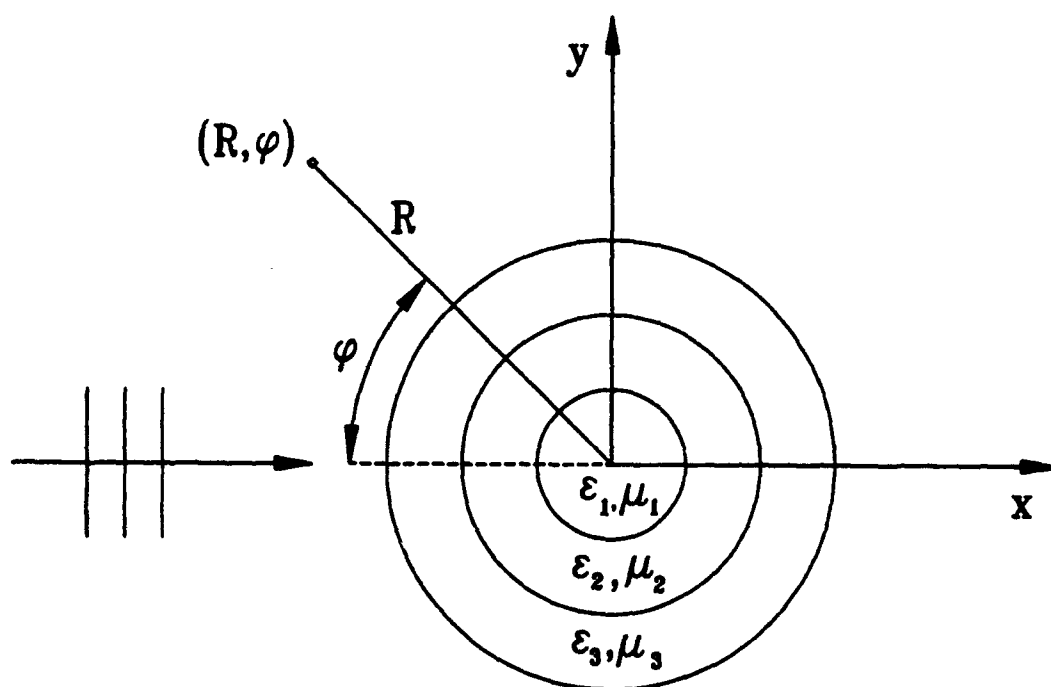


Figure 13: Geometry for infinite length cylinder analysis with normal plane wave incidence.

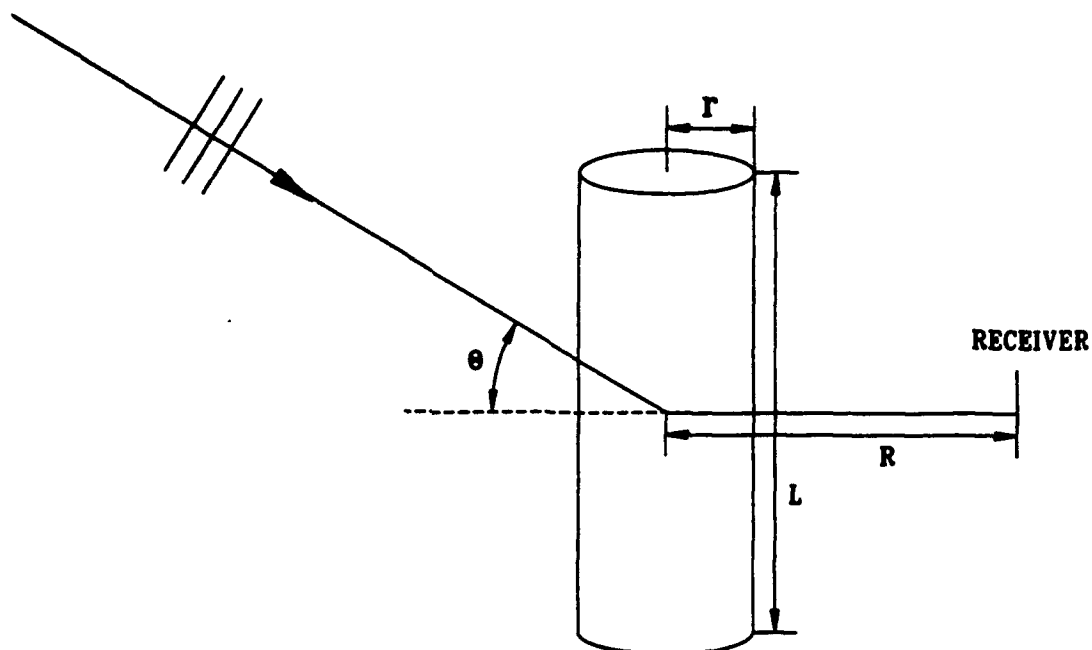


Figure 14: Geometry used for analysis of finite length cylinders with oblique plane wave incidence.

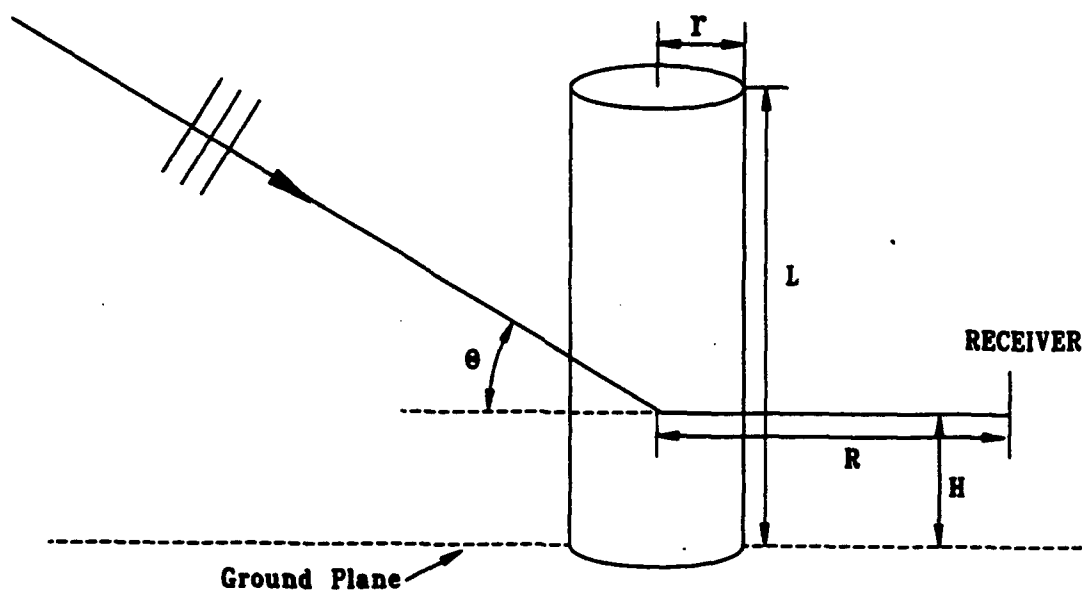


Figure 15: Geometry used for analysis of finite length cylinders with oblique plane wave incidence above an infinite ground plane to simulate the ground.

3 Analysis and Results

For the analysis, different combinations of material properties and thicknesses for the cylinder are used to find any trends in the near-zone scattered field to cylinder model parameters. The dielectric constants ϵ_r and dimensions of the dielectric cylinder used are from Tables 1 and 2. Chapter 4 shows that the single layer dielectric model is sufficient to match with measurements for the backscatter RCS. However, since the fields in the vicinity of the cylinder are now of interest, both the single layer models and the multilayer model are used. For the two-layer multilayer model shown in Table 2, a third layer is also added to simulate the actual geometry of a tree more accurately as discussed in Chapter 3. The fields near a dielectric cylinder using single layer, two-layer, and three-layer models are all analyzed.

3.1 Results for Cylinders of Infinite Length

Most of the analysis consists of dielectric cylinders that are 0.15 meters in radius and at a frequency of 0.75GHz. The dielectric constants and thicknesses are varied for each of the two or three layers of the cylinder. The main trends in the analysis are shown in the next few figures. The results for a typical three-layer cylinder model for both TM and TE polarizations at radial distances of 4, 10, and 30 meters are shown in Figures 16, 17, and 18, respectively. This three-layer model has an inner layer of thickness 0.07m and $\epsilon_r=15-j7$, a second layer of thickness 0.07m and $\epsilon_r=7-j3$, and an outer layer of thickness 0.01m and $\epsilon_r=4-j1$. These figures show the trends in the total field produced by a typical tree at various radial distances. It is worth noting that at even 30 meters (75 wavelengths) the total field still shows a variation directly behind the cylinder of about ± 1 dB from the free space value. This result is typical for the various combinations of dielectric constants and thicknesses used in the cylinder models.

For comparison, results for a two-layer cylinder model at $R=4$ meters are shown in Figure 19. This two-layer model has an inner layer of thickness 0.13m and $\epsilon_r=8-j1$,

and an outer layer of thickness 0.02m and $\epsilon_r = 4 - j0$. The field plot is very similar to the previous case for the three-layer model but differs slightly in the forward scatter region. This two-layer geometry also shows a similar fluctuation in the field at 30 meters as the previous three-layer example. For further comparison, the dielectric constants that are used to model the RCS of the logs in Chapter 4 are also used in the near field analysis. Two single layer cylinder geometries are analyzed each with a different dielectric constant. A field plot of the first single layer model at $R=4$ meters is shown in Figure 20 for a dielectric constant of $\epsilon_r = 12.4 - j4.9$. The field pattern at $R=4$ meters for another single layer model with dielectric constant $\epsilon_r = 24 - j8$ is shown in Figure 21. The similarities between the single, two, and three layer cylinder models illustrate the trends observed in the field patterns of the various cylinder geometries analyzed. All the geometries examined showed approximately the same total field patterns as these two cases. This invariance in the field patterns to the constituent layers for the various cases shows that the field is relatively insensitive to the cylinder layer thickness and dielectric constants used in modeling the tree trunk.

To further illustrate the behaviour of the fields with distance, a rectangular grid of field points in the forward scatter region is calculated. Figures 22 and 23 show the field for a grid of points behind the cylinder for TM and TE polarizations, respectively. The cylinder is comprised of three-layers with an inner thickness of 0.08 meters and $\epsilon_r = 15 - j7$, a second layer with a thickness of 0.05 meters and $\epsilon_r = 6 - j3$, and an outer layer with a thickness of 0.02 meters and $\epsilon_r = 4 - j1$. For comparison, the fields for another geometry are plotted in Figures 24 and 25. This cylinder has an inner layer thickness of 0.08 meters and $\epsilon_r = 6 - j3$, a second layer with a thickness of 0.05 meters and $\epsilon_r = 15 - j7$, and an outer layer of thickness 0.02 meters and $\epsilon_r = 4 - j1$. The field for a single layer cylinder with a dielectric constant of $\epsilon_r = 12.4 - j4.9$ is shown in Figures 26 and 27 for TM and TE polarizations, respectively. Another single layer cylinder with a dielectric constant of $\epsilon_r = 24 - j8$ is plotted in Figures 28 and 29, respectively. The main difference in the plots is mainly in the depth of

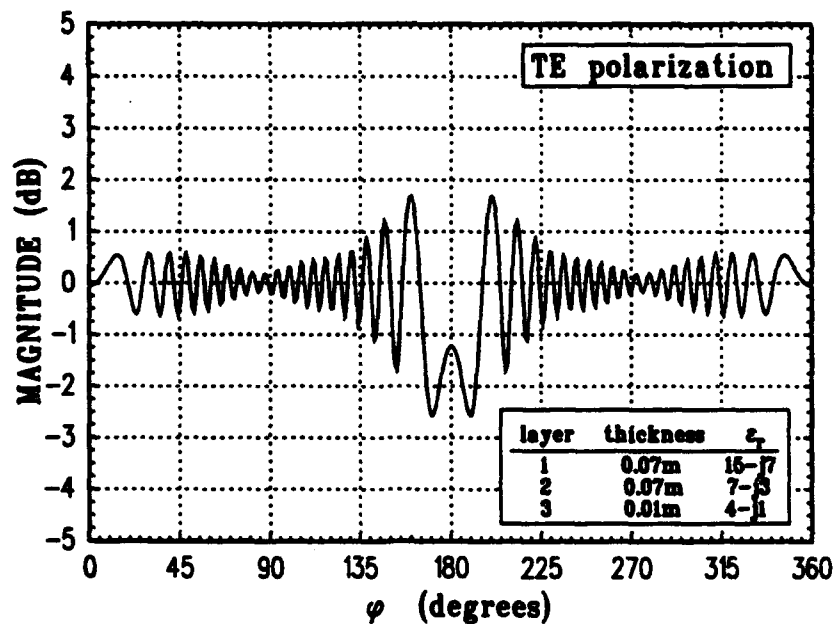
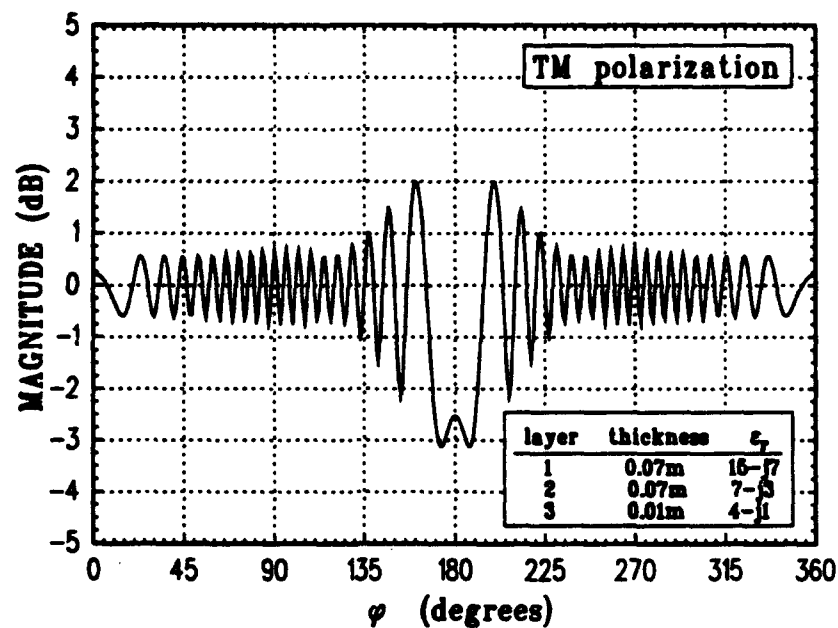


Figure 16: Total E-field magnitude in dB relative to the incident field for a three-layer cylinder at a distance of 4 meters at 0.75GHz.

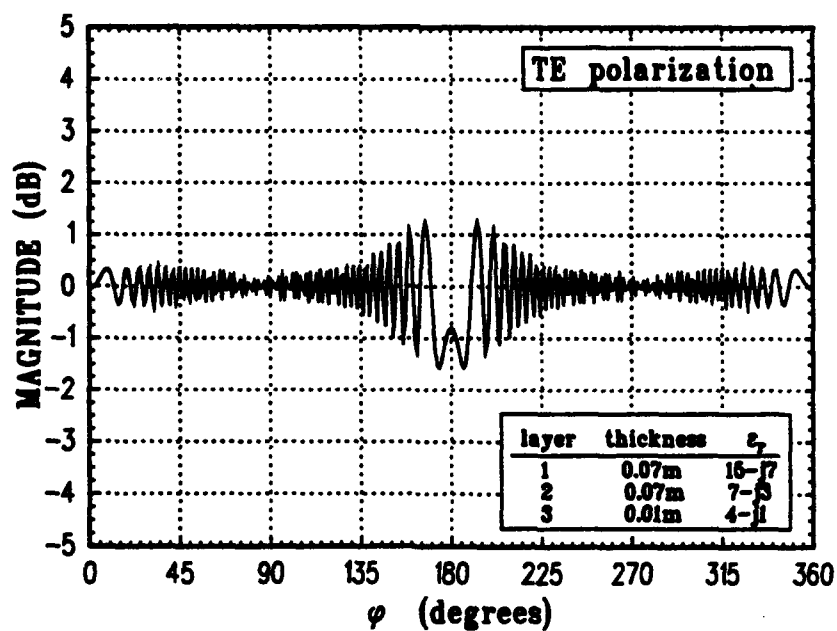
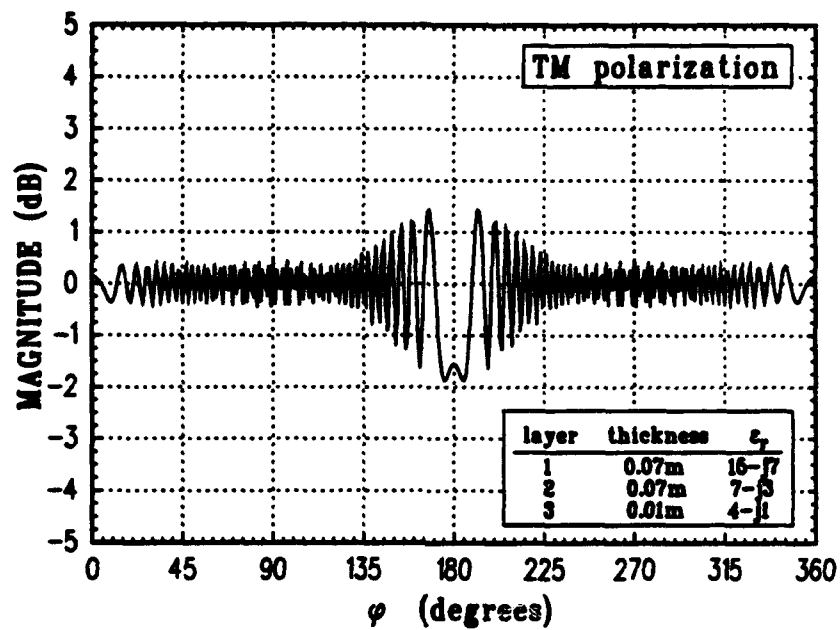


Figure 17: Total E-field magnitude in dB relative to the incident field for a three-layer cylinder at a distance of 10 meters at 0.75GHz.

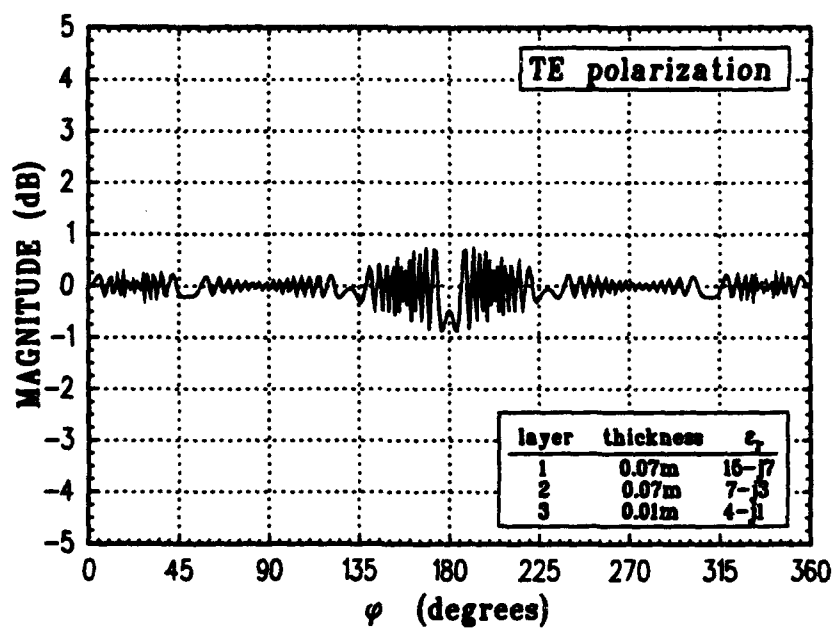
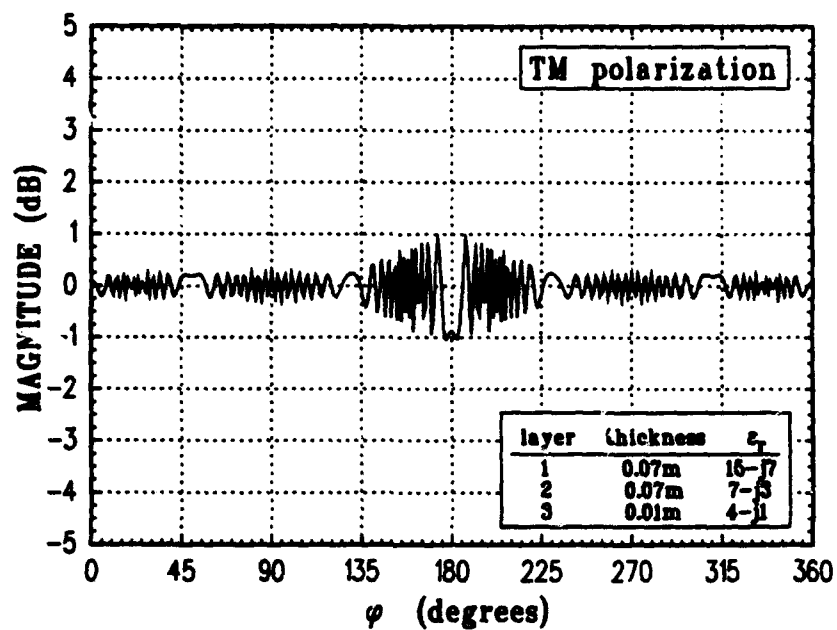


Figure 18: Total E-field magnitude in dB relative to the incident field for a three-layer cylinder at a distance of 30 meters at 0.75GHz.

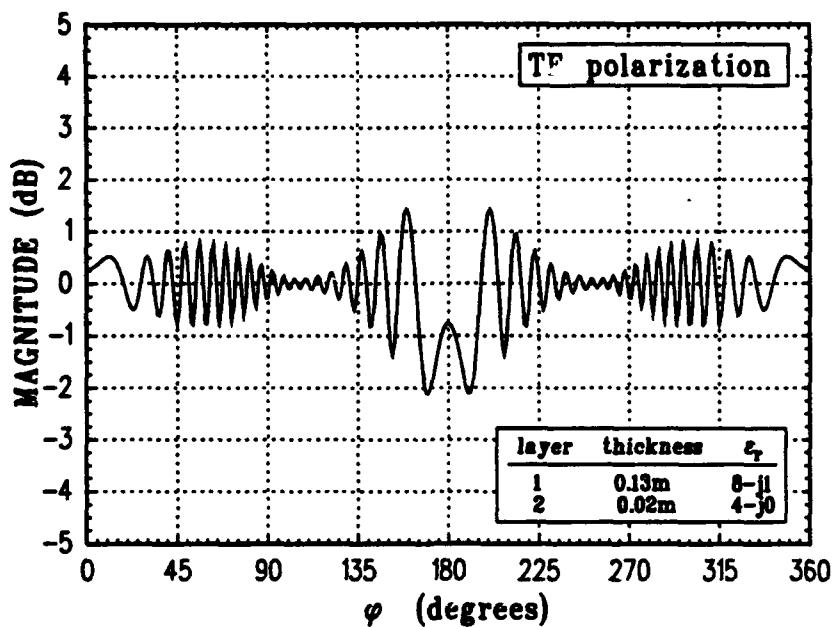
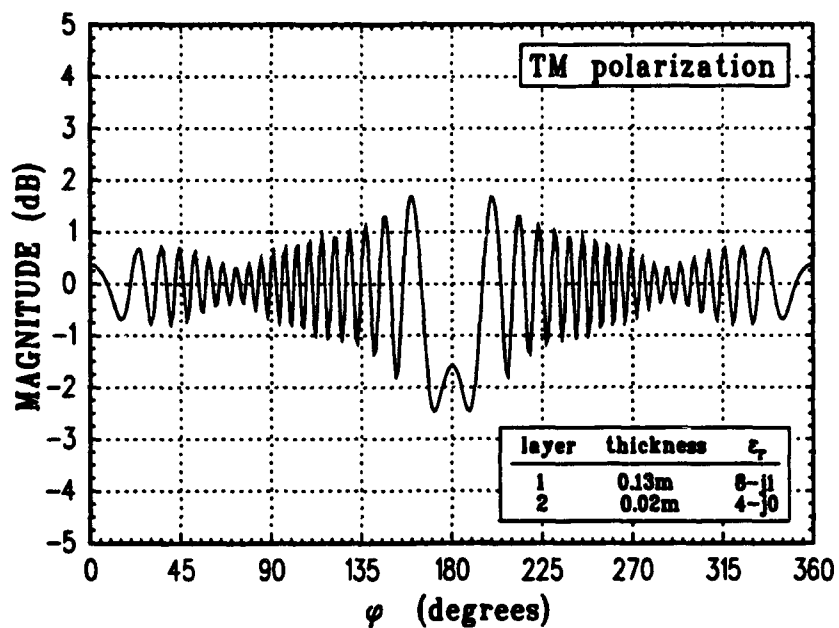


Figure 19: Total E-field magnitude in dB relative to the incident field for a two-layer cylinder at a distance of 4 meters at 0.75GHz.

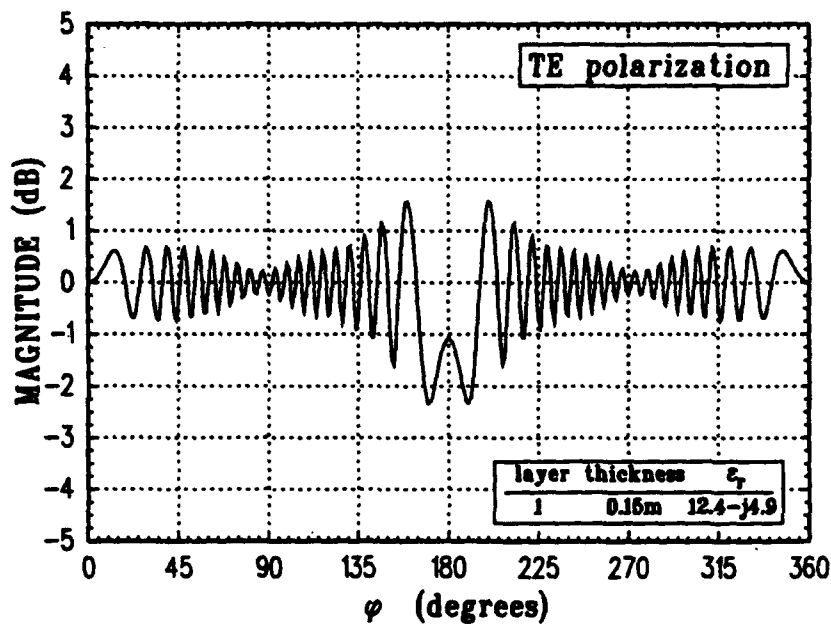
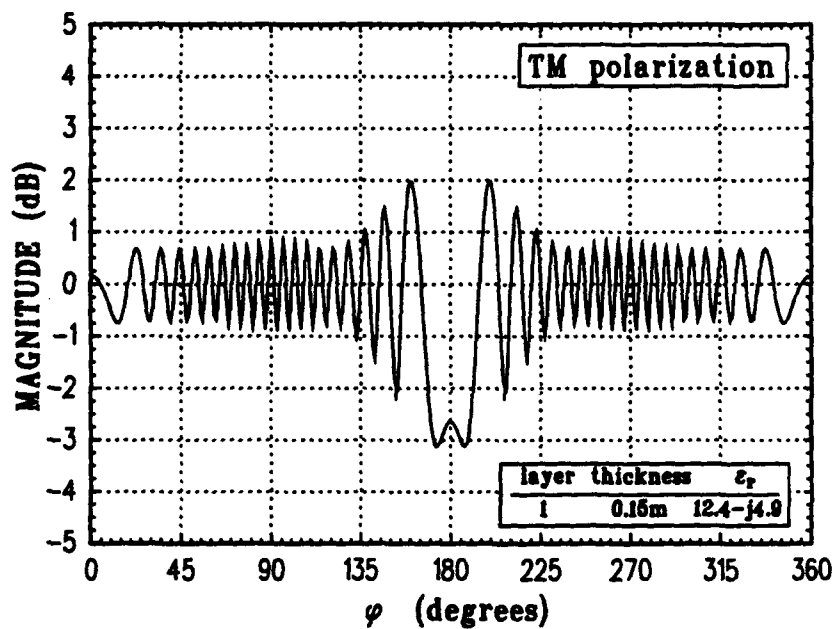


Figure 20: Total E-field magnitude in dB relative to the incident field for a single layer cylinder with $\epsilon_r=12.4-j4.9$ at a distance of 4 meters at 0.75GHz.

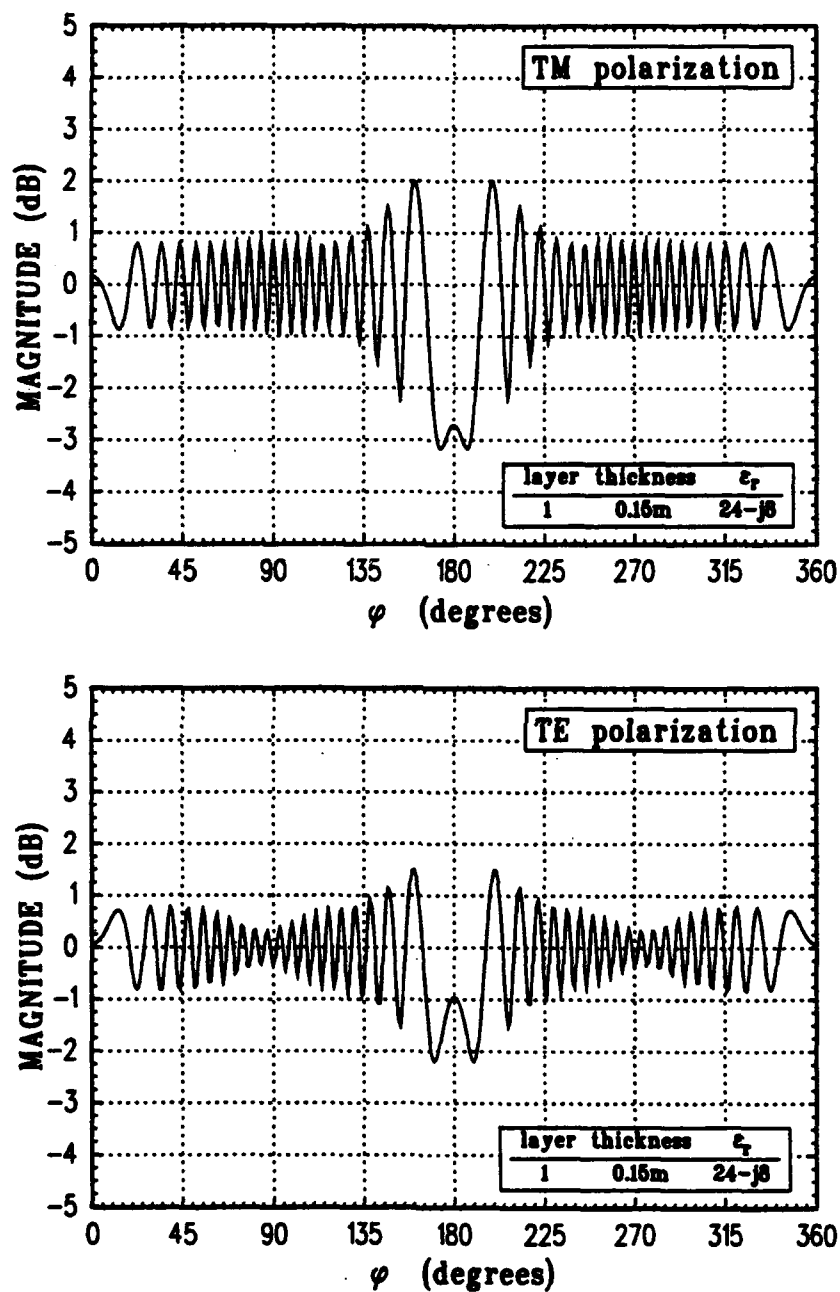


Figure 21: Total E-field magnitude in dB relative to the incident field for a single layer cylinder with $\epsilon_r=24-j8$ at a distance of 4 meters at 0.75GHz.

the scattered field near the cylinder. The similarity of the plots for their respective polarizations again shows the same relative insensitivity in near field patterns to the dielectric constant and the layer thickness as was observed earlier. And since the fields are relatively insensitive to the number of layers used, modeling the trunk with a single dielectric layer is also valid for the near-zone scattered field as is found for the far-zone RCS.

4 Results For Cylinders Of Finite Length

The previous section describes the results for infinite length dielectric cylinders under normal incidence. The infinite length of the cylinder used to model the tree trunk isn't very faithful to the true finite length of a tree trunk. For this reason, the scattered field of finite length dielectric cylinder at oblique incidence is also of interest. However, no solution is readily available for the near field of a finite length multilayered dielectric cylinders at oblique incidence. Therefore, it is desirable to find a range over which the exact solution for normal incidence of infinite length cylinders can be applied to the case of finite length cylinders with oblique incidence. To accomplish this, a UTD solution for oblique incidence is used for comparison at various inclination angles, θ (see Figure 14), with the exact, normal incidence solution. However, the only accurate UTD solution for the deep shadow region presently available is for PEC cylinders. The exact solution for infinite length cylinders at normal incidence is used to calculate the field at various distances R from a PEC cylinder. The UTD solution is then used to calculate the field for various incidence angles θ at the same distances.

For the geometries analyzed, a cylinder length of $L=10$ meters and a radius of $r=0.15$ meters as shown in Figure 14 are used. The two solutions match very closely for the case of normal incidence ($\theta=0$ degrees) for the finite length cylinder. This shows that the diffraction from the cylinder ends is relatively insignificant for the height and radius analyzed. Comparison plots between the exact solution and the

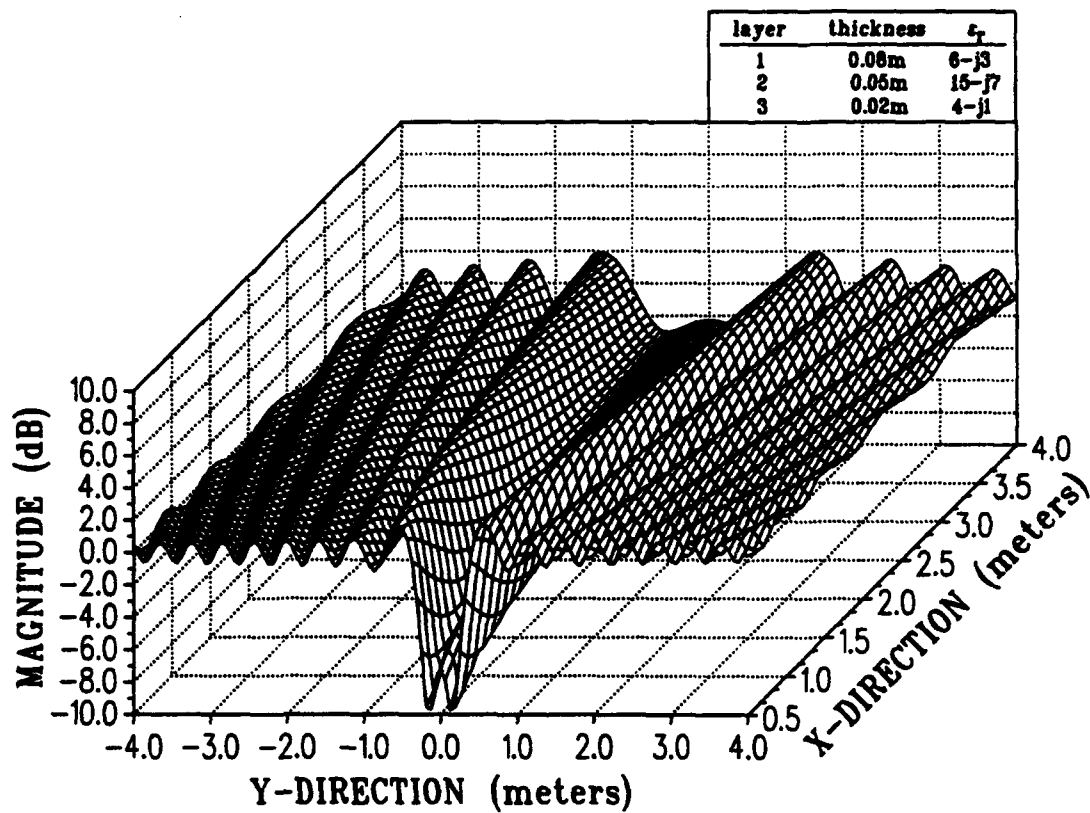


Figure 22: Total E-field magnitude in dB relative to the incident field for a three-layer cylinder at 0.75GHz for TM polarization.

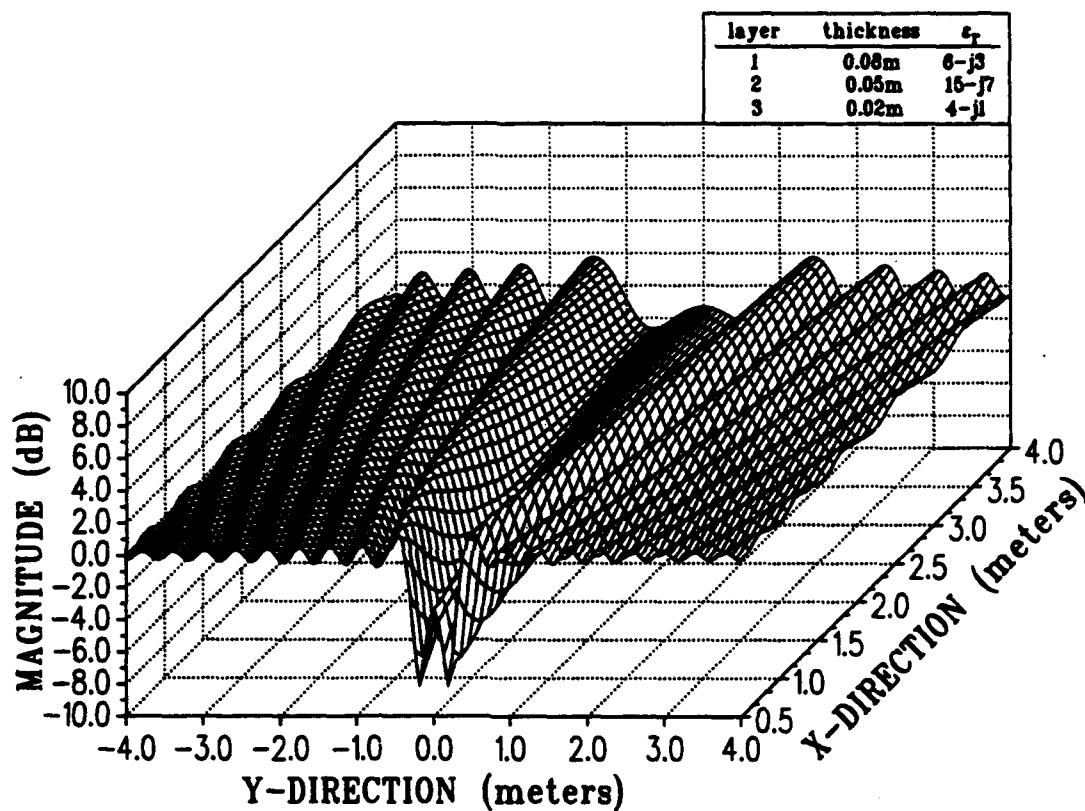


Figure 23: Total E-field magnitude in dB relative to the incident field for a three-layer cylinder at 0.75GHz for TE polarization.

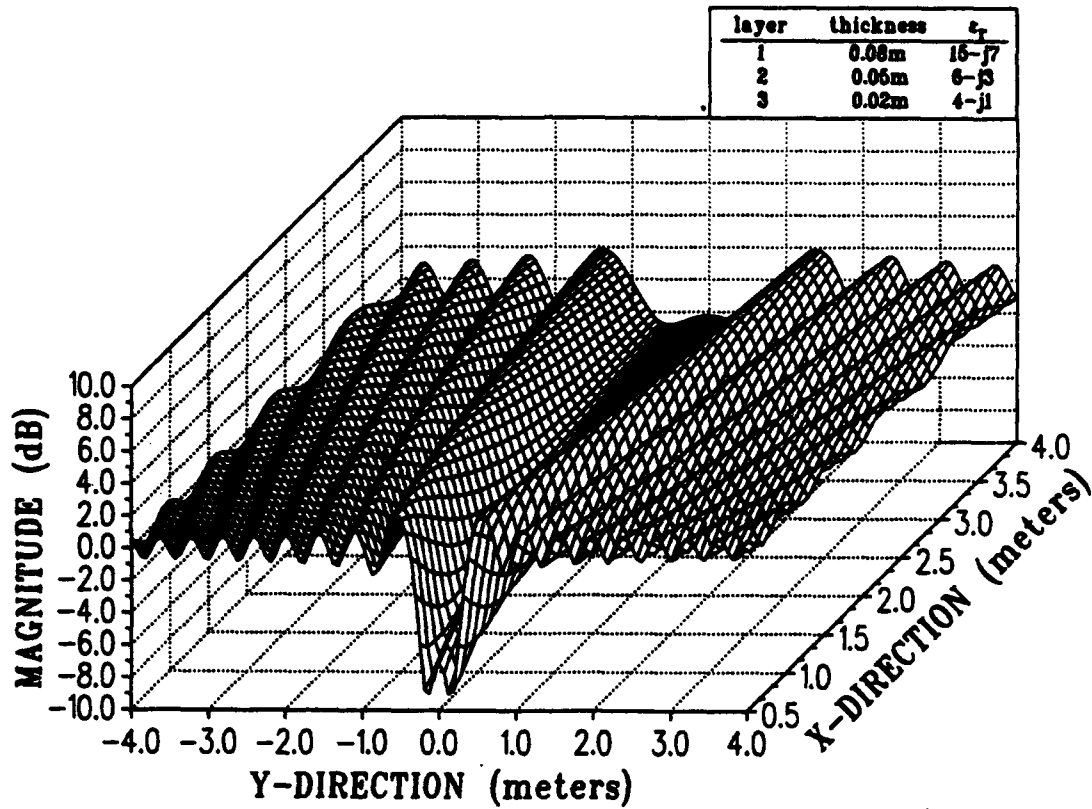


Figure 24: Total E-field magnitude in dB relative to the incident field for a three-layer cylinder at 0.75GHz for TM polarization.

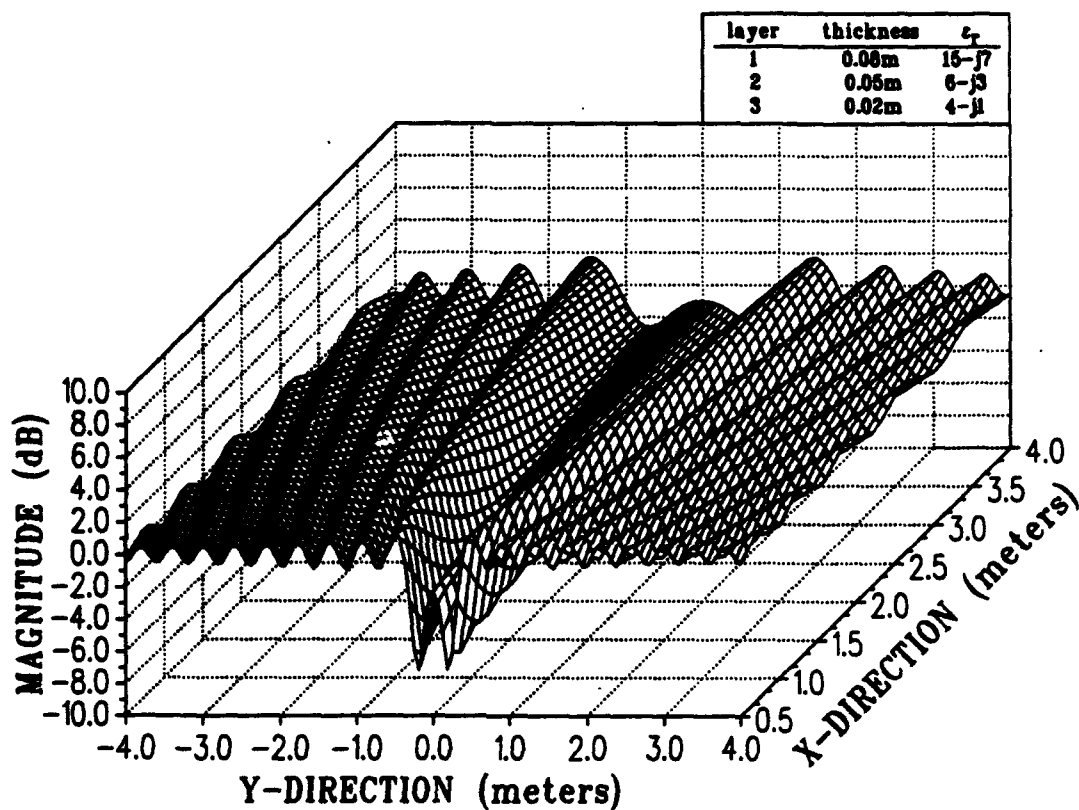


Figure 25: Total E-field magnitude in dB relative to the incident field for a three-layer cylinder at 0.75GHz for TE polarization.

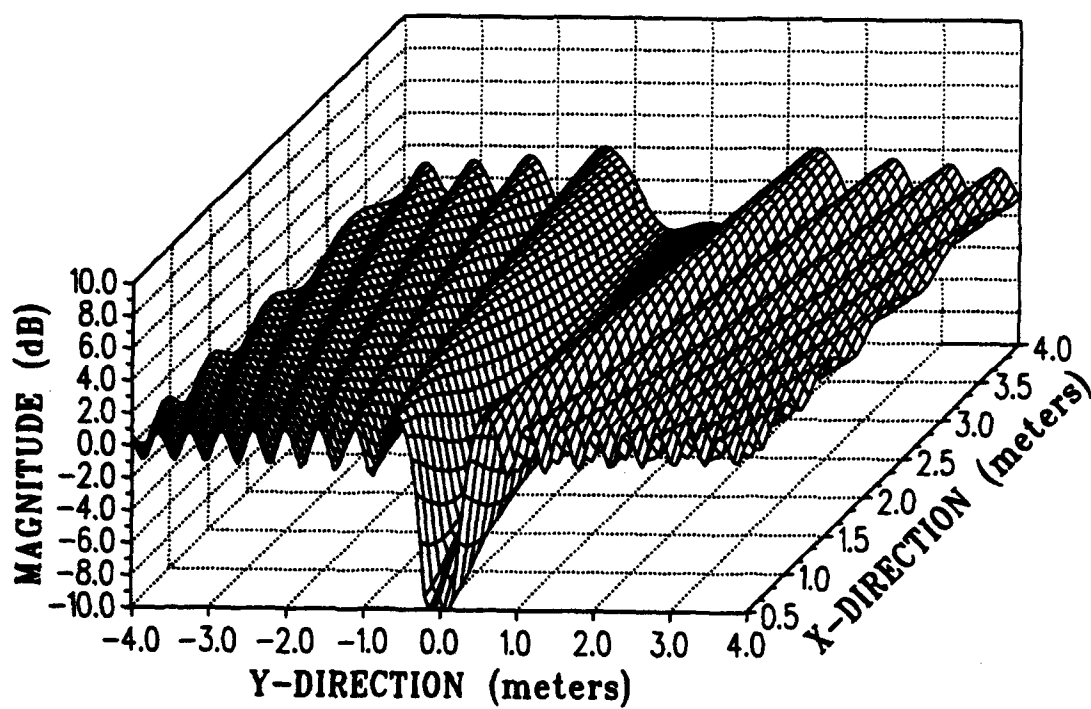


Figure 26: Total E-field magnitude in dB relative to the incident field for a single layer cylinder with $\epsilon_r = 12.4 - j4.9$ at 0.75GHz for TM polarization.

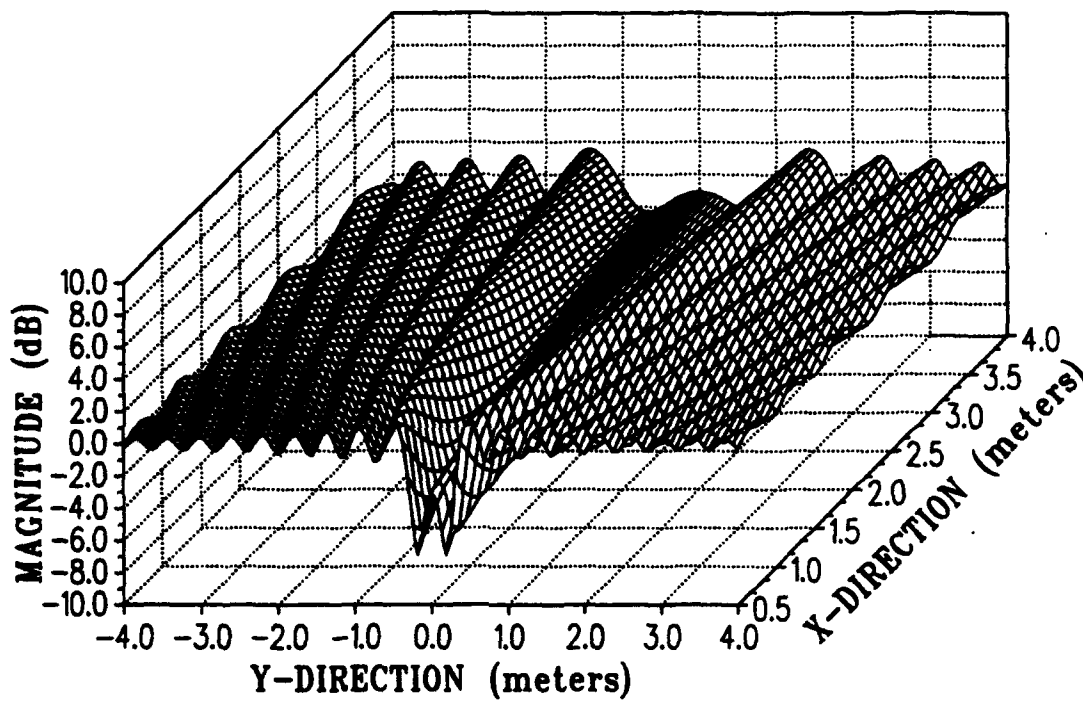


Figure 27: Total E-field magnitude in dB relative to the incident field for a single layer cylinder with $\epsilon_r = 12.4 - j4.9$ at 0.75GHz for TE polarization.

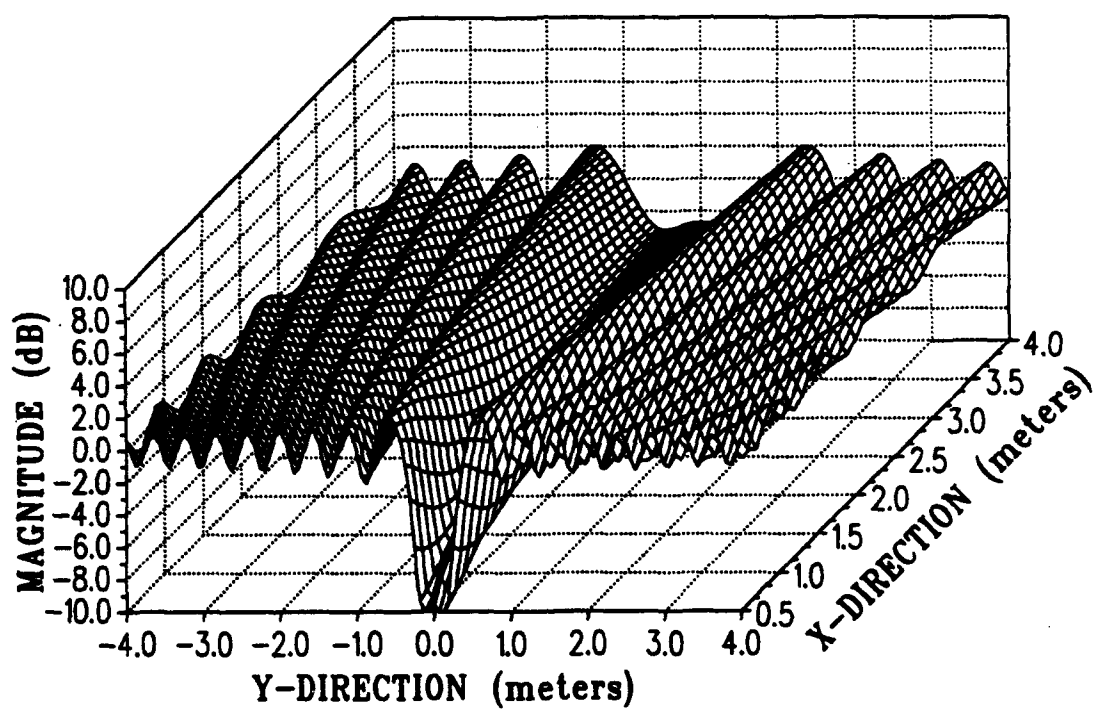


Figure 28: Total E-field magnitude in dB relative to the incident field for a single layer cylinder with $\epsilon_r = 24 - j8$ at 0.75GHz for TM polarization.

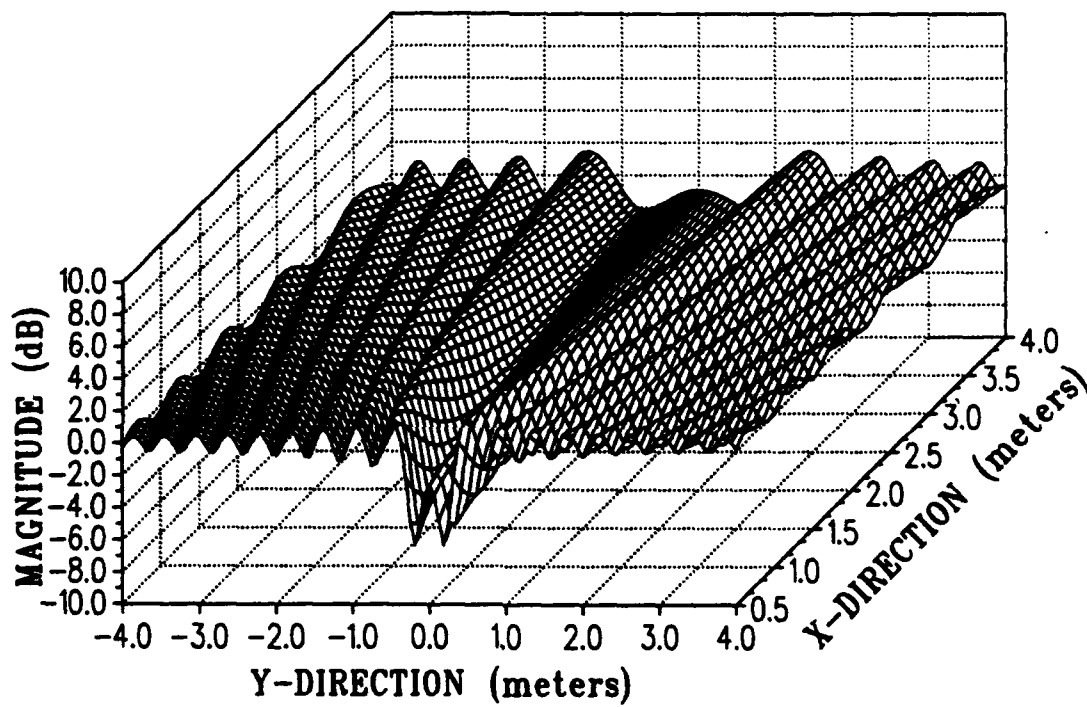


Figure 29: Total E-field magnitude in dB relative to the incident field for a single layer cylinder with $\epsilon_r = 24 - j8$ at 0.75GHz for TE polarization.

UTD solution are overlayed in Figures 30 and 31 at a distance of 5 meters for 15 and 30 degree inclinations, respectively. The two solutions are also overlayed for a distance of 10 meters and an incident angle of 15 degrees in Figure 32. The overlayed plots show a very close similarity in their near field patterns except for a slight variance in the sidelobe spacing and a difference in the depth of the main null in the forward scatter region. These differences are relatively small and show that the normal solution can be used for oblique incidence up to 30 degrees depending on the accuracy required. However, the solution for normal incidence is no longer applicable to the oblique incidence geometry as the incidence angle θ increases and/or the radial distance R increases since then the direct ray dominates the near field pattern.

The case for the cylinder above an infinite ground plane is analyzed next using the same NEC-BSC code as the above UTD solution. The case for a cylinder radius of 0.15m, length of $L=10$ meters, and height of $H=2$ meters for various inclination angles as shown in Figure 15 are analyzed. The near field patterns for TM and TE polarizations at a distance of 5 meters for incidence angles of 15 and 30 degrees are overlayed with the exact solution for normal incidence in Figures 33 and 34, respectively. The imaged UTD oblique incidence solution and the normal incidence exact solution agree very closely in the same regions and disagree in the same regions as the above exact and UTD solution without the ground plane.

5 Summary

The scattered fields in the vicinity of a cylinder used to model a tree trunk are analyzed. It was shown that the scattered fields for a infinite length dielectric cylinder are relatively insensitive to the dielectric constants and layering of the cylinder and that a single layer model is also valid for the near-zone scattering. Also, the blockage in the forward scatter caused by the tree trunk is shown to be large. The blockage is approximately 5dB directly behind the trunk and decreases to approximately 1dB at 30 meters from the trunk. The solution of the infinite length dielectric cylinder

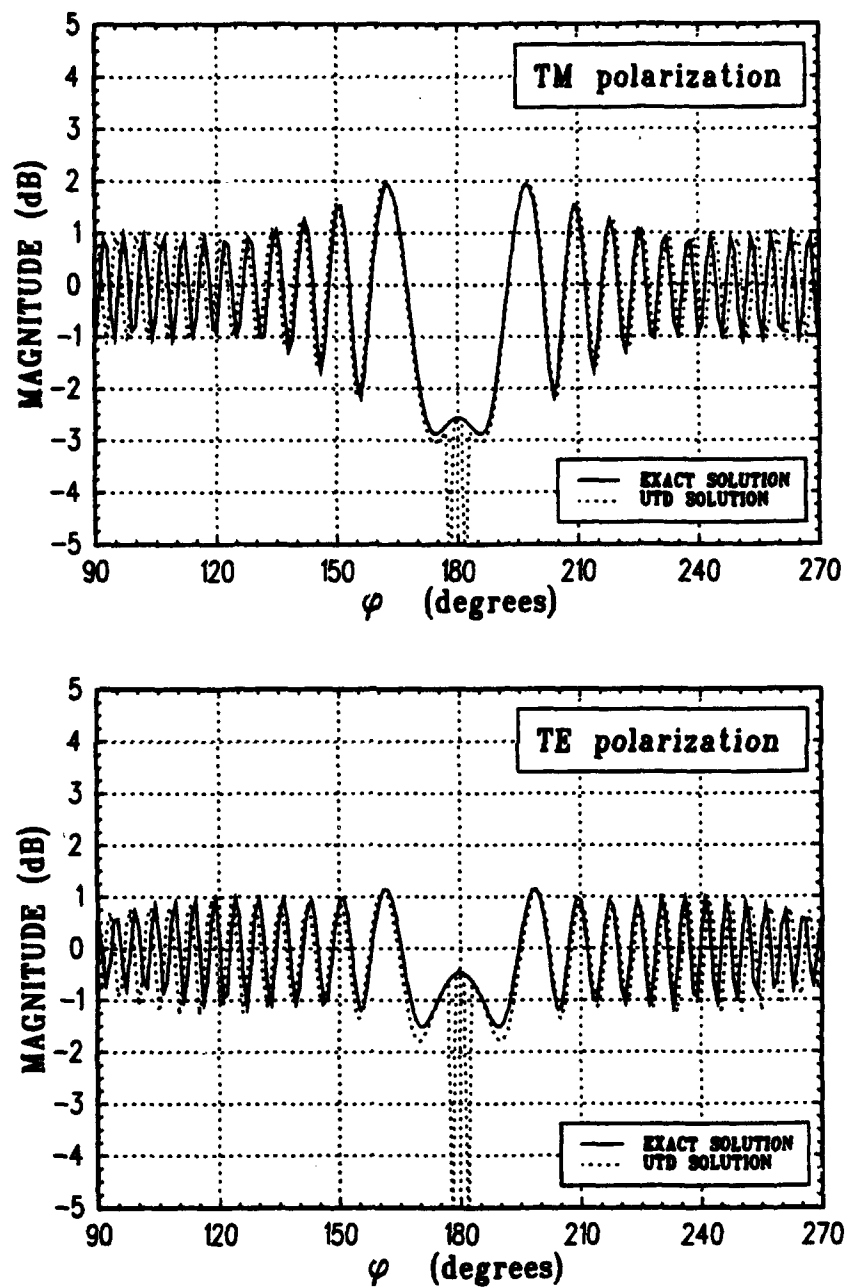


Figure 30: Comparison of total E-field magnitude in dB relative to the incident field for a P.E.C. cylinder for an exact solution at normal incidence and a UTD solution at 15 degrees incidence at a distance of 5 meters at 0.75GHz

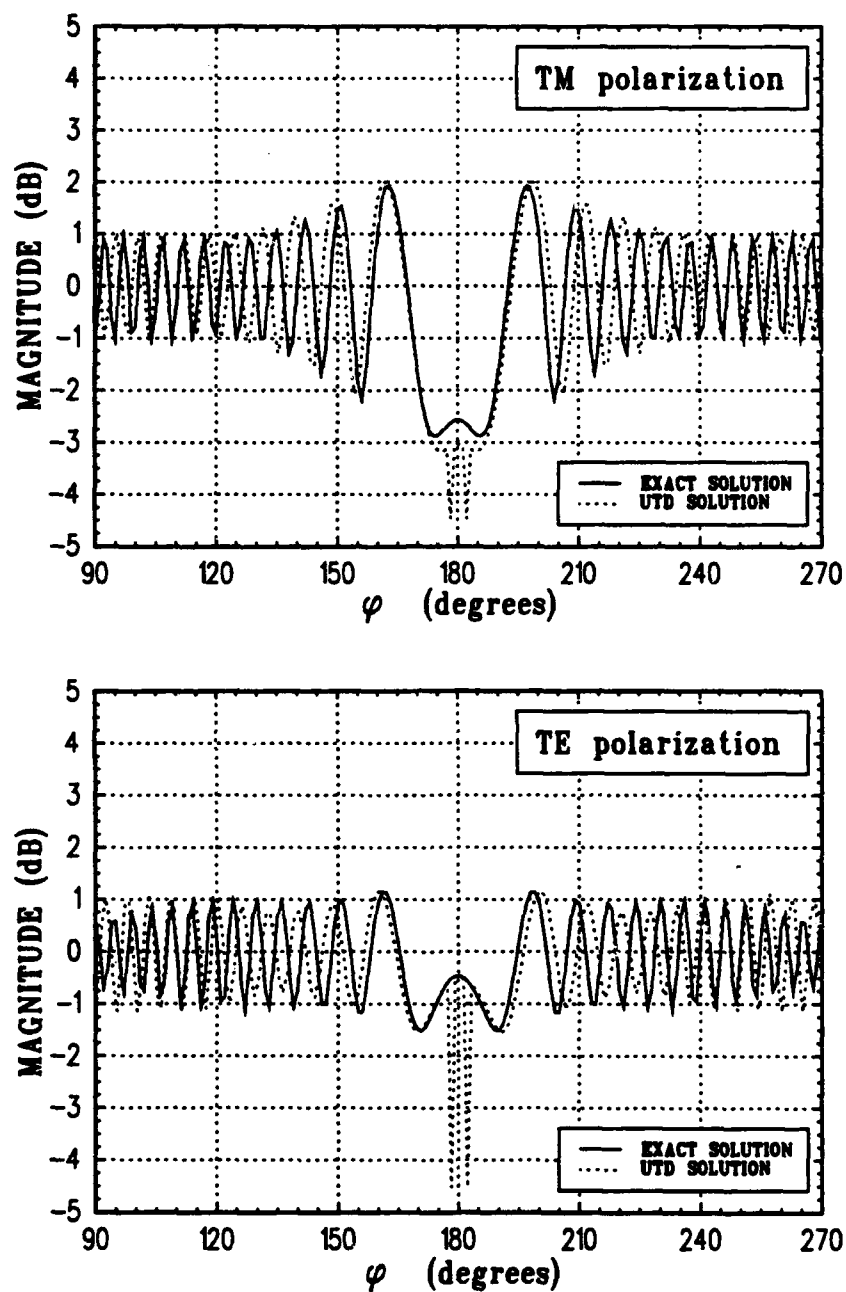


Figure 31: Comparison of total E-field magnitude in dB relative to the incident field for a P.E.C. cylinder for an exact solution at normal incidence and a UTD solution at 30 degrees incidence at a distance of 5 meters at 0.75GHz.

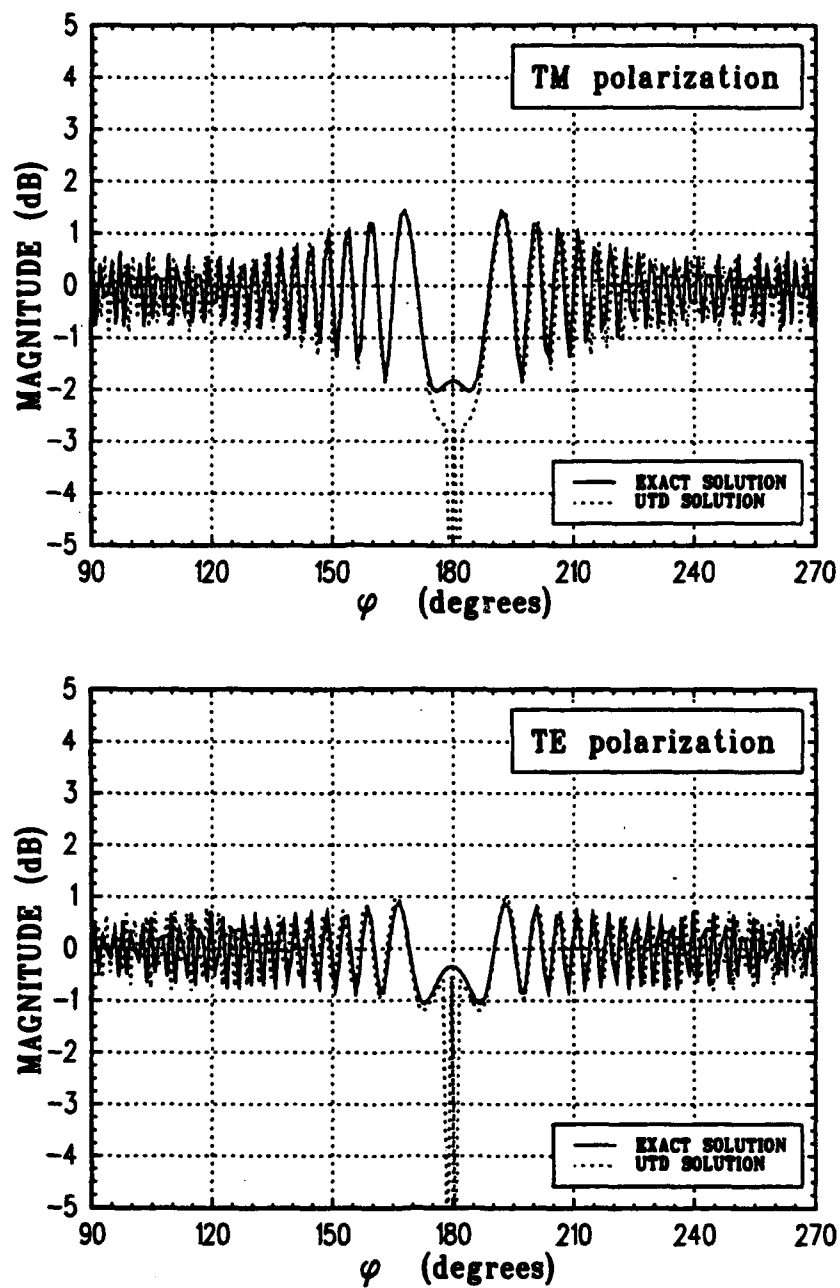


Figure 32: Comparison of total E-field magnitude in dB relative to the incident field for a P.E.C. cylinder for an exact solution at normal incidence and a UTD solution at 15 degrees incidence at a distance of 10 meters at 0.75GHz.

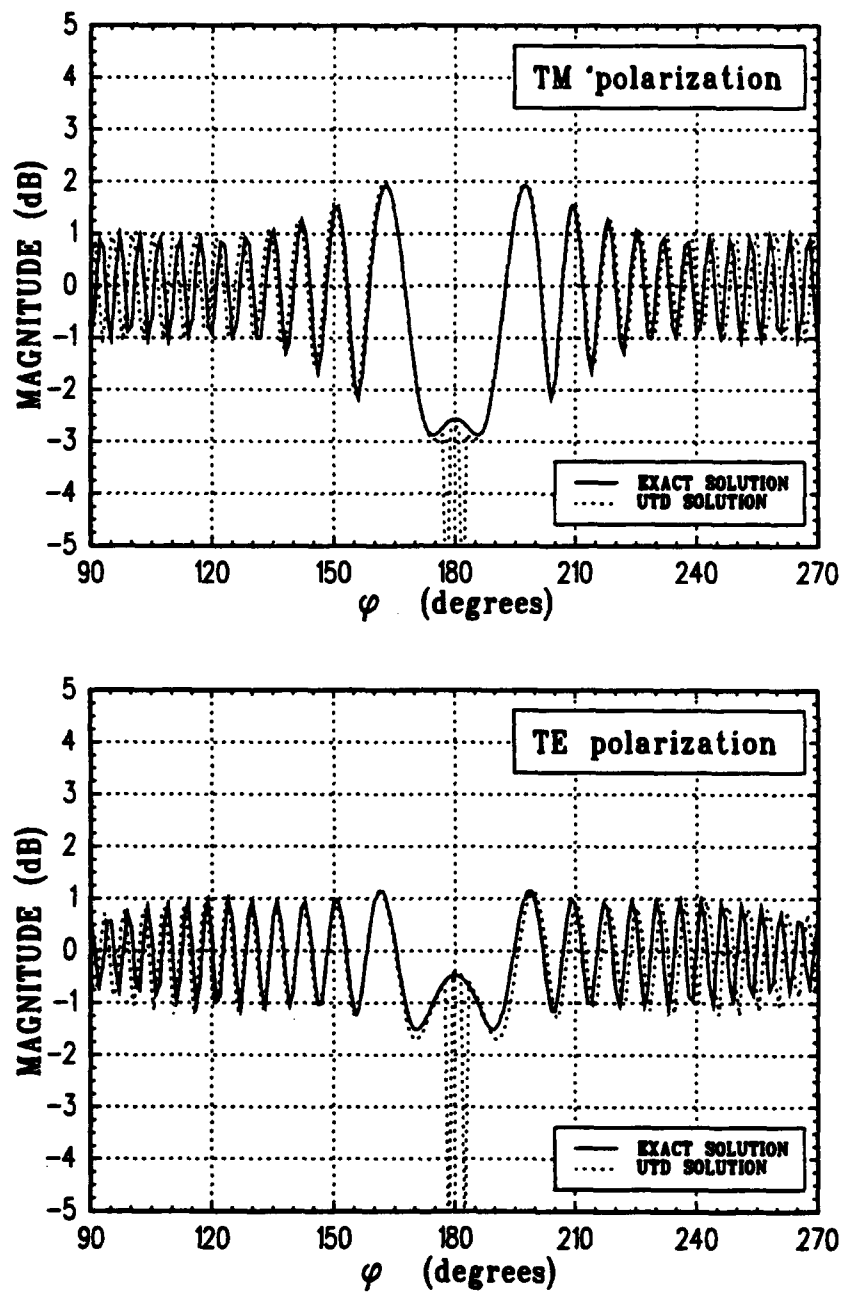


Figure 33: Comparison of total E-field magnitude in dB relative to the incident field for a P.E.C. cylinder for an exact solution at normal incidence and an imaged UTD solution at 15 degrees incidence at a distance of 5 meters at 0.75GHz.

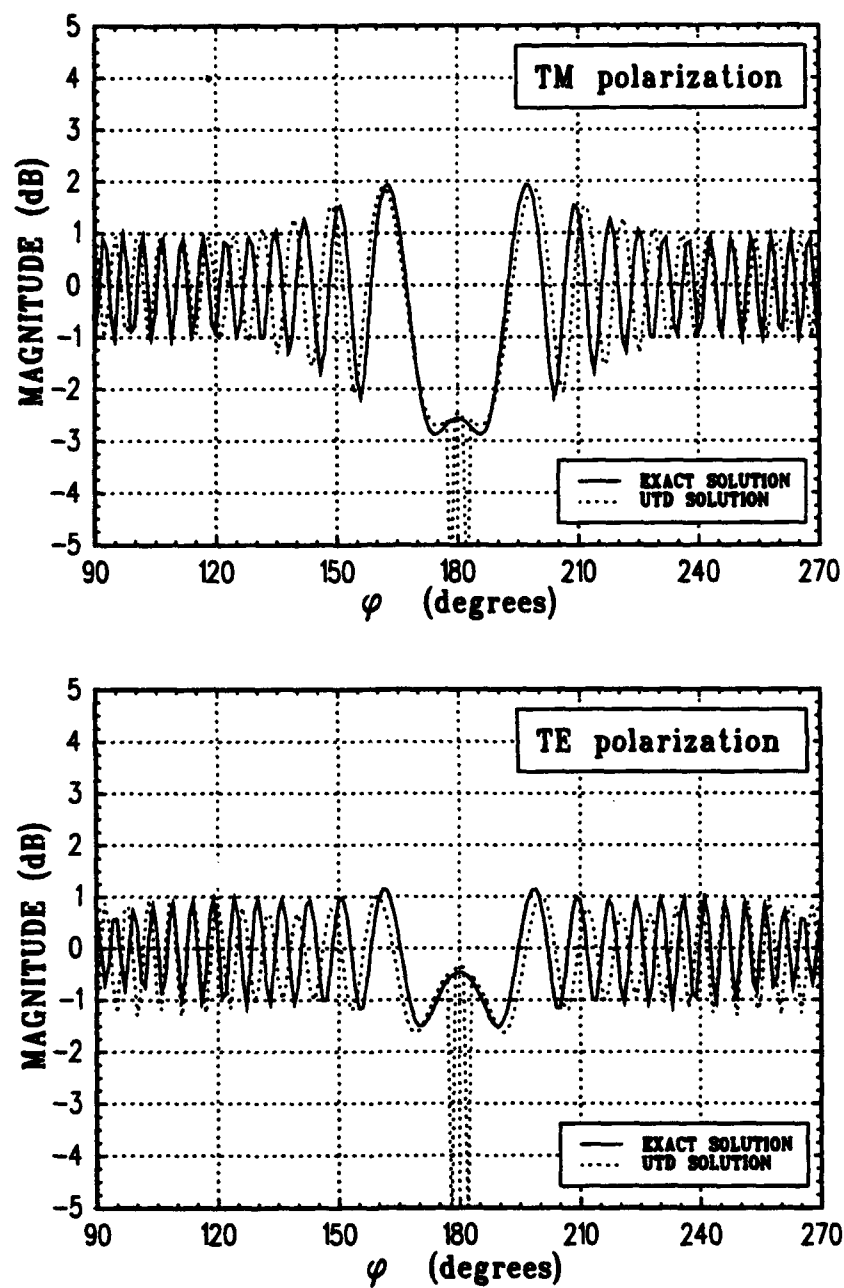


Figure 34: Comparison of total E-field magnitude in dB relative to the incident field for a P.E.C. cylinder for an exact solution at normal incidence and an imaged UTD solution at 30 degrees incidence at a distance of 5 meters at 0.75GHz.

is then shown to be applicable to a finite length dielectric cylinder as long as the incidence angle is less than 30 degrees and no direct ray between the source and receiver exists. Similar results are found for the finite length cylinder above a ground plane as for the case without the ground plane.

SECTION 6

Trunk-Ground Interactions

1 Introduction

The effect of the ground on the scattering by a tree trunk is examined. This builds on the results of Chapter 5 which examines the fields in the vicinity of infinite length cylinders and for finite length cylinders above a perfect ground plane. The analysis in Chapter 5 uses an exact eigenfunction solution and a UTD analysis with the NEC-BSC code. In this chapter, the scattering from only the interaction between the tree trunk and the ground is examined. The scattering from branches is discussed separately in Chapter 7 to simplify the analysis. The Geometric Theory of Diffraction (GTD) is used to find the scattering of a finite length dielectric cylinder representing the trunk protruding from an infinite dielectric half-space representing the ground. The solution is then verified against the PEC top-hat solution formulated by N. Akhter [25] and is also verified using image theory for a dielectric cylinder above a PEC ground plane. The GTD solution is then used to analyze the scattering from the trunk-ground interactions for various trunk and ground parameters. In the analysis, the ground is modeled as described in Section 2 and the wood is modeled based on the results of Chapters 4 and 5.

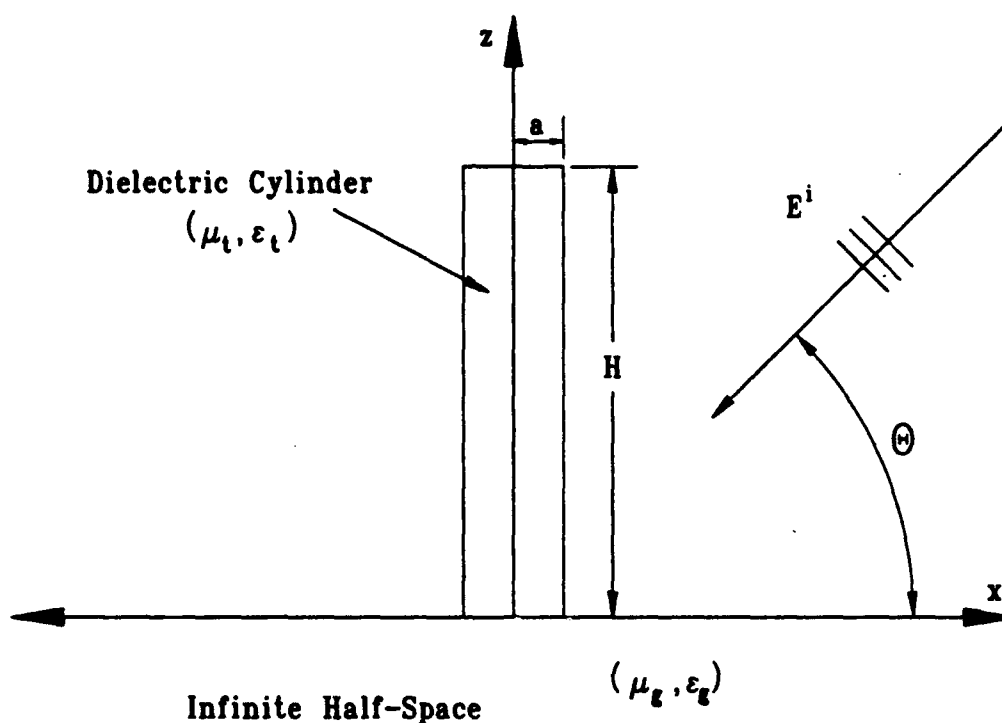


Figure 35: Geometry used to model trunk-ground interactions.

2 Modeling of Geometry

In Section 2, only the larger branches and the trunk need to be accounted for in modeling the tree for the frequencies between 0.3–1.3GHz. In Chapters 4, 5, and 7 it is valid to model the scattering from a log (wood) as a dielectric cylinder. The same method is used in this analysis. The ground is now modeled as a dielectric half-space as mentioned in Section 4 which is more realistic than modeling it as a PEC as is done in Chapter 5. This modeling of the geometry will enable a more accurate analysis of the RCS of a tree by including trunk-ground interactions (TGI). The resulting geometry is shown in Figure 35. The geometry consists of a finite length dielectric cylinder representing a tree trunk protruding from a dielectric half-space which simulates the ground. The cylinder can consist of either multiple concentric dielectric layers or as a single dielectric piece. The polarization defined as horizontal,

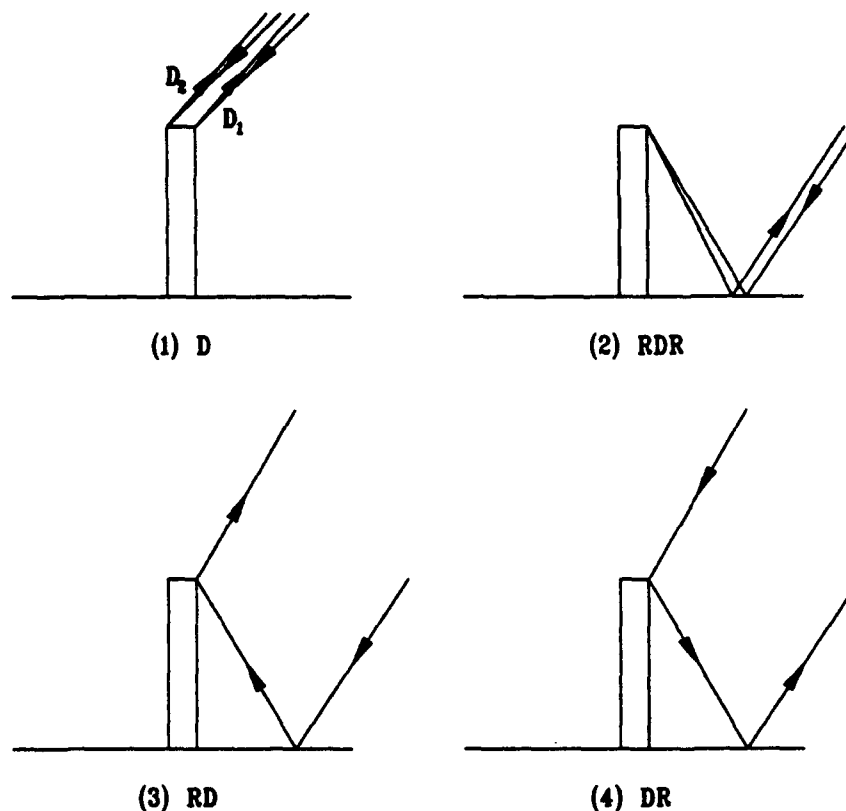


Figure 36: Diffraction interactions used in trunk-ground interaction modeling

with the electric field normal to the x - z plane, and vertical, with the electric field parallel to the x - z plane.

The modified Geometrical Theory of Diffraction for dielectric materials is then used to calculate the scattering from this geometry. Due to rotational symmetry, the backscattered field needs only to be calculated in the plane containing the axis of the cylinder. The only rays that need to be considered to find the backscattered field are shown in Figure 36.

Diffraction from the cylinder-ground junction is not considered in this analysis. This is because when the cylinder and base are at right angles and are of the same material, the scattering from this junction will be zero. When the cylinder and base are of two different materials, it is felt that the scattering from this interface will be small when compared to the other scattering mechanisms. Furthermore, an

appropriate solution to the scattering from this interface is not presently available. Therefore without significant impact on the calculation of the backscattered field, this contribution can be ignored.

The remaining terms in the GTD solution can readily be calculated using Equations (2) and (12). Accordingly, for the single diffraction D_1 terms, the incident and reflected angles referred to the top of the cylinder are given by:

$$\begin{aligned}\Phi' &= \pi - \theta \\ \Phi &= \pi - \theta - \epsilon.\end{aligned}\quad (25)$$

Where a small bistatic angle ϵ is subtracted from the diffracted ray to avoid computational errors when the diffracted ray lies along the incident ray path. The phase length of ray D_1 referenced to the center of the cylinder base is:

$$\rho = H \sin \theta + a \cos \theta. \quad (26)$$

The argument of the Chiang transition function U is:

$$U = 2ka \cos \theta. \quad (27)$$

The quantity ρ^d given by Equation (5) is:

$$\rho^d = \frac{a}{2 \cos \theta}. \quad (28)$$

Combining Equations (25), (26), (27), and (28) with Equations (2) and (12) yields the diffracted field for location 1 given by:

$$\begin{aligned}U^{D_1} = U_{s,h}^i \frac{-e^{-j\pi/4}}{3\sqrt{2\pi k}} \left\{ \left[\cot \left(\frac{\pi - 2\theta - \epsilon}{3} \right) + \cot \left(\frac{\pi + 2\theta + \epsilon}{3} \right) \right] + \right. \\ \left. \left[R_o^{s,h} \cot \left(\frac{3\pi - 2\theta - \epsilon}{3} \right) + R_n^{s,h} \cot \left(\frac{-\pi + 2\theta + \epsilon}{3} \right) \right] \right\} \\ e^{2jk(h \sin \theta + a \cos \theta)} \sqrt{\frac{a}{2 \cos \theta}} T_e(2ka \cos \theta)\end{aligned}\quad (29)$$

where:

$$U_{s,h}^i = \begin{cases} E, & \text{Horizontal polarization} \\ H, & \text{Vertical polarization.} \end{cases} \quad (30)$$

Likewise using the same procedure the diffracted field for location 2 is found to be:

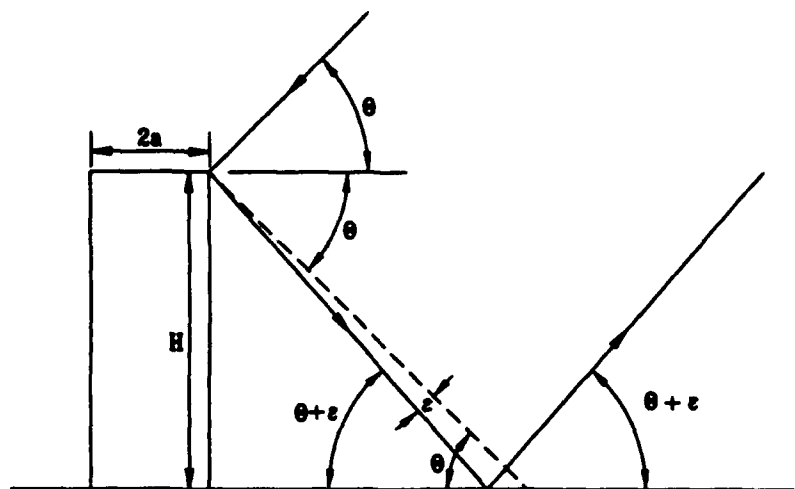
$$U^{D_2} = U_{s,h}^i \frac{-e^{-j\pi/4}}{3\sqrt{2\pi k}} \left\{ \left[\cot\left(\frac{\pi - \epsilon}{3}\right) + \cot\left(\frac{\pi + \epsilon}{3}\right) \right] + \left[R_o^{s,h} \cot\left(\frac{\pi + 2\theta - \epsilon}{3}\right) + R_n^{s,h} \cot\left(\frac{\pi - 2\theta - \epsilon}{3}\right) \right] \right\} e^{2jk(h \sin \theta + a \cos \theta)} e^{j\frac{\pi}{2}} \sqrt{\frac{a}{2 \cos \theta}} T_e(-2ka \cos \theta). \quad (31)$$

For the Reflected-Diffracted-Reflected (RDR) term, a similar procedure is used as before except the reflection coefficient from the ground R_g must be taken into account. The resulting diffracted field for the RDR term is:

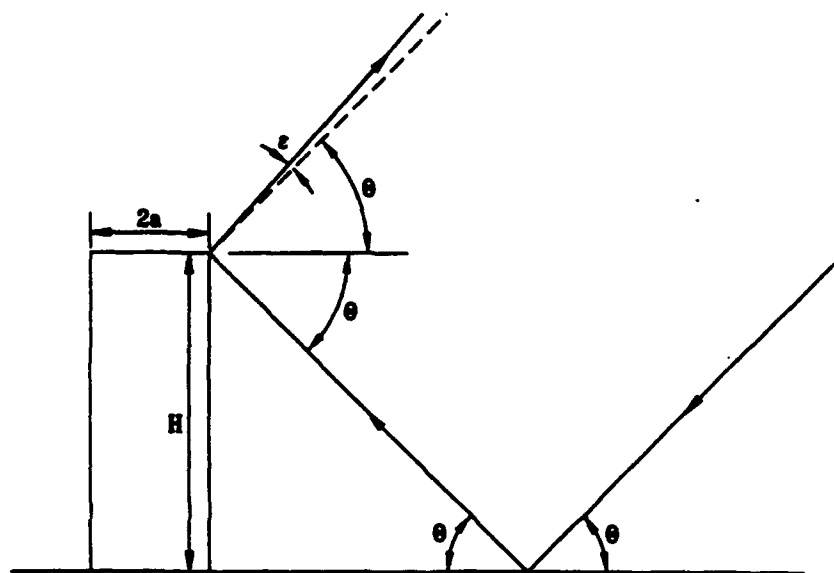
$$U^{RDR} = U_{s,h}^i \frac{-e^{-j\pi/4}}{3\sqrt{2\pi k}} (R_g^{s,h})^2 \left\{ \left[\cot\left(\frac{\pi + 2\theta - \epsilon}{3}\right) + \cot\left(\frac{\pi - 2\theta + \epsilon}{3}\right) \right] + \left[R_o^{s,h} \cot\left(\frac{3\pi + 2\theta - \epsilon}{3}\right) + R_n^{s,h} \cot\left(\frac{-\pi - 2\theta + \epsilon}{3}\right) \right] \right\} e^{\frac{-2jkh}{\sin \theta}} e^{2jk\frac{a+h}{\tan \theta} \cos \theta} \sqrt{\frac{a}{2 \cos \theta}} T_e(2ka \cos \theta). \quad (32)$$

The Diffracted-Reflected (DR) and Reflected-Diffracted (RD) terms can be calculated as follows. It has been shown that the DR and RD terms give the complete solution in the dihedral region if a small bistatic angle is taken between the incident and reflected ray paths for both the RD and DR terms [25]. The appropriate ray paths are shown in Figure 37. When the RD and DR terms are calculated this way and combined, the discontinuities in their solutions will cancel and provide the correct bounded result. This combination is done numerically by the computer and each diffraction term is presented independently. Using the geometry of Figure 37, the DR field is:

$$U^{DR} = U_{s,h}^i \frac{-e^{-j\pi/4}}{3\sqrt{2\pi k}} R_g^{s,h} \left\{ \left[\cot\left(\frac{\pi + \epsilon}{3}\right) + \cot\left(\frac{\pi - \epsilon}{3}\right) \right] + \left[R_o^{s,h} \cot\left(\frac{3\pi + \epsilon}{3}\right) + R_n^{s,h} \cot\left(\frac{-\pi - \epsilon}{3}\right) \right] \right\} e^{jk(a \cos(\theta + \epsilon) - h \sin(\theta + \epsilon))} e^{jk\sqrt{h^2 + a^2} \cos\left(\theta - \tan^{-1} \frac{h}{a}\right)} \sqrt{\frac{a}{2 \cos \theta}} T_e(2ka \cos \theta) \quad (33)$$



DR term



RD term

Figure 37: Calculation of RD and DR term using small bistatic angles between ray paths.

and the RD field is

$$U^{RD} = U_{s,h}^i \frac{-e^{-j\pi/4}}{3\sqrt{2\pi k}} R_g^{s,h} \left\{ \left[\cot\left(\frac{\pi - \epsilon}{3}\right) + \cot\left(\frac{\pi + \epsilon}{3}\right) \right] + \left[R_o^{s,h} \cot\left(\frac{3\pi - \epsilon}{3}\right) + R_n^{s,h} \cot\left(\frac{-\pi + \epsilon}{3}\right) \right] \right\} e^{jk(a \cos(\theta) - h \sin(\theta))} e^{jk\sqrt{h^2 + a^2} \cos\left(\theta + \epsilon - \tan^{-1} \frac{h}{a}\right)} \sqrt{\frac{a}{2 \cos \theta}} T_e(2ka \cos \theta). \quad (34)$$

It should be noted that the method to calculate the diffracted fields from the TGI geometry doesn't take the creeping wave component of the cylinder into account. The above diffracted fields are combined to calculate the scattered field for the trunk-ground interactions.

3 Verification of TGI Solution

The GTD solution for the trunk-ground interaction is verified in two ways. The RCS of a finite length dielectric cylinder is calculated using a modified exact eigenfunction expansion. Then the RCS of a dielectric cylinder of half the length as used in the exact solution above an infinite ground plane is analyzed using the TGI solution for θ approximately 0 degrees. The two values agree quite well for the various cases tried.

Unfortunately, no other solution for the dielectric trunk-ground interaction is available, but a solution is for a PEC top-hat. The top-hat has a finite radius PEC disk for a base instead of an infinite ground plane as in the TGI geometry. Therefore, to compare the two solutions, the equivalent top-hat geometry must be chosen carefully. First, the diffraction from the edge of the base of the top-hat must be eliminated since this edge doesn't exist for the TGI geometry. Second, the dimensions of the top-hat must be chosen such that only RD, DR, and RDR diffractions can occur from the top of the top-hat cylinder and not from the base edge. Once these modifications are done, the solutions can be verified for the PEC case. This is shown in Figure 38 for a top-hat of radius $a=0.2\text{m}$ and height $H=15\text{m}$.

Table 4: Diameters of trees (DBH) and the corresponding tree height h and effective tree height h_t of the cylinder used to model the tree.

DBH	tree height (h)	effective tree height (h_t)
12" (0.3048m)	17.4m	14.8m
14" (0.3556m)	20.4m	17m
16" (0.4064m)	23.3m	20m

The base radius of the top-hat is taken as 430 meters to eliminate the RD, DR, and RDR diffraction terms from occurring from the base edge. Since a solution for a dielectric top-hat is not readily available, the verification of the solution is complete and the solution of the TGI geometry is assumed correct for the dielectric case based on the above two cases.

4 Analysis of Trunk-Ground Interactions

The trunk-ground interactions are analyzed using the above GTD TGI solution for the scattered fields. For the tree geometries, the diameters of the trees are taken from measurements at a forested area near OSU's Big Ear telescope. The trees in the forest range in diameters from small saplings up to trees 16" in diameter. The analysis consists mostly of trees with DBH 's between 12"-16". These dimensions are large enough for a GTD analysis and comprise a fairly large number of the trees in the forest. Using these diameters and Equations (14) and (17) appropriate heights of the trees can be found. The dielectric constants are chosen based on the results of Chapter 4 for the tree and on Section 2 for the ground. The results of the analysis are described below.

The RCS for a tree with $DBH=14"$ and a corresponding height from Table 4 of 17 meters is shown in Figure 39 at a frequency of 0.75GHz. In the Figure, the top plot is for a cylinder with a dielectric constant of $\epsilon_t=12.4-j4.9$ while the bottom

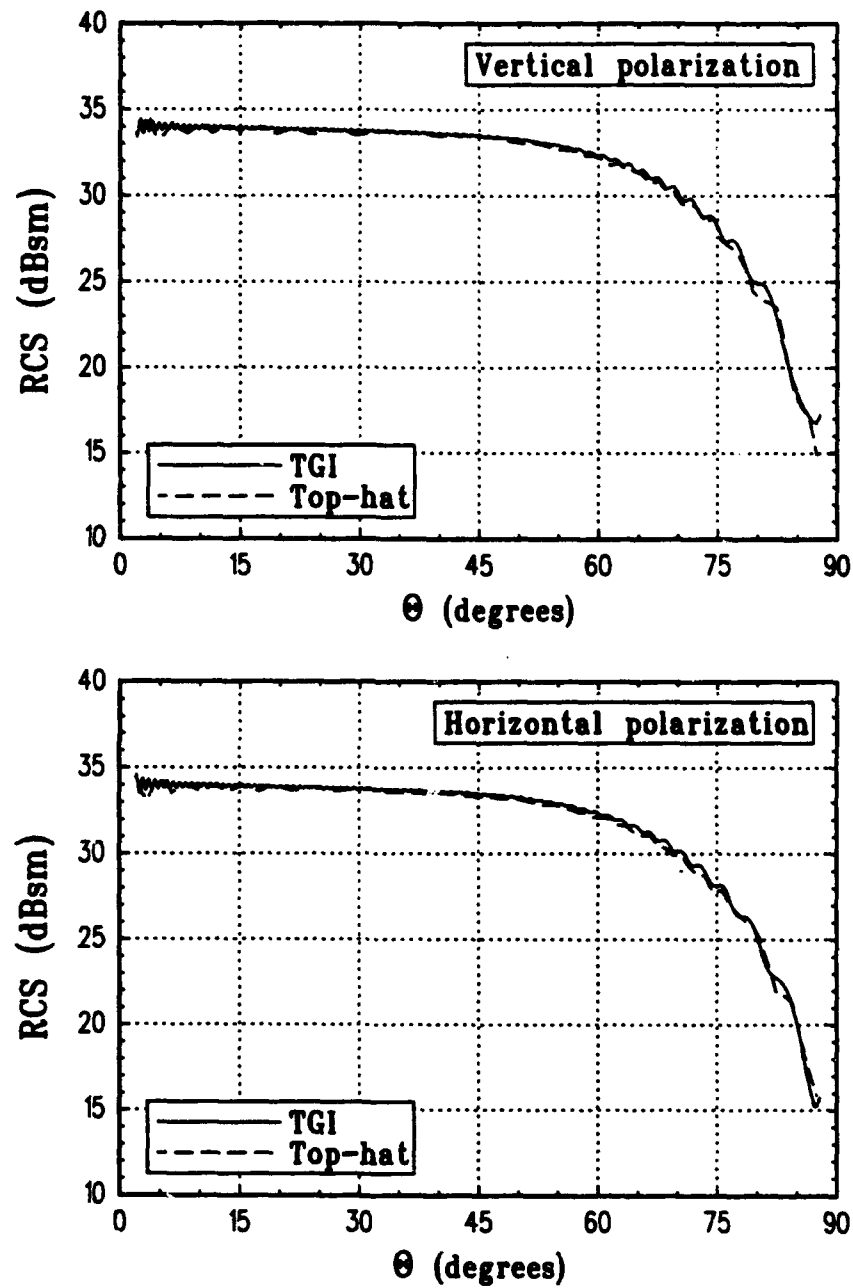


Figure 38: Comparison of top-hat and TGI solutions for the PEC case. The cylinder radius $a=0.2\text{m}$ and height $H=15\text{m}$. The top-hat base is 430 meters for this comparison and the frequency is 0.75GHz .

plot is for a cylinder with a dielectric constant of $\epsilon_t=24.8-j8$. The ground for both plots has a dielectric constant of $\epsilon_g=20-j0.15$ which from Table 3 corresponds to the measured soil at Ohio State University's Big Ear telescope. The same size tree is shown in Figure 40 and Figure 41 for soil dielectric constants of $\epsilon_g=7-j1.5$ and $\epsilon_g=18-j5$, respectively. The effect of the soil and trunk dielectric constants are apparent in the PEC case of Figure 38 where a relatively flat RCS with incidence angle occurs. The dielectric cases show a large null in the pattern around $\theta=15$ degrees and another at around $\theta=75$ degrees for only the vertical polarization but no nulls for the horizontal polarization. These angles correspond to the Brewster angle for the vertical polarization for the dielectric surfaces of the trunk and ground. No nulls are present for the horizontal polarization since the Brewster angle for the horizontal polarization is dependent on the magnetic properties of the material. Since the trunk and ground are assumed to have the permeability of free space (μ_0) the Brewster angle doesn't exist for the horizontal polarization.

The difference in the polarizations is worth further examination. The reflection coefficients from a dielectric half-space are shown in Figure 42 for the dielectric constants used to model the ground and wood. The reflection coefficients for the ground (Γ_g) show a deep null around 15 degrees. The location and depth of the null depend on the exact dielectric material of interest. A similar null is observed in the reflection coefficients for the tree dielectric materials (Γ_t). The reflection coefficient for the tree dielectric constants is shown for a dielectric half-space instead of for a cylinder. This is for ease of computation and to show the inherent behaviour of the dielectric material so the effect of the cylindrical geometry is removed. The inaccuracy caused by this is small since the material is lossy so any contribution due to reflections from the back face of the cylinder would be attenuated and the main contribution will come from the front cylinder face which is similar to the case for a half-space. The reflection coefficient for the vertical polarization shows a similar null for the tree dielectric materials compared to the soil dielectric materials but

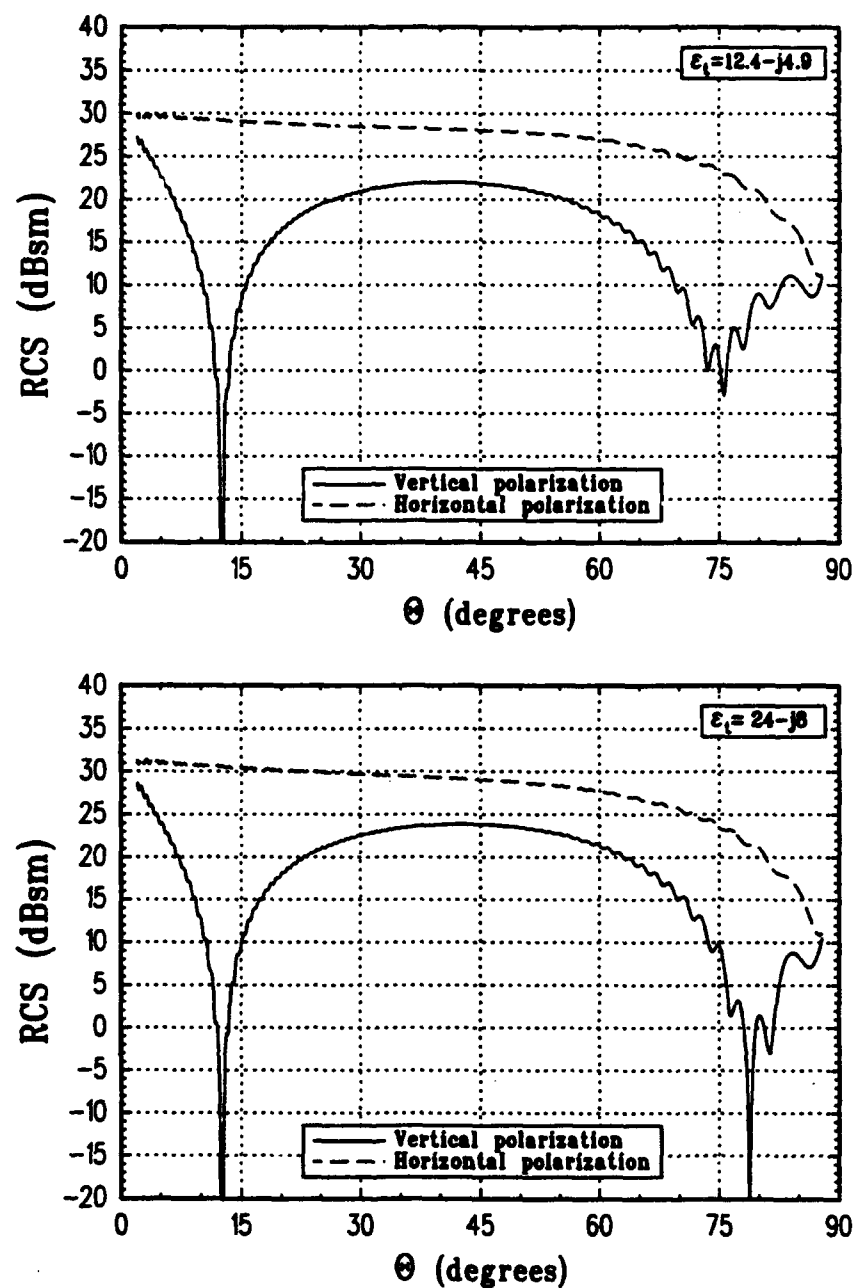


Figure 39: Radar cross section for a tree with $DBH=14''$ and height $h_t=17m$ at a frequency of $0.75GHz$ for both horizontal and vertical polarizations. The relative dielectric constant of the ground is $\epsilon_g=20-j0.15$. The relative dielectric constant of the tree is $\epsilon_t=12.4-j4.9$ for the top plot and $\epsilon_t=24-j8$ for the bottom plot.

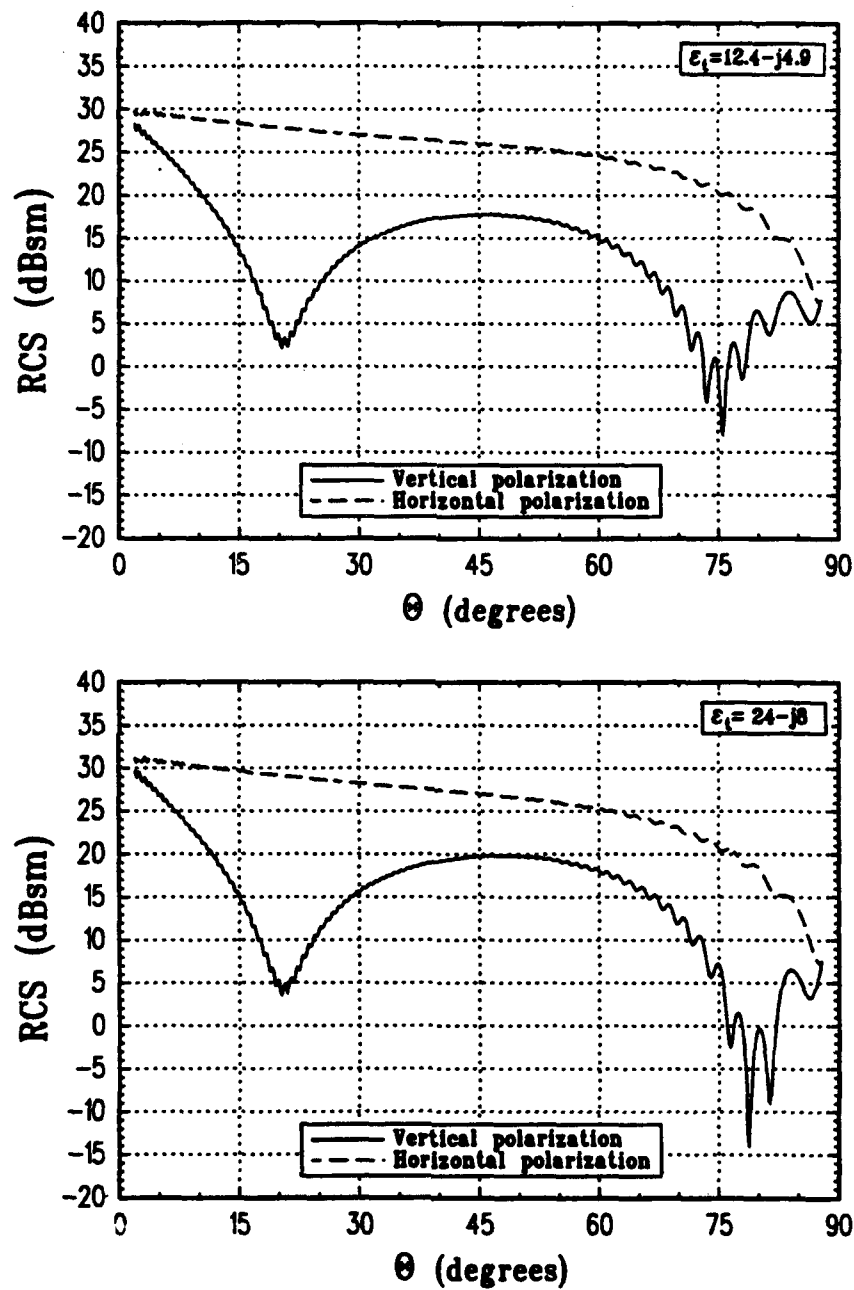


Figure 40: Radar cross section for a tree with $DBH=14''$ and height $h_t=17m$ at a frequency of $0.75GHz$ for both horizontal and vertical polarizations. The relative dielectric constant of the ground is $\epsilon_g=7-j1.5$. The relative dielectric constant of the tree is $\epsilon_t=12.4-j4.9$ for the top plot and $\epsilon_t=24-j8$ for the bottom plot.

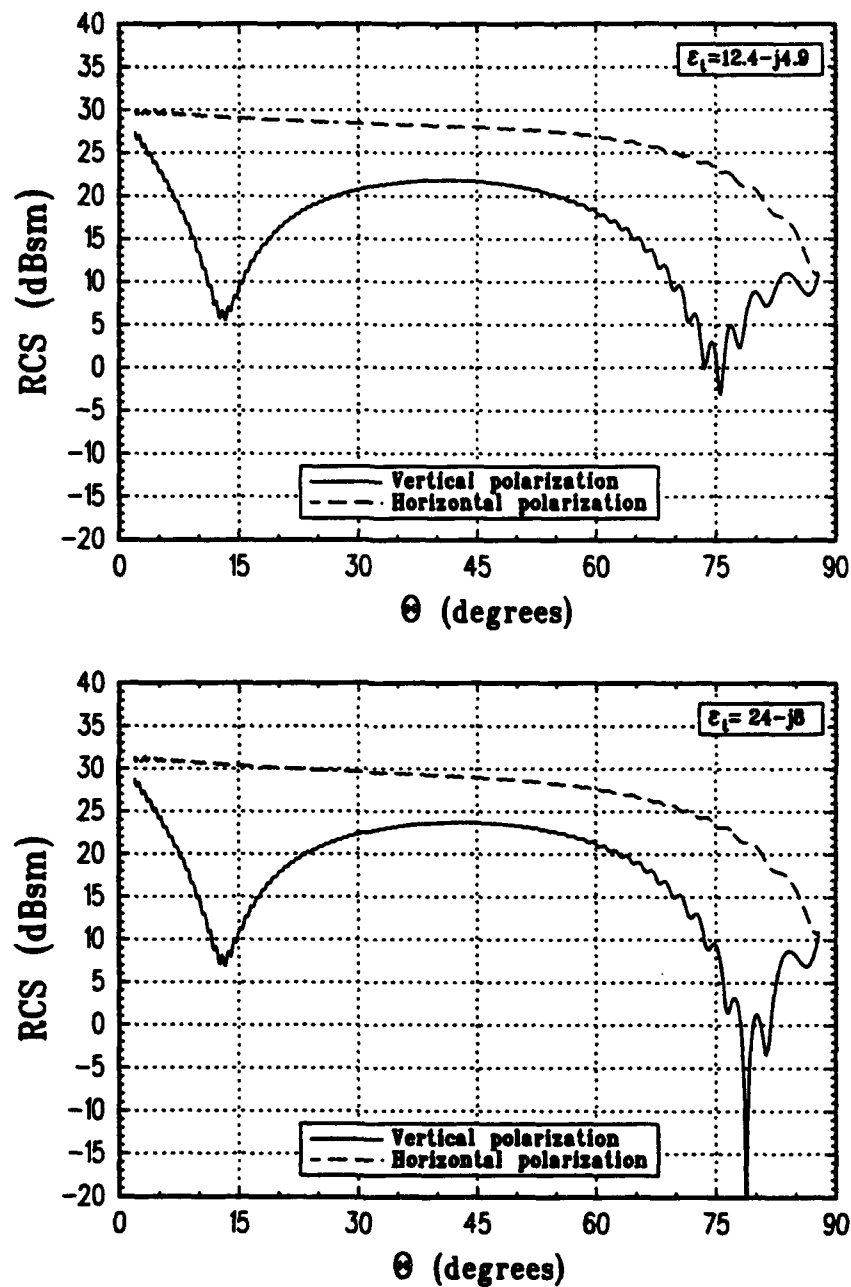


Figure 41: Radar cross section for a tree with $DBH=14''$ and height $h_t=17m$ at a frequency of $0.75GHz$ for both horizontal and vertical polarizations. The relative dielectric constant of the ground is $\epsilon_g=18-j5$. The relative dielectric constant of the tree is $\epsilon_t=12.4-j4.9$ for the top plot and $\epsilon_t=24-j8$ for the bottom plot.

at higher incident angles from horizontal since the dielectric half-space for the tree dielectric constants is oriented vertically.

These nulls in the reflection coefficient significantly affect the RCS of the tree geometry since the dominant contribution to the RCS of the TGI geometry is from the RD and DR terms which represent the dihedral effect between the trunk and the ground. Since the RD and DR terms both are multiplied by the reflection from the ground, a decrease in the ground reflection coefficient will significantly decrease the RD and DR term magnitudes near the ground Brewster angle. This decrease in the reflection coefficient is only for the vertical polarization and not the horizontal polarization. The same effect occurs for the RDR term but the effect of the RDR term is smaller than the effect of the RD and DR terms. As the incidence angle increases, the Brewster angle from the tree surface has a significant effect on the diffracted fields. This can be seen by examining Equation (12) and noting that the reflection coefficient from the dielectric surface (the trunk) modifies the diffraction coefficients. Therefore, as the tree reflection coefficient decreases, the diffracted field will decrease which will affect all the diffraction terms. Therefore, we can conclude that the effect of the reflection coefficients near the Brewster angles on the reflected field from the dielectric surfaces causes a significant difference between the RCS of two polarizations from the tree.

To further illustrate the effect of the dielectric materials on the RCS of the tree, other cases will be examined. In Figure 43, the RCS at 0.75GHz for a tree of $DBH=12''$ with a corresponding effective height h_e from Equation (14) of 11.6 meters. The dielectric constants of the tree are $\epsilon_t=12.4-j4.9$ for one graph and $\epsilon_t=24.8-j8$ for the other graph. The ground dielectric constant is $\epsilon_g=18-j5$ for both plots. The RCS shows the same pattern as shown before for trees with diameters of 16''. This shows that the diameter has little effect on the difference between polarizations. In Figure 44 the same size tree and same dielectric constants as in Figure 43 are used but this time at a frequency of 1.3GHz which is the highest

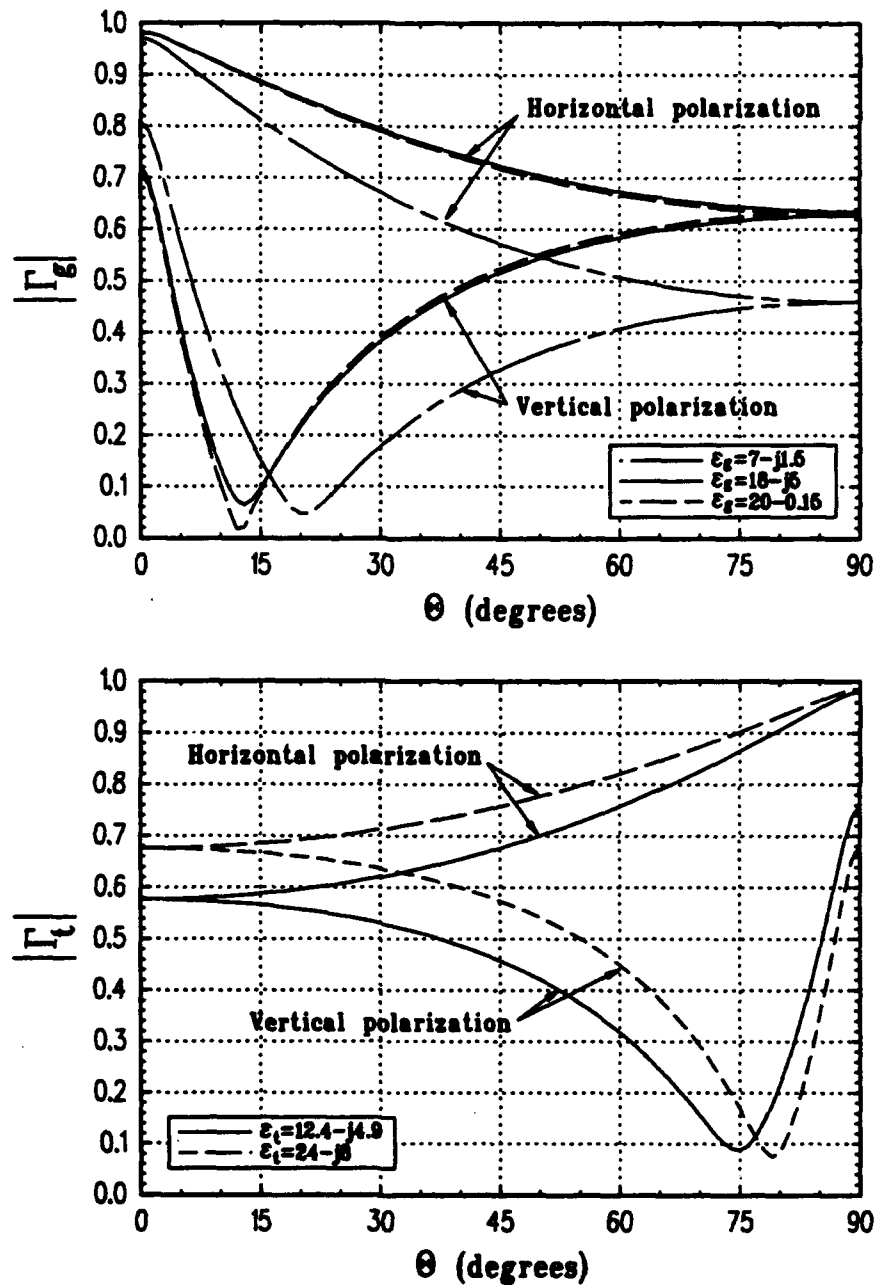


Figure 42: Reflection coefficient from dielectric half-spaces to show the differences in the reflection coefficient (Γ) for the horizontal and vertical polarizations of the dielectric materials used in modeling the trunk-ground interaction. Top plot is of the reflection coefficients for soil dielectric constants (Γ_g) and the bottom plot is of the reflection coefficients for tree dielectric constants (Γ_t).

frequency in the band of interest. Figure 45 shows the RCS for a tree with $DBH=16''$ and a height of 20m at a frequency of 1.3GHz. The dielectric constant of the ground is $\epsilon_g=7-j1.5$. The same difference between the horizontal and vertical polarizations is seen for these tree geometries as in the previous cases.

5 Summary

The analysis of the scattering from a tree trunk including the effect of the ground is examined. The trunk is modeled as a finite length dielectric cylinder and the ground is modeled as an infinite dielectric half-space. The effect of the dielectric constants for the ground and tree is examined. It is found that for all the dielectric constants chosen, the RCS of the tree for horizontal polarization is 5-7dB higher than for the vertical polarization. This is explained by the Brewster angle of the dielectric materials (both the tree and ground). At the Brewster angle, the reflection from the dielectric surfaces is much higher for the horizontally polarized field than the vertically field. The reflection coefficient for the vertical polarization is close to zero at the Brewster angle. This difference in reflection coefficients for the polarizations causes the large difference in the RCS of a tree for the horizontal and vertical polarisations.

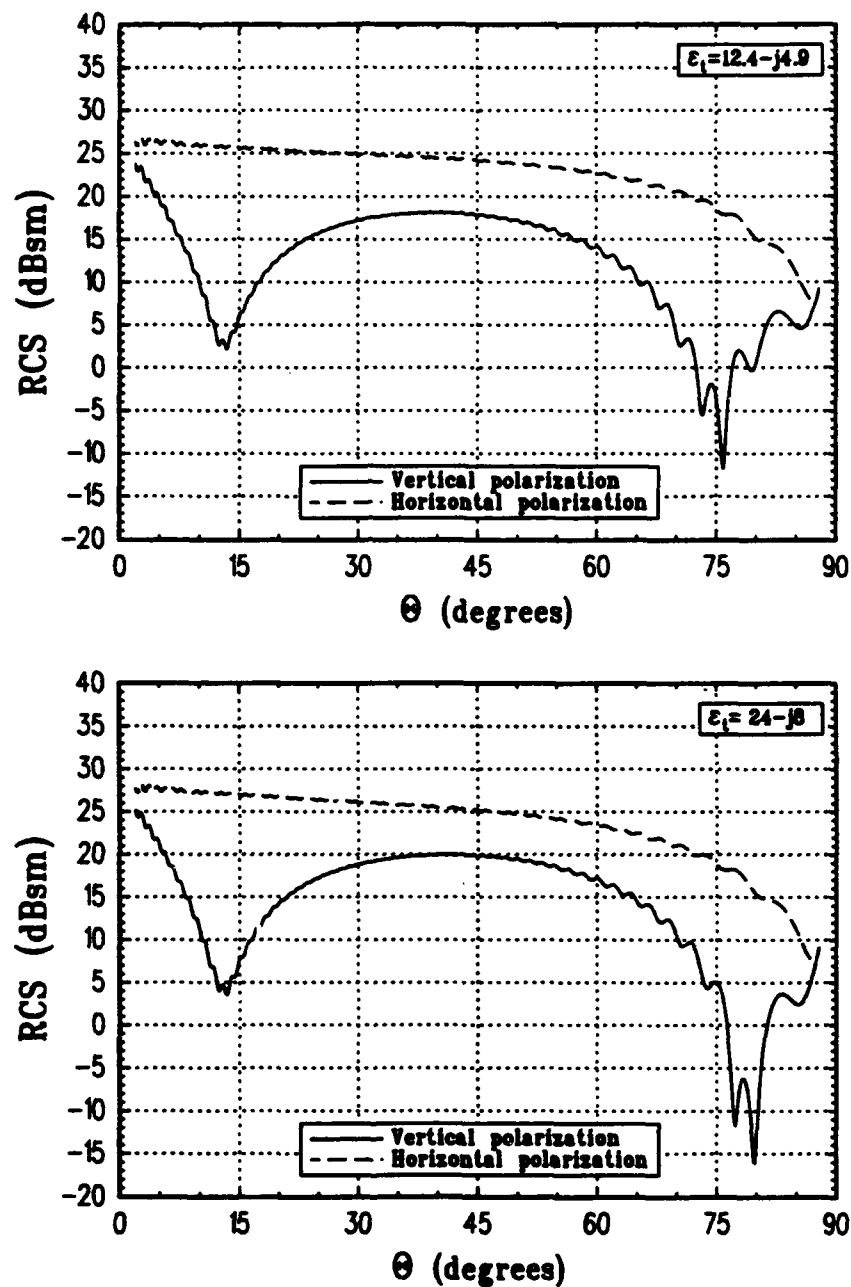


Figure 43: Radar cross section for a tree with $DBH = 12''$ and height $h_t = 14.8m$ at a frequency of $0.75GHz$ for both horizontal and vertical polarizations. The relative dielectric constant of the ground is $\epsilon_g = 18 - j5$. The relative dielectric constant of the tree is $\epsilon_t = 12.4 - j4.9$ for the top plot and $\epsilon_t = 24 - j8$ for the bottom plot.

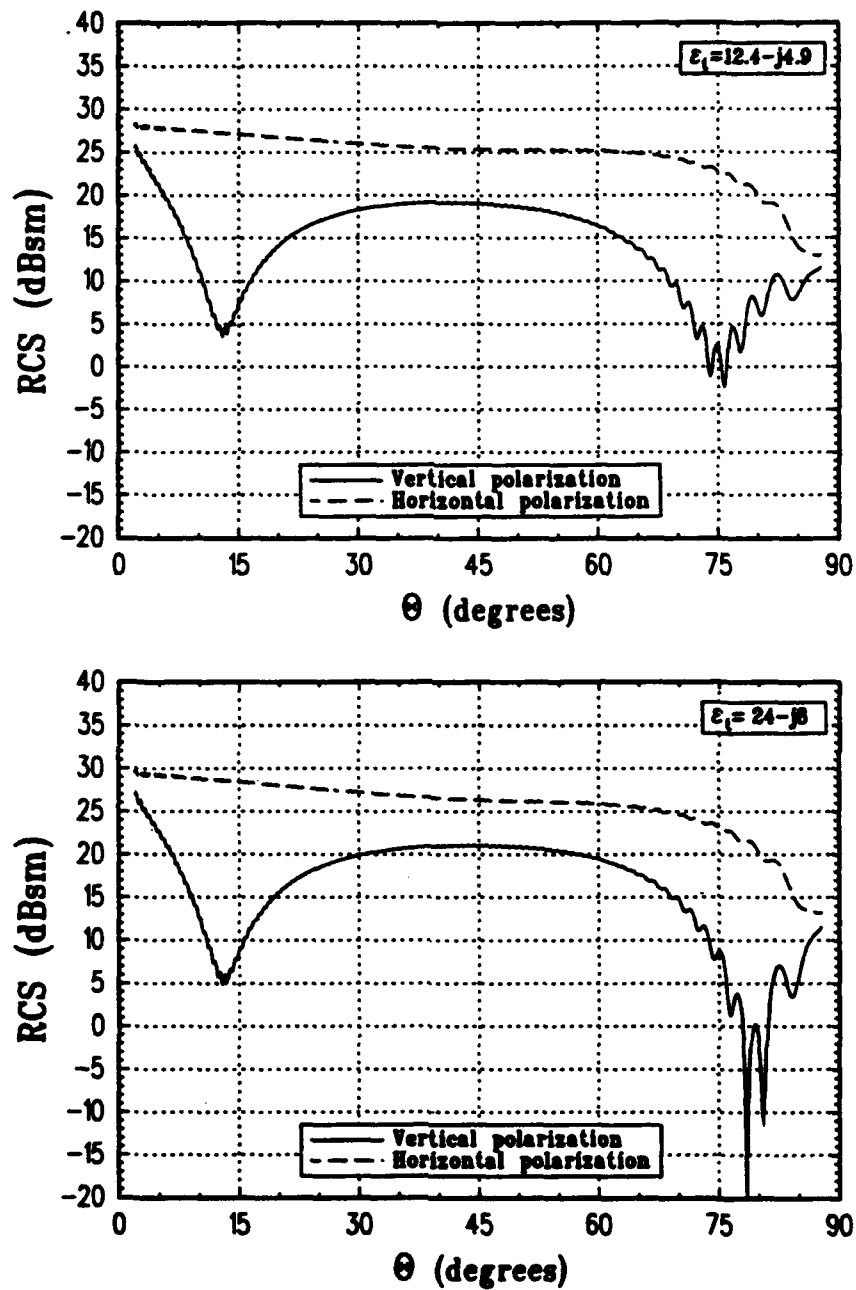


Figure 44: Radar cross section for a tree with $DBH=12''$ and height $h_t=14.8m$ at a frequency of 1.3GHz for both horizontal and vertical polarizations. The relative dielectric constant of the ground is $\epsilon_p=18-j5$. The relative dielectric constant of the tree is $\epsilon_t=12.4-j4.9$ for the top plot and $\epsilon_t=24-j8$ for the bottom plot.

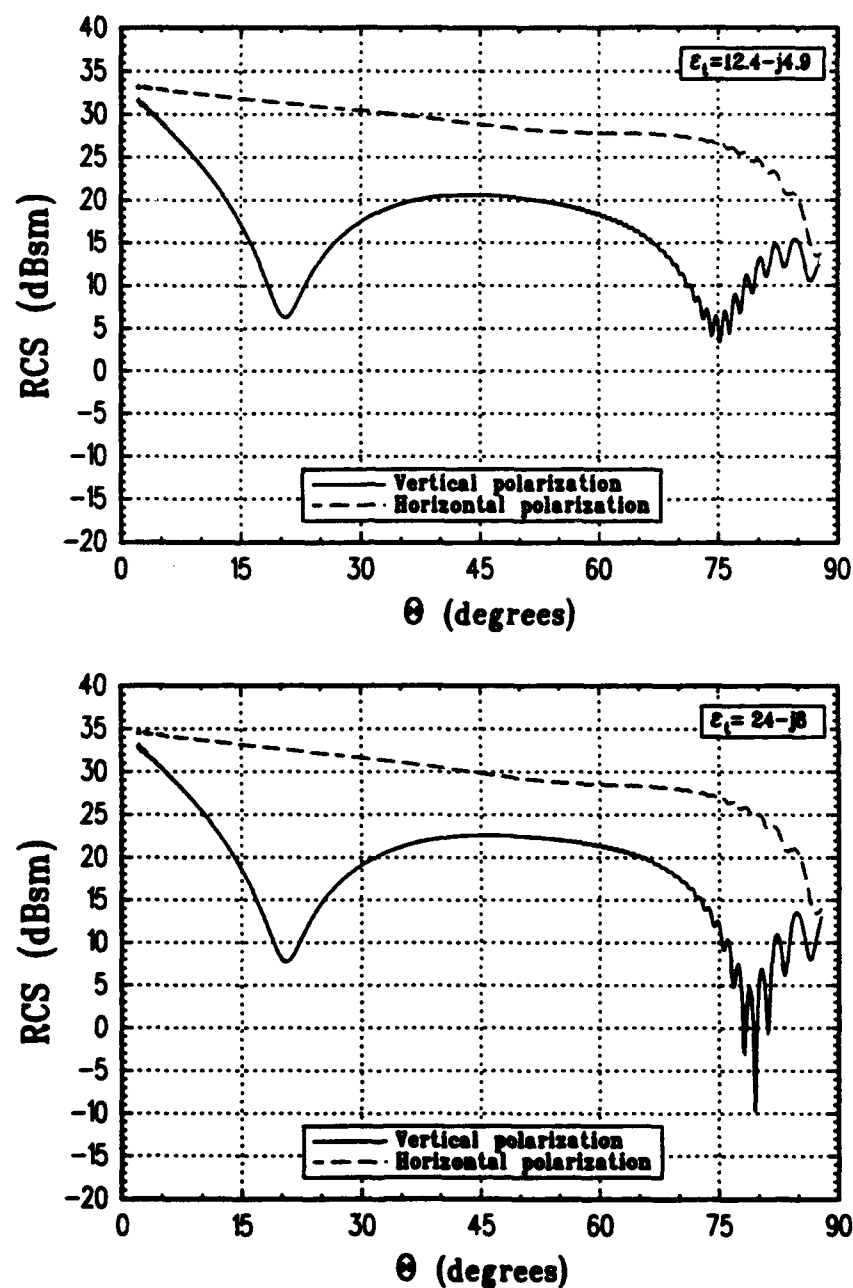


Figure 45: Radar cross section for a tree with $DBH=16''$ and height $h_t=20m$ at a frequency of 1.3GHz for both horizontal and vertical polarizations. The relative dielectric constant of the ground is $\epsilon_g=7-j1.5$. The relative dielectric constant of the tree is $\epsilon_t=12.4-j4.9$ for the top plot and $\epsilon_t=24-j8$ for the bottom plot.

SECTION 7

Branch Scattering

1 Introduction

This chapter discusses the scattering from tree branches. In Chapter 6 the scattering due to the dihedral between the trunk and ground is studied. The polarization difference in the RCS of the trunk-ground is also shown in Chapter 6. The question now is where does the level of scattering from branches compare to the level of scattering from the trunk-ground interaction. Due to the complexity of tree branches, a solution involving all the scattering interactions would be very complex. Therefore, a simplified branch geometry that fits the needs of the analysis must be decided upon. The geometry consists only of the interactions between a single branch and the trunk. This involves analyzing the scattering from the dihedral between a tree branch and trunk, and the specular scattering from the side of a tree branch. To find the level of scattering from branches, it is desired to find the maximum scattering from a single branch that could be expected. To accomplish this, a series of worst case scenarios are analyzed that will provide the highest level of scattering from tree branches that would occur. Based on the results for a single branch, the importance of the scattering from branches can be deduced.

The analysis consists of modeling the tree trunk and branches with dielectric cylinders as is done in Chapters 4 and 5. The dielectric constants are chosen based on information in the literature that is presented in Table 1 and on the results of

Chapter 4. The wood models are then used in a UTD solution for dihedrals of dielectric cylinders. Based on this analysis, a level for the RCS from a branch is found.

2 Modeling of Branch Scattering

The actual geometry of tree branches is very complex and is beyond the level of analysis desired. The purpose of the analysis is to find a level for the scattering from a single branch and, therefore, decide on the importance of branch scattering compared to the trunk-ground interactions. Since the exact level of branch scattering is not of interest, an attempt will be made to simplify the analysis. As already discussed in Section 2, the geometry of the tree can be simplified for the frequencies of interest to eliminate many of the smaller tree branches leaving only the larger branches and the trunk. While a more complete modeling of the branches would account for the various interactions between the trunk and the numerous branches, this analysis is currently too complex for the results desired.

Since the exact level of branch scattering is not desired and only the maximum level of branch scattering, a worst case scattering analysis is done. To do this, it is observed that for a field incident on the tree, many of the larger tree branches will be oriented at oblique angles to the incident field. The backscattered field for oblique incidence will be small and, therefore, this case will be ignored. The dominant effect will be when the incident field is near normal incidence (specular) on the side of a branch. This will have a much larger backscattered field than the oblique incidence case. It is also observed that the larger branches of a tree are oriented at many different angles with respect to the vertical axis of the tree trunk. The angle between the trunk and the branch form a dihedral which can have a significant backscattered field if the incident field is in the plane of the dihedral. The dihedral effect will be largest for backscatter if the angle between the branch and trunk is 90 degrees. Using this reasoning, the only branch scattering effects of interest are the

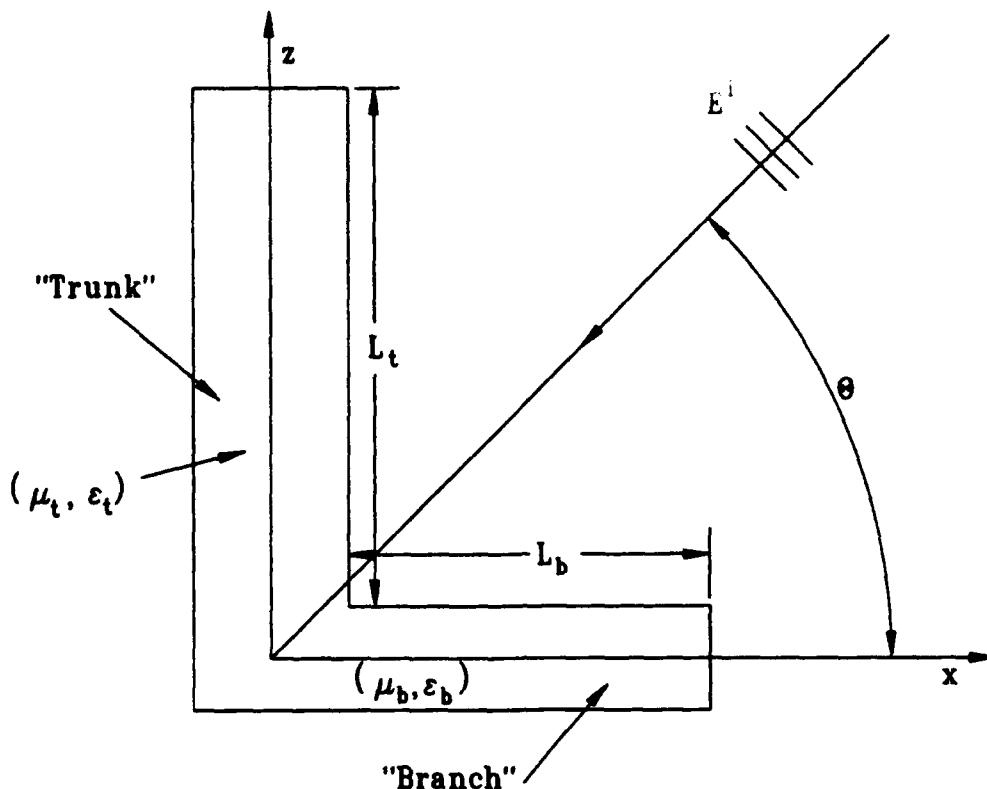


Figure 46: Geometry used to model branch scattering.

specular scattering from the side of a tree branch and the dihedral effect between the trunk and branch. All other scattering effects will be ignored including higher order interactions between the branches because these effects will be small compared the two main effects mentioned above.

The geometry that will be analyzed is shown in Figure 46. It consists of two finite length dielectric cylinders at a 90 degree dihedral angle. For this geometry, a horizontally polarized wave is oriented normal to the x - z plane while a vertically polarized wave is parallel to the x - z plane. The backscattered field is calculated using the UTD solution formulated in [25] and briefly summarized in Appendix C. Care must be taken when using this solution to guarantee that the diameters of the dielectric cylinders are greater than approximately 0.7 wavelengths otherwise the

UTD solution will break down. For this geometry, the specular scattering from the side of a branch will occur for $\theta=90$ degrees.

To model the scattering from a tree branch, the sizes and dielectric constants of the cylinders must be decided upon. The dielectric constants of the wood are modeled using the same values that are found to compare with measurements in Chapter 4. The lengths of the dielectric cylinders are taken from Equation (17). Unfortunately, these equations only provide an effective tree height h_t and height to maximum crown diameter h_u . However, these equations can be used to derive approximate values for the lengths of the dielectric cylinders used in the modeling. And since only a worst case analysis is of interest, the approximations of the length are appropriate if chosen correctly.

Therefore, using Equation (17), if the diameter of the tree (DBH) is known then the height to the widest part of the canopy h_u and the effective height of the tree h_t can be found. It is then assumed that the longest branches occur at the widest part of the canopy. While this assumption may not always be valid, we are assuming a 90 degree dihedral which forces the longest branches to occur at the widest part of the canopy. The length of the tree cylinder L_t is then taken as the difference between the effective height of the tree h_t and the widest part of the canopy h_u . The diameter of the cylinder used to model the trunk is taken as the DBH of the tree. These assumptions will significantly overestimate the actual dimensions of the trunk since in the model, the cylinder has a constant diameter but in an actual tree the trunk will be tapered.

For the diameter and length of the branch cylinder, other approximations are used. The literature is short on details on the modeling tree branches and formulas relating tree size to branch sizes. Therefore, since only a worst case analysis is of interest, an intuitive model is used that will still provide physically realistic dimensions but will overestimate the actual dimensions of the branches to provide a maximum level of the RCS from a branch. Accordingly, it is assumed that the

branch and tree have approximately the same dielectric constants which should be a reasonable assumption for the larger branches which are the only ones of interest here. The diameter of the branch will be taken to be equal to the diameter of the trunk. This is justified since it would be unrealistic for a branch to have a larger diameter than the tree and setting the diameters equal will provide a worst case scenario. Choosing an appropriate length for the branch is more difficult. Setting the branch length equal to the trunk length would provide a worst case analysis but would be highly unrealistic and nonphysical. Therefore, the length of the branch cylinder will be arbitrarily taken as one-half the length of the trunk. This length is more realistic than making the lengths equal but should still provide an overestimation of the RCS of the branch. Also, the branch is modeled as a constant radius, straight cylinder but since an actual branch is tapered and usually bent, the actual RCS of a branch is overestimated. These dimensions for the branch overestimate the actual dimensions and, therefore, the scattering for a tree branch.

3 Analysis of Branch Scattering

The diameters used for the tree trunk are based on a survey of trees in the woods surrounding the Ohio State University Radio Telescope known as Big Ear. The tree survey showed that there are a large number of trees with *DBH*s between 12 and 16 inches (0.30 and 0.41 meters). Therefore, the cylinders used to model the trunks and branches will be between 0.3 and 0.41 meters in diameter. Using these values in Equation (17) the lengths L_t and L_b can be found as discussed previously. These dimensions are summarized in Table 5 for various *DBH* values.

The dimensions from Table 5 are then used with the dielectric constants from Chapter 4 to find a level for the scattering from tree branches. The RCS from the branch dihedral for a tree with a *DBH*=12" and dielectric constant of $\epsilon_b = \epsilon_t = 12.4 - j4.9$ is shown in Figure 48 for both horizontal and vertical polarizations at a frequency of 0.75GHz. For comparison, the RCS for the same size tree but with a dielectric

Table 5: Diameters of trees (DBH) and the corresponding cylinder lengths used in modeling branch scattering for worst case analysis.

DBH	tree cylinder length (L_t)	branch length (L_B)
12" (0.3048m)	5.26m	2.63m
14" (0.3556m)	6.06m	3.03m
16" (0.4064m)	6.86m	3.43m

constant of $\epsilon_b = \epsilon_t = 24 - j8$ is shown in Figure 49 at the same frequency. For both Figures 48 and 49, the RCS for horizontal polarization is greater than the RCS for vertical polarization. For comparison, a branch dihedral of the same size and at the same frequency is shown in Figure 47 but for a PEC case. The PEC case doesn't show the same difference in the horizontal and vertical polarizations that the dielectric cases show. This difference in the polarizations is due to the reflection coefficients from the branch surface being smaller for vertical polarization than for horizontal polarization. This is due to the decrease in the reflection coefficient for vertical polarization near the Brewster angle as is described in Chapter 6. Therefore, the differences in the two polarizations are due to the same reasons as is explained for the polarization differences of the GTI geometry in Chapter 6.

The RCS of the branch dihedral should be examined more closely. For θ near 0 degrees, most of the scattering is from the trunk cylinder and not the branch. The trunk scattering is discussed in detail in Chapter 6 and isn't important for the current analysis of branch scattering. Near $\theta = 90$ degrees the scattering is mainly from the specular scattering from the side of the branch cylinder. The RCS for the branch is less than 7 dBsm for the geometries in Figures 48 and 49. For the dihedral region, the scattering for the horizontal and vertical polarizations are approximately 5 dB different.

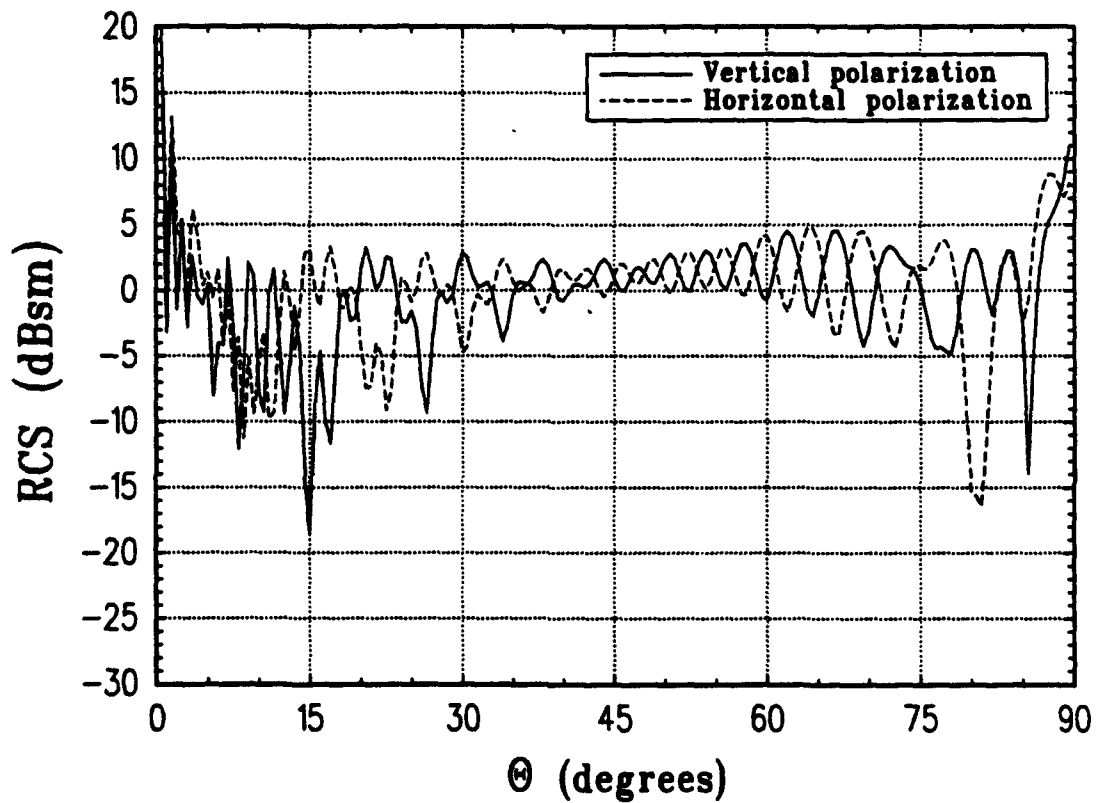


Figure 47: Radar cross section of 90 degree PEC cylindrical dihedral with diameters of 12" for comparison to the dielectric case of scattering from a tree-branch dihedral at a frequency of 0.75GHz.

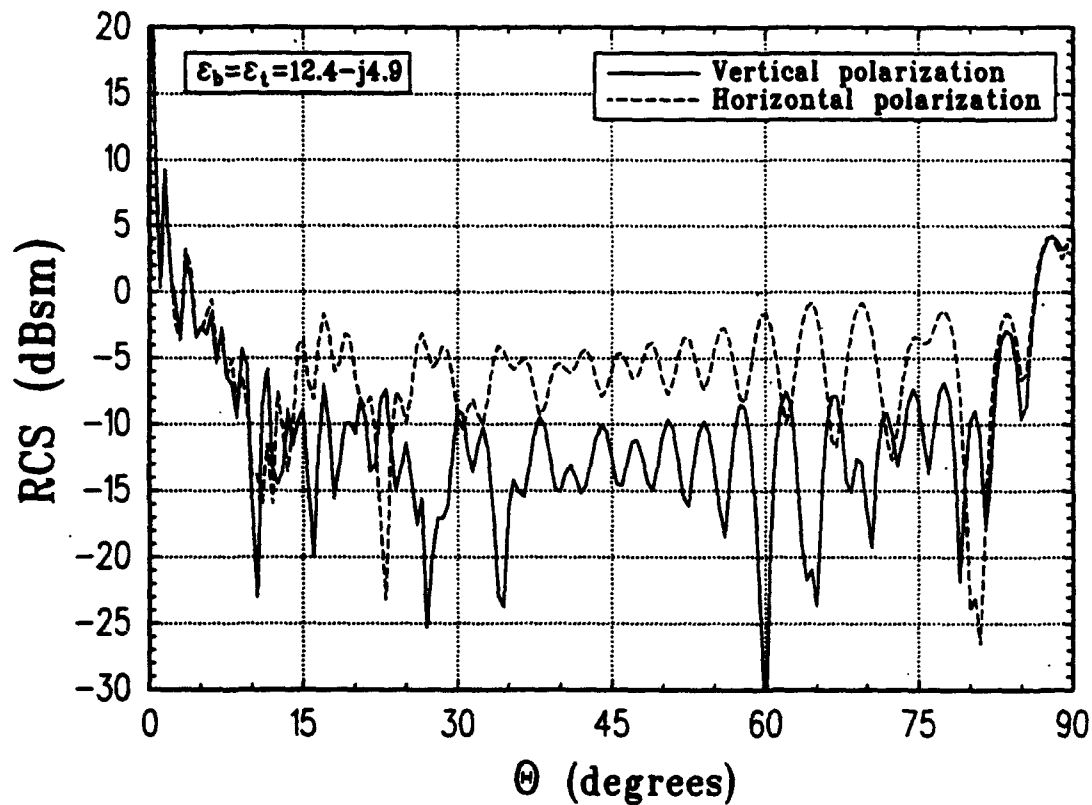


Figure 48: Radar cross section of 90 degree cylindrical dihedral to simulate the scattering from a tree-branch dihedral at a frequency of 0.75GHz. The tree diameter (DBH) is 12" with a relative dielectric constant of $\epsilon_b = \epsilon_t = 12.4 - j4.9$.

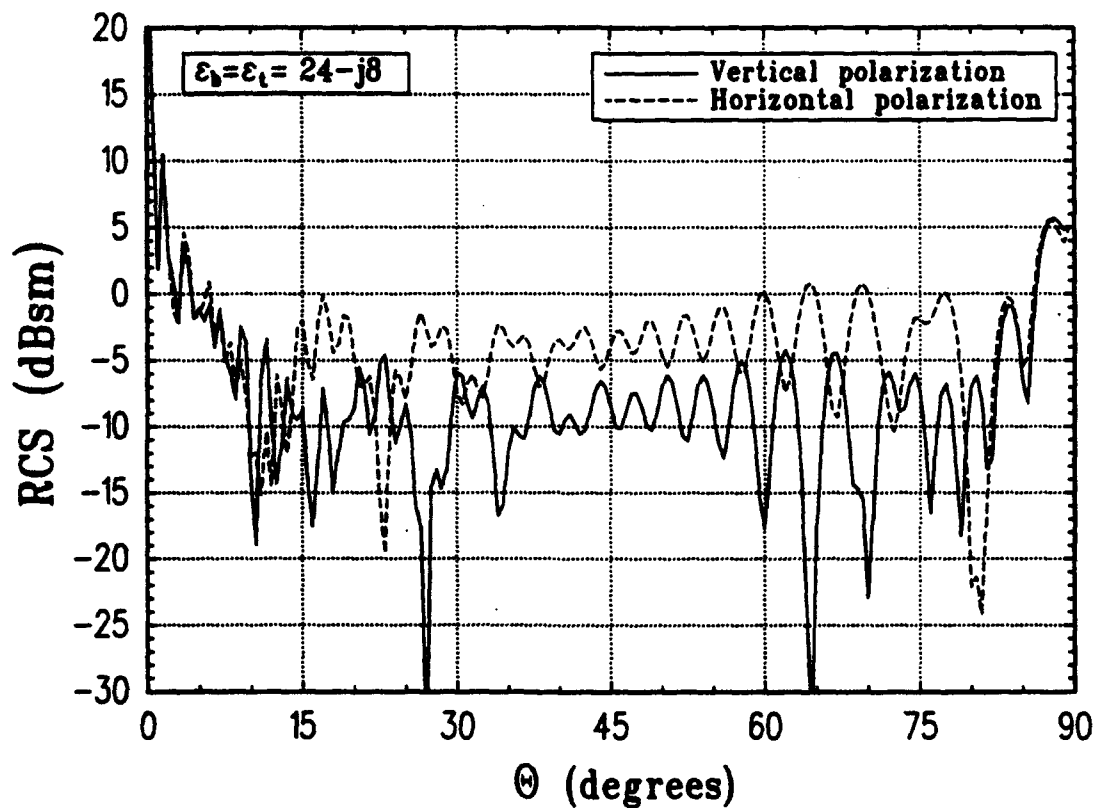


Figure 49: Radar cross section of 90 degree cylindrical dihedral to simulate the scattering from a tree-branch dihedral at a frequency of 0.75GHz. The tree diameter (DBH) is 12" and a relative dielectric constant of $\epsilon_b = \epsilon_t = 24 - j8$.

To further illustrate the scattering from branches, several more geometries are analyzed. The RCS for a $DBH=14''$ tree with dielectric constants of $\epsilon_b = \epsilon_t = 12.4 - j4.9$ and $\epsilon_b = \epsilon_t = 24 - j8$ is shown in Figure 50 for both horizontal and vertical polarizations at a frequency of 0.75GHz. In Figure 51, the RCS at 0.75GHz of a tree with $DBH=16''$ and with dielectric constants of $\epsilon_b = \epsilon_t = 12.4 - j4.9$ and $\epsilon_b = \epsilon_t = 24 - j8$ is shown. In Figure 52, the RCS of the same tree with $DBH=16''$ and with dielectric constants of $\epsilon_b = \epsilon_t = 12.4 - j4.9$ and $\epsilon_b = \epsilon_t = 24 - j8$ is shown but at a frequency of 1.3GHz which is the highest frequency in the band of interest. By comparing Figures 48, 49, 50, and 51 it is seen that the size of the branch (diameter and length) doesn't affect the shape of the RCS considerably. The size mainly causes the RCS of the branches to shift upward for larger size branches. The difference between the RCS for the horizontal and vertical polarizations is nearly independent for the branch sizes analyzed and is always approximately 5 dB. The largest RCS in the dihedral region of the geometries analyzed is for the geometry of Figure 52. The RCS is less than approximately 5dBsm in the dihedral region and is less than 12 dBsm for the specular scattering from the log. The log for Figure 52 is 16'' in diameter which is the largest tree size in the woods at OSU's radio telescope and the frequency is the highest in the band of interest. Since the dimensions used in the analysis are the largest that are reasonable for the worst case analysis, the case in Figure 52 is representative of the largest RCS for branch scattering for the tree sizes and frequencies of interest.

4 Summary

A model for the scattering from the dihedral formed by the tree trunk and a branch is presented. The analysis consists of a worst case analysis to show the highest level of branch scattering that could be expected. As a result, the sizes of the cylinders used to represent the branches and trunk are picked as large as considered reasonable based on formulas for tree height and on intuition about branch sizes. The resulting

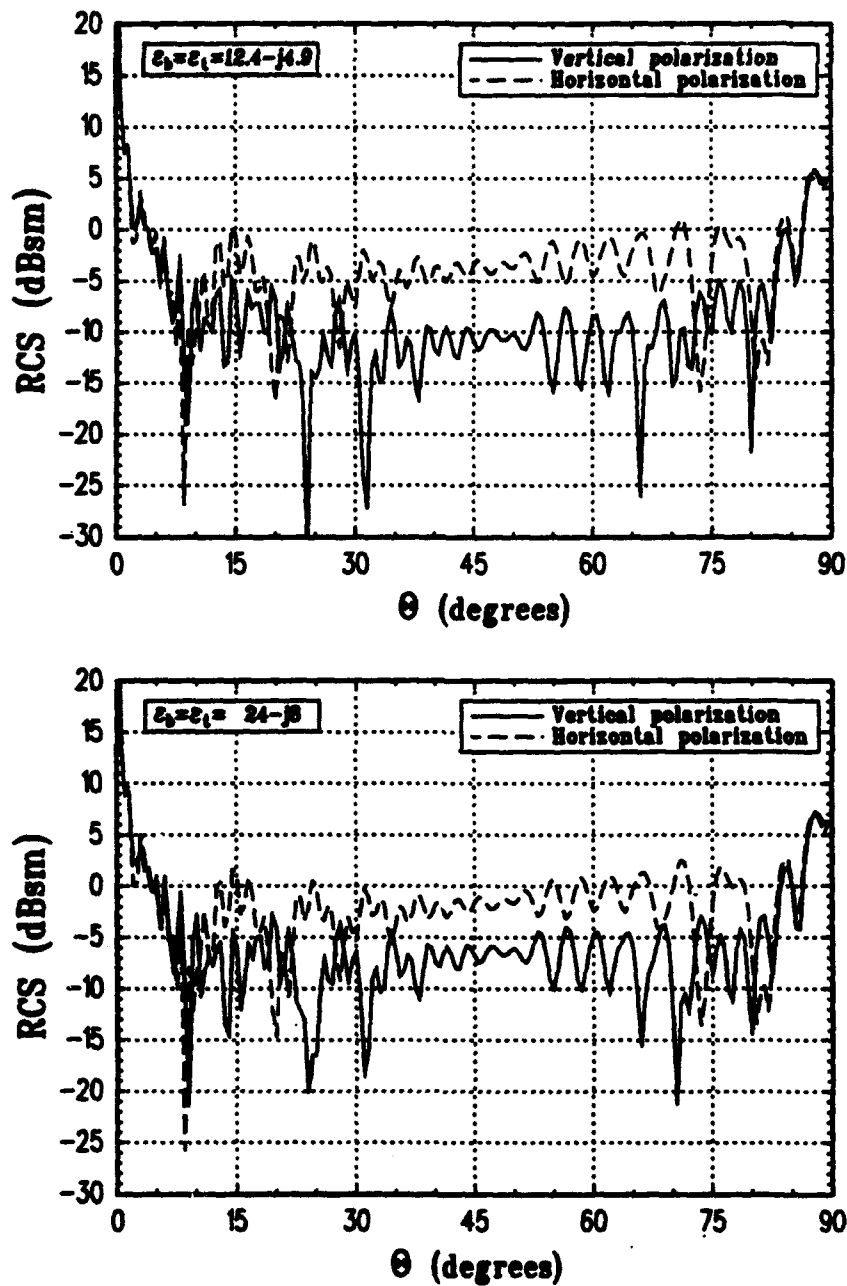


Figure 50: Radar cross section of 90 degree cylindrical dihedral to simulate the scattering from a tree-branch dihedral at a frequency of 0.75GHZ. The tree diameter (DBH) is 14" with relative dielectric constants of $\epsilon_s = \epsilon_t = 12.4 - j4.9$ and $\epsilon_s = \epsilon_t = 24 - j8$.

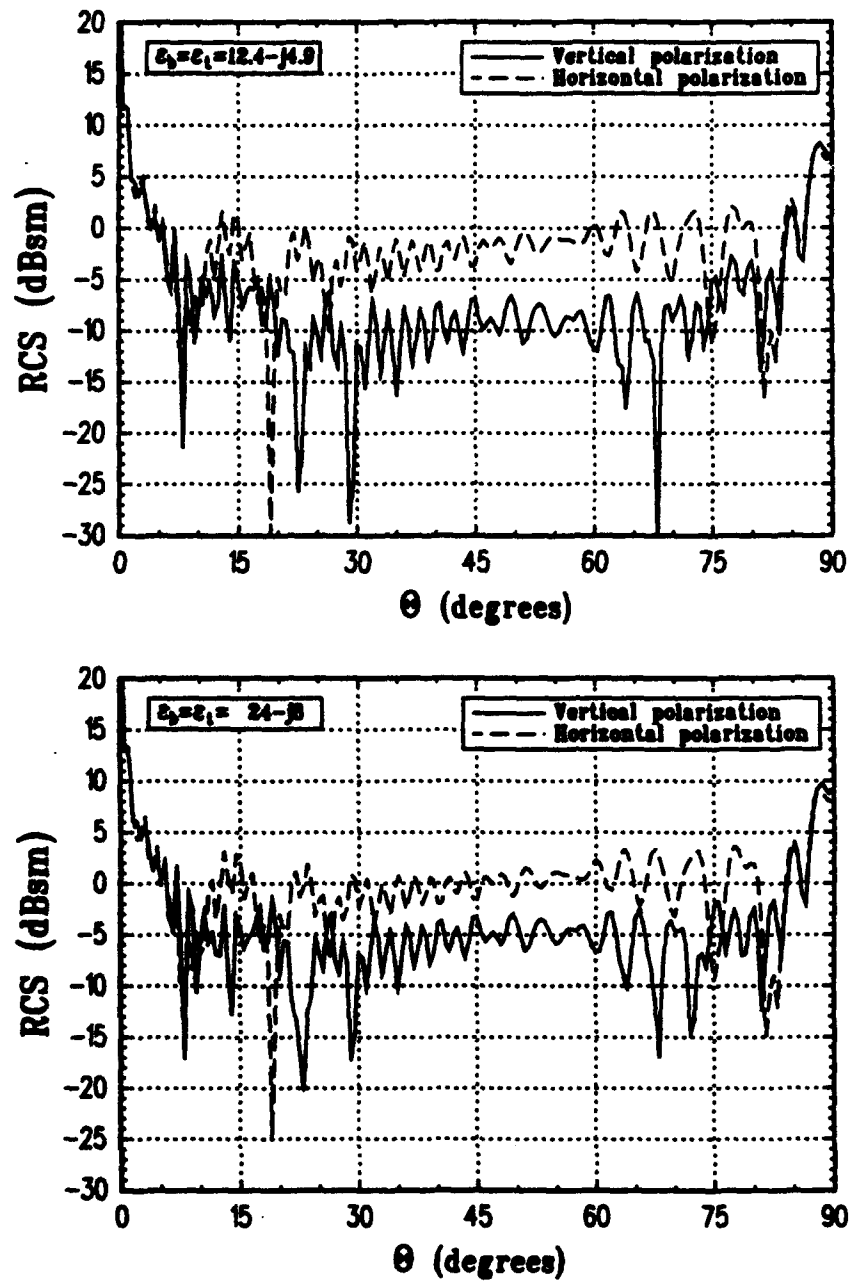


Figure 51: Radar cross section of 90 degree cylindrical dihedral to simulate the scattering from a tree-branch dihedral at a frequency of 0.75GHz. The tree diameter (DBH) is 16" with relative dielectric constants of $\epsilon_s = \epsilon_t = 12.4 - j4.9$ and $\epsilon_s = \epsilon_t = 24 - j8$.

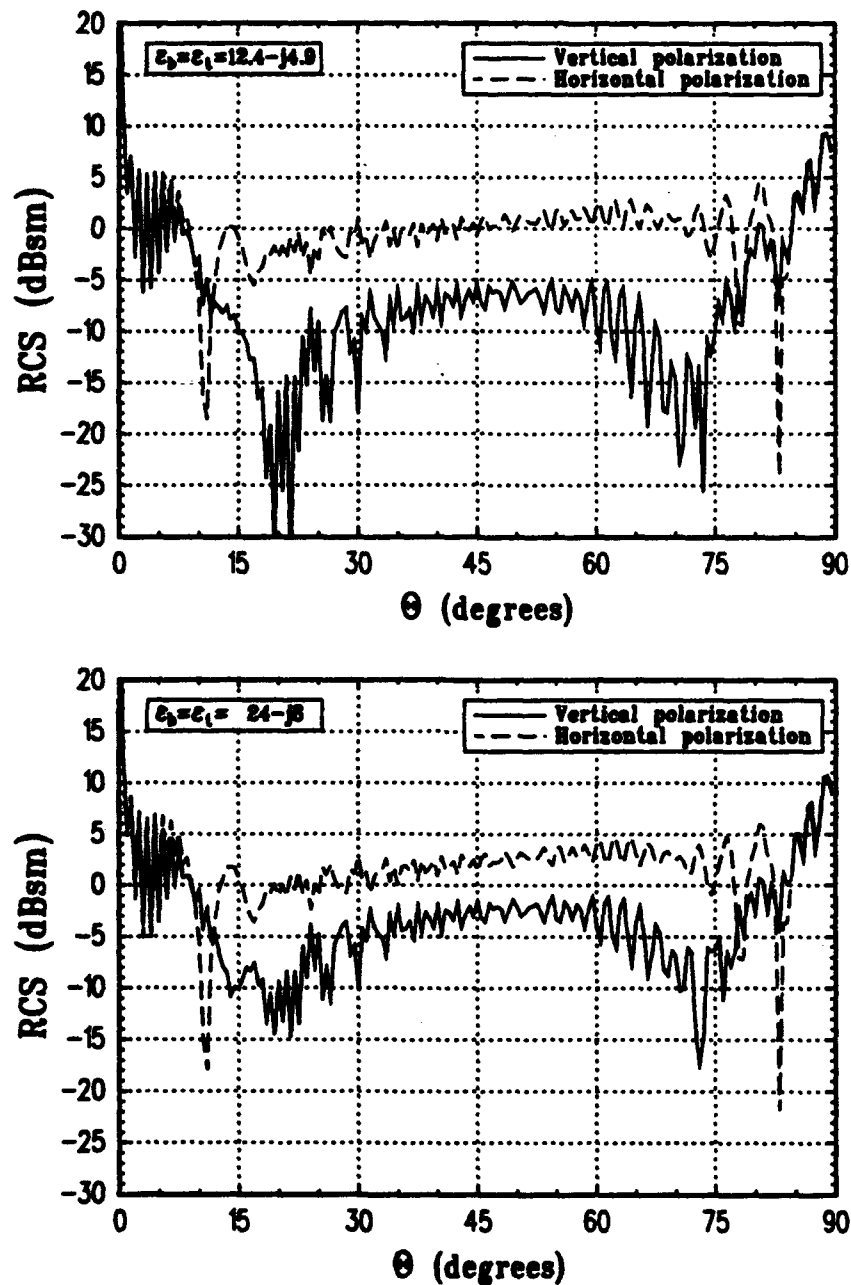


Figure 52: Radar cross section of 90 degree cylindrical dihedral to simulate the scattering from a tree-branch dihedral at a frequency of 1.3GHz. The tree diameter (DBH) is 16" with relative dielectric constants of $\epsilon_b = \epsilon_t = 12.4 - j4.9$ and $\epsilon_b = \epsilon_t = 24 - j8$.

model overestimated the RCS of actual branches since in modeling, the branches and trunk are modeled as perfectly straight and of constant diameter whereas for actual trees the branches and trunk are bent and tapered so the actual geometry will have a lower RCS than modeled. Using this worst case analysis, the maximum RCS for a tree branch is less than 5 dBsm in the dihedral region between the trunk and branch and would be much less out of the dihedral plane. The specular scattering from a branch is less than 12 dBsm. While the specular scattering from a branch is greater than the dihedral region, the chances of the incident field impinging exactly perpendicular to a branch is small and, therefore, the scattering from a tree branch will be smaller than calculated. Therefore, it is shown that the highest level of scattering from branches is approximately 20dB lower than the scattering from the trunk-ground interaction in the dihedral region.

SECTION 8

Summary and Conclusions

The electromagnetic scattering from the trunk and branches of a tree is analyzed. To solve for the scattered field, the modified Geometrical Theory of Diffraction is used. Before the scattering from tree can be analyzed, some background information is required. A summary of the current techniques and methods of modeling trees is presented. The geometry used for a low-frequency model of the trunk and branches is shown. The corresponding dielectric information for modeling wood is presented. But before the trunks and branches are analyzed, the scattering from tree logs is examined. These measurements are used to find a set of values that are presented in the summary that can appropriately be used to model the types of wood of interest. A set of dielectric constants for wood are found and used in modeling logs to closely match the measured RCS. It is also found that the surface roughness can be ignored for frequencies below approximately 6GHz for the trees of interest. A method is presented that could be used to match the measured RCS of a log to theory using a roughness model for the wood surface. But due to sensitivity in the model to the surface roughness and the variation of the RCS of the same section of a trees trunk, it is shown that this method isn't recommended in modeling the RCS from a tree trunk above 6GHz.

The results for the modeling of a tree are combined with the information presented to calculate the scattered fields in the vicinity of a tree trunk. It is shown

that the scattered field near a tree trunk is relatively insensitive to the constituent parameters of the tree. Also, the blockage in the forward scatter region caused by the trunk is shown to be large and decreases slowly with distance from the trunk and is shown to be approximately 1dB at 30 meters from the trunk. It is also shown that the method of calculating the scattered field near a tree trunk at normal incidence can be used for oblique incidence of finite length cylinders. However, its applicability fails for large angles of incidence and/or for large distances from the cylinder when a direct ray between the source and field point dominates the near-zone scattered field.

The backscattered field of a tree trunk is examined next. First the effect of the trunk-ground interactions (TGI) is examined. The modified Geometrical Theory of Diffraction is used to find the scattered field for this geometry. It is found that the scattered field for horizontal and vertical polarizations is approximately 7dB different in the dihedral region between the trunk and the ground. This is explained by the decrease in the reflection coefficient for both the trunk and ground dielectric surfaces near the Brewster angle for vertical polarization. The Brewster angle for the horizontal polarization isn't present for this geometry since no magnetic materials are used in the modeling.

To determine the effect of the scattering from branches, the dihedral between the branch and trunk is examined. The purpose is to find a level for the scattering from a branch and, therefore, to find the importance of branch scattering compared to the trunk-ground interactions. Therefore, since the exact level of the scattering from a branch isn't important but the maximum level is, a worst case analysis is examined. This allows the branch geometry to be greatly simplified. It is found that the scattered field in the dihedral region of the branch scattering is approximately 20dB lower than the TGI scattering in the same region. The maximum level of branch scattering occurs for normal incidence on the side of the branch and is less than 12dBsm. But, since the incident field will rarely be normally incident on the

branch, the branch scattering should be less. The branch scattering also exhibits the same difference in the RCS for the dihedral region between the horizontal and vertical polarizations as the TGI geometry. The cause for the difference is also due to the change in the reflection coefficient near the Brewster angle as is the cause for the difference in the TGI geometry. Since the scattering from a single branch is much less than the scattering from the TGI interactions, for several branches, the level of branch scattering will increase but the TGI will remain larger for a single tree.

In conclusion, for the low frequencies of interest, simplifications can be made in modeling the scattering from the trunks and branches of trees. Also, the higher order terms between branches and the branch and the ground will be much smaller than the main branch scattering for the geometries of interest and, therefore, are ignored. The leaves, smaller branches, and higher order terms were ignored in the analysis, but would need to be included to completely model the scattering from a tree.

Appendix A

Reflection and Transmission of plane waves in Planar, Stratified (multilayered) Medium

Details of reflection and transmission of the plane wave in multilayered medium are presented in [10]. Here a summary of [10] is presented. Suppose a plane wave in free space has oblique incidence on a plane multilayer consisting of N homogeneous isotropic slabs as shown in Figure 53. Let d_n , μ_n , and ϵ_n represent the thickness, permeability, and permittivity of slab n . The slabs are considered to have infinite width and height and parallel surfaces, with unbounded free space on both sides of the multilayer. The incident plane wave impinging on the left-hand surface of the multilayer is given, in the TE case (i.e., perpendicular polarization) by:

$$E_x^i = E_0 e^{jk_0 y \sin \theta} e^{jk_0 z \cos \theta}, \quad (35)$$

where θ is the angle of incidence, $k_0 = 2\pi/\lambda$, and λ is the free space wavelength. The reflected wave is given by:

$$E_x^r = R E_0 e^{jk_0 y \sin \theta} e^{-jk_0 z \cos \theta}, \quad (36)$$

where R is the reflection coefficient of the multilayer. The transmitted plane wave on the right-hand side of the multilayer is represented by:

$$E_x^t = T E_0 e^{jk_0 y \sin \theta} e^{jk_0 z \cos \theta}, \quad (37)$$

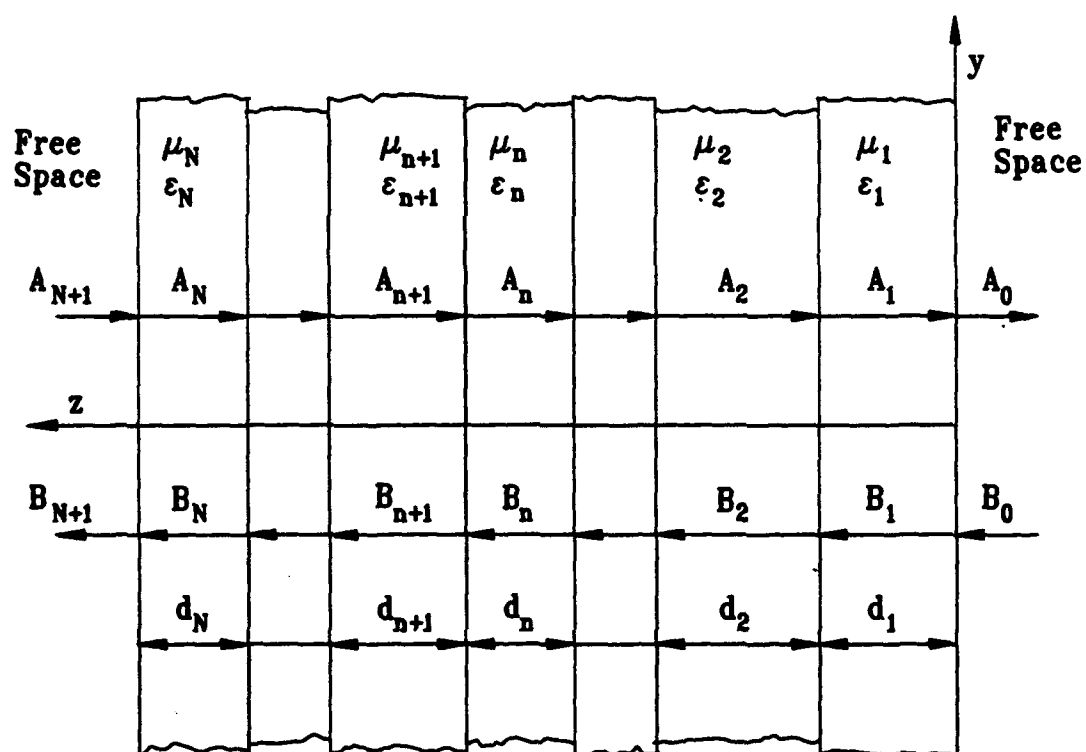


Figure 53: A plane multilayer, illustrating the outgoing and the reflected waves in each layer.

where T is the transmission coefficient of the multilayer. The field in each layer can be regarded as an infinite series of the plane waves bouncing back and forth, but it is more convenient (and equally valid) to consider it to be the sum of only two plane waves, one travelling outward and one reflected. In layer n , for example, the field is represented by:

$$E_n = (A_n e^{\gamma_n z} + B_n e^{-\gamma_n z}) e^{jk_0 y \sin \theta}. \quad (38)$$

Similarly, in layer $n+1$ the electric field intensity is given by:

$$E_{n+1} = (A_{n+1} e^{\gamma_{n+1} z} + B_{n+1} e^{-\gamma_{n+1} z}) e^{jk_0 y \sin \theta}. \quad (39)$$

The boundary between layers n and $n+1$ is located at:

$$z_n = d_1 + d_2 + d_3 + \dots + d_n. \quad (40)$$

By enforcing the boundary conditions on E_x and H_y at $z = z_n$, it can show that:

$$\begin{bmatrix} A_{n+1} \\ B_{n+1} \end{bmatrix} = \begin{bmatrix} P_n & Q_n \\ R_n & S_n \end{bmatrix} \begin{bmatrix} A_n \\ B_n \end{bmatrix}, \quad (41)$$

where:

$$P_n = \frac{1}{2} \left(1 + \frac{\mu_{n+1} \gamma_n}{\mu_n \gamma_{n+1}} \right) e^{(\gamma_n - \gamma_{n+1}) z_n}, \quad (42)$$

$$Q_n = \frac{1}{2} \left(1 - \frac{\mu_{n+1} \gamma_n}{\mu_n \gamma_{n+1}} \right) e^{-(\gamma_n + \gamma_{n+1}) z_n}, \quad (43)$$

$$R_n = \frac{1}{2} \left(1 - \frac{\mu_{n+1} \gamma_n}{\mu_n \gamma_{n+1}} \right) e^{(\gamma_n + \gamma_{n+1}) z_n}, \quad (44)$$

and:

$$S_n = \frac{1}{2} \left(1 + \frac{\mu_{n+1} \gamma_n}{\mu_n \gamma_{n+1}} \right) e^{-(\gamma_n - \gamma_{n+1}) z_n}. \quad (45)$$

The propagation constant γ_n for layer n will be complex if the medium is dissipative. Both the real and the imaginary parts of γ_n will be positive. If layer n is a lossless medium, γ_n will be purely imaginary. The wave equation is employed to obtain:

$$\gamma_n = j \sqrt{\omega^2 \mu_n \epsilon_n - k_0^2 \sin^2 \theta}. \quad (46)$$

The reflection and transmission coefficient of the multilayer can be calculated in a systematic manner by setting:

$$A_0 = 1 \quad (47)$$

and:

$$B_0 = 0 \quad (48)$$

and then by using the recursion equations Equation (41) to calculate $A_1, B_1, A_2, B_2, \dots, A_{N+1}$, and B_{N+1} in that order.

From Eqs. (35) through (38),

$$E_0 = A_{N+1}, \quad (49)$$

$$R = \frac{B_{N+1}}{A_{N+1}}, \quad (50)$$

and:

$$R = \frac{1}{A_{N+1}}. \quad (51)$$

In the TE case the constants A_n and B_n represent the electric field intensities of the outgoing and reflected wave in each layer. In the TM case (parallel polarisation) the solution proceeds in the same manner. The equations given above apply in both cases but the A_n and B_n represent the magnetic field intensities in the TM case and μ_{n+1} and μ_n must be replaced with ϵ_{n+1} and ϵ_n in Eqs. (42) through (45).

If a perfectly conducting sheet is placed on the right-hand surface of the multilayer (i.e., on the x-y plane), the solution is again given by the equations above with the exception that the transmission coefficient T is not calculated in this case, and Eqs. (47) and (48) are replaced with:

$$A_1 = 1 \text{ and } B_1 = -1 \text{ in the TE case} \quad (52)$$

and:

$$A_1 = 1 \text{ and } B_1 = 1 \text{ in the TM case.} \quad (53)$$

Equations (52) and (53) are obtained by forcing the tangential electric field intensity to vanish at the perfectly conducting plane.

In the above equations, the reflection coefficient R is defined as the ratio of the reflected wave amplitude to the incident wave amplitude at the coordinate origin; that is,

$$R = \frac{E_z^r(0,0,0)}{E_z^i(0,0,0)}; \text{ for the TE case,} \quad (54)$$

and:

$$R = \frac{H_z^r(0,0,0)}{H_z^i(0,0,0)}; \text{ for the TM case.} \quad (55)$$

Appendix B

Scattering of Plane Waves by Stratified (multilayered) Cylinders

Details of the scattering of plane waves by multilayered dielectric cylinders of infinite length with normal incidence are presented in [10]. Here, a summary of [10] is presented. Consider a plane wave to have normal incident on a multilayered dielectric cylinder consisting of M lossless homogeneous layers as shown in Figure 54. The cylinder axis is taken to be the z axis in the rectangular coordinate system, and the x axis is the axis of propagation of the incident plane wave. The permeability and permittivity of layer m are denoted by μ_m and ϵ_m , and the phase constant is given by:

$$k_m = \omega \sqrt{\mu_m \epsilon_m} \quad (56)$$

In the TM case, the electric field has only a z component given in layer m by:

$$E_m = \sum_{n=0}^{\infty} [A_{mn} J_n(k_m \rho) + B_{mn} N_n(k_m \rho)] \cos n\phi \quad (57)$$

where (ρ, ϕ, z) are the cylindrical coordinates and J_n and N_n represent the Bessel and Neumann functions. The time dependence, $e^{j\omega t}$, is implied. In the TE case the solution is obtained from the equations given here by interchanging μ and ϵ and \vec{E} and \vec{H} , where \vec{H} represents the magnetic field intensity.

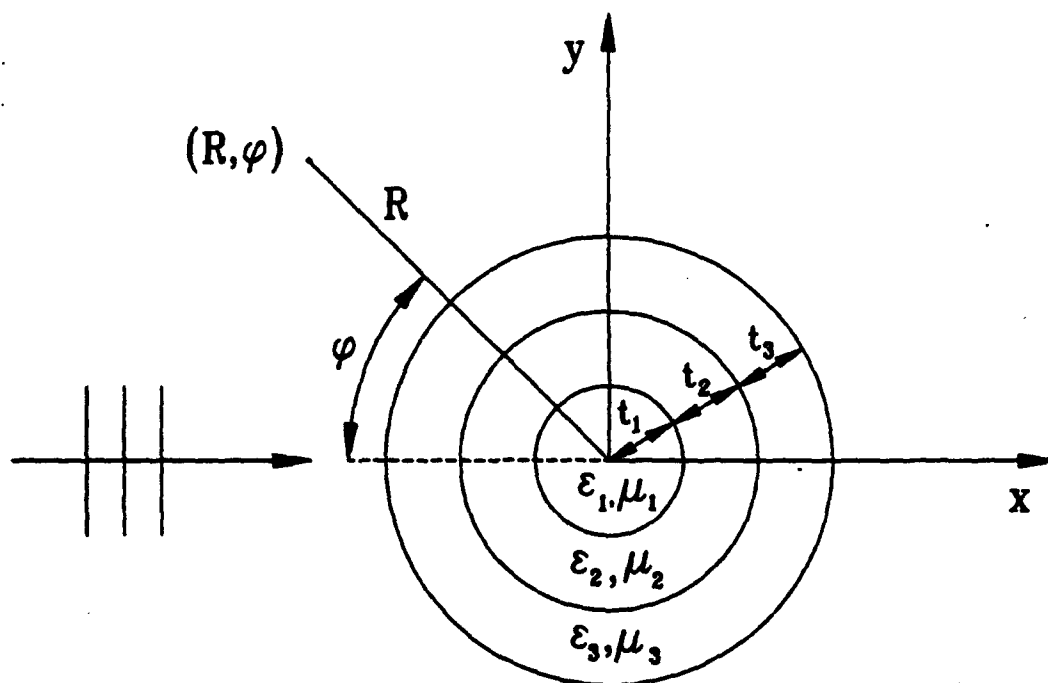


Figure 54: A Multilayered Dielectric Cylinder of Infinite Length.

The coefficients A_{mn} and B_{mn} must be determined by applying the boundary conditions of E_z and H_ϕ at each interface. From Maxwell equations, the ϕ component of the magnetic field intensity in layer m is given by:

$$H_m = \frac{k_m}{j\omega\mu_m} \sum_{n=0}^{\infty} [A_{mn}J'_n(k_m\rho) + B_{mn}N'_n(k_m\rho)] \cos n\phi \quad (58)$$

where J'_n and N'_n denote the derivatives of the Bessel and Neumann functions with respect to the arguments.

Let R_m denote the outer radius of layer m . From the boundary conditions at the interface between the layers m and $m+1$, it is found that the wave expansion coefficients for the two regions have the following linear relations:

$$A_{m+1,n} = U_{mn}A_{mn} + W_{mn}B_{mn} \quad (59)$$

and:

$$B_{m+1,n} = V_{mn}A_{mn} + X_{mn}B_{mn} \quad (60)$$

where:

$$U_{mn} = \frac{\pi R_m}{2\mu_m} [-\mu_{m+1}k_m J'_n(k_m R_m) N_n(k_{m+1} R_m) + \mu_m k_{m+1} J_n(k_m R_m) N'_n(k_{m+1} R_m)] \quad (61)$$

$$V_{mn} = \frac{\pi R_m}{2\mu_m} [\mu_{m+1}k_m J'_n(k_m R_m) J_n(k_{m+1} R_m) - \mu_m k_{m+1} J_n(k_m R_m) J'_n(k_{m+1} R_m)] \quad (62)$$

$$W_{mn} = \frac{\pi R_m}{2\mu_m} [-\mu_{m+1}k_m N'_n(k_m R_m) N_n(k_{m+1} R_m) + \mu_m k_{m+1} N_n(k_m R_m) N'_n(k_{m+1} R_m)] \quad (63)$$

and:

$$X_{mn} = \frac{\pi R_m}{2\mu_m} [\mu_{m+1}k_m N'_n(k_m R_m) J_n(k_{m+1} R_m) - \mu_m k_{m+1} N_n(k_m R_m) J'_n(k_{m+1} R_m)] \quad (64)$$

If the coefficients in the first layer (A_{1n} and B_{1n}) were known, the coefficients in the remaining layers could be calculated by using Equations(59) and (60), recursively. To permit a procedure of this type, define a set of normalized coefficients A'_{mn} and

B'_{mn} by the proportionality constant K_n as follows:

$$A_{mn} = K_n A'_{mn} \quad (65)$$

and:

$$B_{mn} = K_n B'_{mn}. \quad (66)$$

With no loss of generality, Let:

$$A'_{1n} = 1 \quad (67)$$

If the center layer is a dielectric medium, the field must be finite at the origin and:

$$B'_{1n} = 0. \quad (68)$$

The normalized coefficients also obey the same recursion formulas and we can now calculate A'_{2n} , B'_{2n} , \dots , A'_{Mn} , B'_{Mn} , $A'_{M+1,n}$, and $B'_{M+1,n}$ in that order.

The field in the exterior free-space region is given by:

$$E_{M+1} = \sum_{n=0}^{\infty} [(-j)^n e_n J_n(k_0 \rho) + C_n H_n^{(2)}(k_0 \rho) \cos n\phi] \quad (69)$$

where $H_n^{(2)}(k_0 \rho)$ represents the Hankel function and k_0 is the phase constant of free space. The first series in Equation(69) represents the incident plane-wave field, and the second series is the scattered field which contains outward-traveling waves only. The function e_n is unity if $n=0$, and $e_n=2$ if n is greater than zero.

The scattering coefficients for the exterior region are given by:

$$C_n = j B_{M+1,n} = \frac{-(-j)^n e_n B'_{M+1,n}}{B'_{M+1,n} + j A'_{m+1,n}} \quad (70)$$

This completes the solution. Equation(57) can be used to calculate the field at any point in the dielectric cylinder, and Equations(69) and (70) are used to calculate the field at any point outside the cylinder.

In the case of a perfectly conducting cylinder with one or more dielectric layers, let a be the radius of the conducting cylinder and R_1 the outer radius of the first

dielectric layer. The above equations again give the solution if Equation(66) is replaced with:

$$B'_{1n} = -\frac{J_n(k_1 a)}{N_n(k_1 a)} \quad (71)$$

for the TM case and:

$$B'_{1n} = -\frac{J'_n(k_1 a)}{N'_n(k_1 a)} \quad (72)$$

for the TE case. Equations(71) and (72) are obtained by setting $E_z=0$ or $E_\phi=0$ at the conducting surface.

When a plane wave is incident on a scattered cylindrical structure of infinite length, the distant scattering pattern is described by the echo width which is defined as:

$$\sigma_{2D} = \lim_{\rho \rightarrow \infty} 2\pi\rho \left| \frac{E^s}{E^i} \right|^2 \quad (73)$$

The incident electric field E^i is taken to have unit magnitude. The scattered electric field for large distances from the cylinder,

$$E^s = \sqrt{\frac{2j}{\pi k_0 \rho}} e^{-jk_0 \rho} \sum_{n=0}^{\infty} e_n D_n \cos n\phi \quad (74)$$

where:

$$D_n = \frac{-B'_{M+1,n}}{B'_{M+1,n} + jA'_{M+1,n}} \quad (75)$$

Substituting Equations(74) and (75) into Equation(73) the bistatic echo width of the multilayered dielectric cylinder is given by:

$$\sigma_{2D} = \frac{2\lambda}{\pi} \left| \sum_{n=0}^{\infty} e_n D_n \cos n\phi \right|^2 \quad (76)$$

Appendix C

Scattering from Multijointed Cylinders

This appendix summarizes the solution for the multijointed cylinder geometry solved by N. Akhter [25]. The geometry for the multijointed cylinders is shown in Figure 55. The Uniform Theory of Diffraction is used to calculate the far-zone scattered field from this geometry. The solution is based on the modification of a 2-D dihedral solution using UTD by N. Akhter [25]. The solution is modified for dielectric material using the dielectric wedge diffraction coefficient in Equation (6).

The interactions needed to calculate the backscattered field in the UTD solution are shown in Figure 56. The diffracted field for each interaction term is calculated similar to the interactions for the trunk-ground interaction geometry in Chapter 6. For the single diffraction D terms, the calculation is the same as in Chapter 6 except now there are 2 cylinders. The spread factors for the D terms shown in Equation (2) are calculated similarly to the D terms in Chapter 6 using Equation (5).

The diffracted field for the RD and DR terms is calculated similar to the RD and DR terms in Chapter 6. The difference is that the multijointed cylinder geometry consists of 2 cylinders versus 1 cylinder for the trunk-ground interaction geometry. This difference allows rays to reflect and diffract from both cylinders. Therefore, terms including reflections from cylinder #2 and diffractions from cylinder #1 need

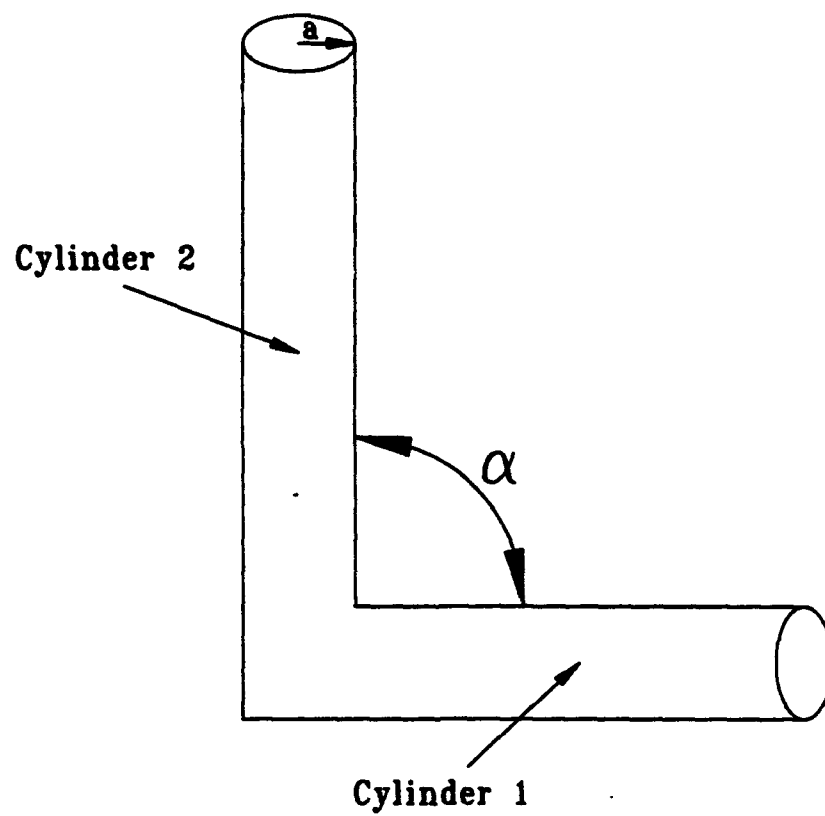
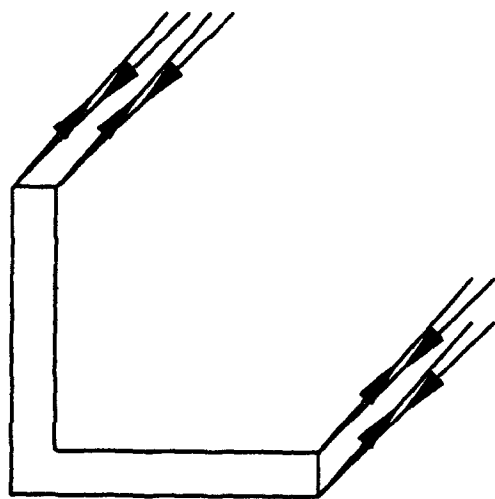
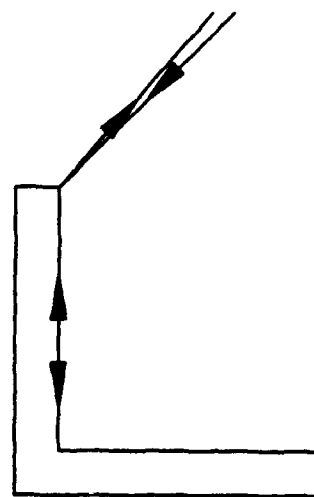


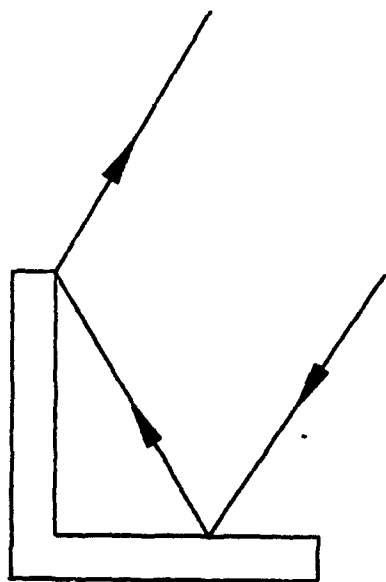
Figure 55: Geometry of multijointed cylinder.



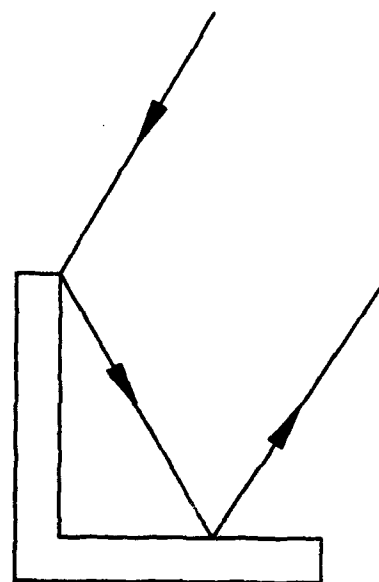
(1) D



(2) DRD



(3) RD



(4) DR

Figure 56: Diffraction interactions Used in calculating the scattering from multi-joined cylinders.

to be calculated in addition to the terms including reflections from cylinder #1 and diffractions from cylinder #2. The diffraction coefficients for the RD and DR fields are similar to the diffraction coefficients in Chapter 6. However, since both surfaces are now curved, the spreading factor will be different than the spreading factor used in Chapter 6.

The spread factors for the RD and DR terms shown in Equation (2) are calculated using Equation (5). For the RD and DR terms, the spread factors will be the same since the rays travel along the same ray path. The spread factor for the ray diffracted from cylinder #1 and reflected from the side of cylinder #2, the spreading factor is:

$$\rho^{D_1 R_2} = \left[\frac{\rho^d a}{a + (s + \rho^d) 2 \sin(\alpha - \theta)} \right]^{\frac{1}{2}} \quad (77)$$

where:

$$\rho^d = \frac{a}{\sin \theta + \sin(2\alpha - \theta)}. \quad (78)$$

In the above equations, a is the cylinder radius and α is the dihedral angle between the cylinders. The spread factor for the ray diffracted from cylinder #2 and reflected from the side of cylinder #1, the spreading factor is:

$$\rho^{D_2 R_1} = \left[\frac{\rho^d a}{a + (s + \rho^d) 2 \sin \theta} \right]^{\frac{1}{2}} \quad (79)$$

where:

$$\rho^d = \frac{a}{\sin(\alpha + \theta) + \sin(\alpha - \theta)}. \quad (80)$$

The final interaction of interest is the Diffracted-Reflected-Diffracted (DRD) term which is calculated similar to the previous interaction terms. The spread factor for the ray diffracted from cylinder #2, reflected from cylinder #1, and then diffracted from cylinder #2 again is given by:

$$\rho^{D_2 R_1 D_2} = \left[\frac{\rho_1^d}{s(\rho_1^d + s)} \frac{\rho_1^r \rho_2^r}{(\rho_1^r + s)(\rho_2^r + s)} \rho_2^d \right]^{\frac{1}{2}} \quad (81)$$

where:

$$\rho_1^d = \frac{a}{\cos \alpha + |\sin(\alpha - \theta)|} \quad (82)$$

$$\rho_1^r = s \quad (83)$$

$$\frac{1}{\rho_2^r} = \frac{1}{s + \rho_1^d} + \frac{2}{a} \quad (84)$$

$$\rho_2^d = \frac{1}{(\rho_2^r + s)} + \frac{\cos \alpha + |\sin(\alpha - \theta)|}{a} \quad (85)$$

$$(86)$$

The spread factor for the ray diffracted from cylinder #1, reflected from cylinder #2, and then diffracted from cylinder #1 again is given by:

$$\rho^{D_1 R_2 D_1} = \left[\frac{\rho_1^d}{s(\rho_1^d + s)} \frac{\rho_1^r \rho_2^r}{(\rho_1^r + s)(\rho_2^r + s)} \rho_2^d \right]^{\frac{1}{2}} \quad (87)$$

where:

$$\rho_1^d = \frac{a}{\cos \alpha + \sin \theta} \quad (88)$$

$$\rho_1^r = s \quad (89)$$

$$\frac{1}{\rho_2^r} = \frac{1}{s + \rho_1^d} + \frac{2}{a} \quad (90)$$

$$\rho_2^d = \frac{1}{(\rho_2^r + s)} + \frac{\cos \alpha + \sin \theta}{a} \quad (91)$$

$$(92)$$

REFERENCES

- [1] M. A. Karam, F. Amar, and A. K. Fung, "Electromagnetic wave scattering from a forest or vegetation canopy: Ongoing research at the University of Texas at Arlington," *IEEE Antennas Propagat. Magazine*, vol. 35, pp. 18-26, Apr. 1993.
- [2] D. E. Pitts, et. al., "Estimation of X-Band scattering properties of tree components," *IEEE Transactions on Geoscience and Remote Sensing*, vol. 26, pp. 612-616, Sept. 1988.
- [3] R. Kouyoumjian, "Asymptotic high-frequency methods," *Proc. IEEE*, vol. 53, pp. 864-876, 1965.
- [4] P. H. Pathak, W. D. Burnside, and R. J. Marhefka, "A uniform GTD analysis for the diffraction of electromagnetic waves by a smooth convex surface," *IEEE Trans. Antennas Propagat.*, vol. AP-28, pp. 631-642, Sept. 1980.
- [5] R. Kouyoumjian and P. Pathak, "A uniform geometrical theory of diffraction for an edge in a perfectly-conducting surface," *Proc. IEEE*, vol. 62, pp. 1448-1461, 1974.
- [6] J. Keller, "Diffraction by an aperture," *J. Appl. Phys.*, vol. 28, pp. 426-444, 1957.
- [7] W. D. Burnside and K. W. Burgener, "High frequency scattering by a thin lossless dielectric slab," *IEEE Trans. Antennas Propagat.*, vol. AP-31, pp. 104-110, Jan. 1983.
- [8] R. G. Rojas-Teran and W. D. Burnside, "GTD analysis of airborne antennas radiating in the presence of lossy dielectric layers," Semi-Annual Report 710964-8, The Ohio State University ElectroScience Laboratory, Department of Electrical Engineering, Aug. 1981.
- [9] Short course notes on, "The modern geometrical theory of diffraction," vols. 1,2, and 3, The Ohio State University ElectroScience Laboratory, Department of Electrical Engineering, 1982.

- [10] J. H. Richmond, "Efficient recursive solutions for plane and cylindrical multilayers," Technical Report 1968-1, The Ohio State University ElectroScience Laboratory, Department of Electrical Engineering, Aug. 1965.
- [11] K. Chiang and R. Marhefka, "Bistatic scattering from a finite circular cylinder," Technical Report 714614-4, The Ohio State University ElectroScience Laboratory, Department of Electrical Engineering, July 1984.
- [12] M. Kolawole, "A sparse canopy forest backscatter model," *International Geoscience and Radio Science Symposium*, pp. 5-9, 1991.
- [13] G.-Q. Sun and D. S. Simonett, "Simulation of L-band and HH microwave backscattering from a coniferous forest stands," *Inter. J. Remote Sensing*, pp. 907-925, 1988.
- [14] F. Altman, A. Schneider, and W. Tinga, "Permittivity of green wood," *International Geoscience and Radio Science Symposium*, pp. 2848-2851, 1989.
- [15] M. Dobson, R. DeLaSierra, and N. Christensen, "Spatial and temporal variations of the microwave dielectric properties of loblolly pine trunks," *International Geoscience and Radio Science Symposium*, pp. 1107-1110, 1991.
- [16] W. Salas, K. Ranson, B. Rock, and D. Moss, "Diurnal changes in the dielectric properties and water status of eastern hemlock and red spruce from Howland, ME," *International Geoscience and Radio Science Symposium*, pp. 1111-1114, 1991.
- [17] F. Amar, M. A. Karam, A. K. Fung, G. De Grandi, C. Lavallo, and A. Sieber, "Properties of radar backscatter of forests measured with a multifrequency polarimetric SAR," *International Geoscience and Radio Science Symposium*, pp. 533-535, 1992.
- [18] M. Karam and A. Fung, "A first order backscattering model for a forested canopy with a volume-fraction profile," *International Geoscience and Radio Science Symposium*, pp. 2836-2839, 1989.
- [19] K. McDonald, R. Zimmermann, and J. Way, "An investigation of the relationship between tree water potential and dielectric constant," *International Geoscience and Radio Science Symposium*, pp. 523-525, 1992.
- [20] T. Mo and J. Wang, "Modelling of SAR polarisation phase difference from trees," *International Geoscience and Radio Science Symposium*, pp. 55-58, 1988.
- [21] G.-Q. Sun, D. S. Simonett, and A. H. Strahler, "A radar backscattering model for discontinuous forest canopies," *International Geoscience and Radio Science Symposium*, pp. 2832-2835, 1989.

- [22] M. Poirier. personal communication.
- [23] P. Beckmann and A. Spizzichino, *The Scattering Of Electromagnetic Waves From Rough Surfaces*. Pergamon Press, New York, 1963.
- [24] R. J. Marhefka and J. Silvestro, "Near zone-basic scattering code user's manual with space station applications," Technical Report 716199-13, The Ohio State University ElectroScience Laboratory, Department of Electrical Engineering, Mar. 1989.
- [25] N. Akhter, *Far Zone Electromagnetic Scattering From Complex Shapes Using Geometrical Theory of Diffraction*. Ph.D. dissertation, The Ohio State University, Columbus, OH 43210, 1993.